Thesis

Theoretical Study on Electronic Structure and Magnetic Property of Transition-Metal Nitrides

Hisashi Shimizu

OSAKA UNIVERSITY
Graduate School of Engineering Science
Department of Material Physics
Toyonaka Osaka

March 1997

Abstract

Theoretical study is made to understand and/or predict structural and magnetic properties of two kinds of $3d$ transition-metal nitrides. One is ferrimagnetic mixed compound $Mn_4N_{1-x}C_x$ and another is $3d$ transition-metal mononitride.

By using the recursion method we have studied effects of substitution of C for N on the magnetic moments of two kinds of Mn atoms in ferrimagnetic Mn_4N, Mn(I) which has localized character and a large moment and Mn(Ⅱ) which has itinerant character and a small moment antiparallel to that of Mn(I). As a function of C concentration the calculated Mn(I) moment is found to be almost unchanged while the absolute value of Mn(Ⅱ) moment increases and in total the net ferromagnetic moment decreases. These results are in good agreement with the experimental observations. It is clarified that this different influence of C substitution on each Mn moment originates from the nature of hybridization between Mn $3d$ and N (or C) $2p$ orbital is different for Mn(I) and Mn(Ⅱ).

Systematic FLAPW (full-potential linearized augmented-plane-wave) band calculations have been carried out for the whole series of transition-metal mononitrides MN (M=$3d$ transition metal) and the following results have been obtained.

1. ScN, TiN, VN and CrN

   The theoretical results for the equilibrium lattice constant of NaCl-type structure are in good agreement with the observations. The calculated bulk moduli are larger than those of pure fcc transition metals. This trend is seen also for other transition-metal nitrides.

2. MnN, CoN, NiN and CuN

   The equilibrium lattice constants of the non-magnetic state have been evaluated for both the NaCl-type and the ZnS-type structures. Energetically the NaCl-type structure is more stable than the ZnS-type one. The lattice constant observed for thin film of ZnS-type CoN which is grown on Cu substrate agrees well with our theoretical value.

   No magnetic order is expected for both the structures of MnN, NiN and CuN and also for ZnS-type CoN. For NaCl-type CoN we have obtained a ferromagnetic solution self-consistently and the energy of the ferromagnetic state is lower than that of the non-magnetic state. It is suggested that if a pure bulk sample of CoN is synthesized it may have the NaCl-type structure and shows some kind of magnetic order.

3. FeN

For ZnS-type FeN, no magnetic order is expected and the equilibrium lattice constant obtained for the non-magnetic state agrees well with the experimental data.

All of the equilibrium lattice constants calculated for the non-magnetic, the ferromagnetic and the $\boldsymbol{q} = [111]$ antiferromagnetic states of NaCl-type FeN are about 4.00 Å, which is much smaller than the observed value, a=4.50 Å.

The results of Mössbauer measurements can be explained reasonably if we assume the sample used in the experiment contains two domains, $\boldsymbol{q} = [111]$ antiferromagnetic NaCl-type FeN and ferromagnetic fcc Fe with the lattice constant a=4.50 Å.

Acknowledgements

The author would like to express his gratitude to Professor N. Suzuki for his support and discussion throughtout this work. He also appreciates a lot of precious advice and help from Professor M. Shirai.

He is very grateful to Professor A. Yanase and Professor H. Harima for providing him with FORTRAN source codes of FLAPW program. He is also very grateful to Professor K. Terao for providing him with FORTRAN original source codes of recursion program.

He willingly thanks Mr. T. Hinomura and Professor K. Suzuki for giving him their experimental data. He also thanks Dr. M. Takahashi for useful discussion on the results of his calculation. He thanks all of the students of Suzuki Lab. for their generosity on his use of computer.

Finally the author thanks Supercomputer Center, Institute for Solid State Physics, University of Tokyo for the facilities and the use of Fujitsu VPP500.

Contents

List of Figures

Part I

Part II

List of Tables

Part I

Part II

Part I

Theoretical Investigation for Magnetic Property of Mixed Compound $\mathbf{Mn_4N_{1-x}C_x}$ by Recursion Method

Chapter 1

Introduction

1.1 Previous Study on $Mn_4N_{1-x}C_x$

Intermetallic manganese compounds, Mn_4N and Mn_4C, have cubic perovskite type crystal structure (space group O_h^1, see Fig. 1.1). In these compounds Mn atoms occupy the corner and face center sites (these are labeled as Mn(I) and Mn(Ⅱ), respectively) and N or C atoms occupy the body center site. A lot of experiments have been performed to get the magnetic properties of Mn_4N so far [1],[2],[3]. Mn_4N becomes a ferrimagnet below $T_N = 755$K [3]. In the ferrimagnetic state the magnetic moment of Mn(I) and Mn(Ⅱ) is different in magnitude and direction. The magnitude of the magnetic moment of Mn(I) is about four times as large as that of Mn(Ⅱ), and it is along [111]-direction. The magnetic moment of Mn(Ⅱ) is mainly along $[\bar{1}\bar{1}\bar{1}]$-direction(antiparallel to Mn(I)), but cants a little from $[\bar{1}\bar{1}\bar{1}]$-direction to have a small non-collinear component lying in a (111)-plane [3]. But this non-collinear component cancels if we sum up all these components in a unit cell. Mn_4C is unstable at room temperature [4] and is quite difficult to make a sample. Therefore little is known about the physical properties of Mn_4C. By partially replacing N atom by C atom, the Néel temperature increases but total magnetic moment decreases [2],[5].

The electronic band structures for the non-magnetic state of Mn_4N and Mn_4C and for the ferrimagnetic state of Mn_4N were calculated by Tagawa and Motizuki by the use of a self-consistent augmented plane wave (APW) method[6]. In the ferrimagnetic state of Mn_4N, the calculated magnetic moments inside the muffin-tin spheres at the Mn(I), Mn(Ⅱ) and N sites are 3.02, -0.96 and 0.09, respectively, in unit of μ_B/atom. These are compared with 3.85, -0.90 and $0.0\mu_B$/atom, respectively, observed at $T = 77$K[3]. The total moment is obtained to be $0.46\mu_B$/f.u. which is

about half of the observed value $1.14\mu_B$/f.u.[3]. They also estimated the magnetic moment of the mixed compound $Mn_4N_{1-x}C_x$, by adopting the rigid band model for a substitution of N atoms by C atoms, *i.e.* the Fermi level is shifted to lower energies with increasing x. The obtained results are not in agreement with the experiments.

1.2 Purpose of Part I

In Ref. [6] Tagawa *et.al.* failed to explain the change of the magnetic moment of each manganese atom in Mn_4N when N atoms are substituted by C atoms. We consider that the APW method is not adequate for mixed compounds such as $Mn_4N_{1-x}C_x$ because in the APW method it is necessary that the system has translational invariance. On the other hand, the recursion method does not require such a condition and this character makes it be possible to treat mixed compounds. Previously we applied the recursion method to the non-magnetic state of Mn_4N, Mn_4C and $Mn_4N_{1-x}C_x$ ($x = \frac{1}{8}, \frac{2}{8}, \frac{4}{8}, \frac{6}{8}, \frac{7}{8}$) to see an effect of substitution of N atoms by C atoms on the electronic structure of each Mn atom.

In this thesis we investigate the electronic structure of $Mn_4N_{1-x}C_x$ ($x = 0, 0.25, 1$) and an effect of N atoms substitution on the electronic and magnetic properties by the recursion method. In this calculation we assume that three Mn(Ⅱ) moments are all collinear.

Table 1.1: Magnetic moments of Mn_4N and $Mn_4N_{0.75}C_{0.25}$[2] observed at $T = 300$K. The unit is μ_B/f.u. for total and μ_B/atom for Mn(I) and Mn(Ⅱ).

	Mn_4N	$Mn_4N_{0.75}C_{0.25}$
Mn(I)	3.53	3.52
Mn(Ⅱ)	−0.89	−0.98
total	0.86	0.58

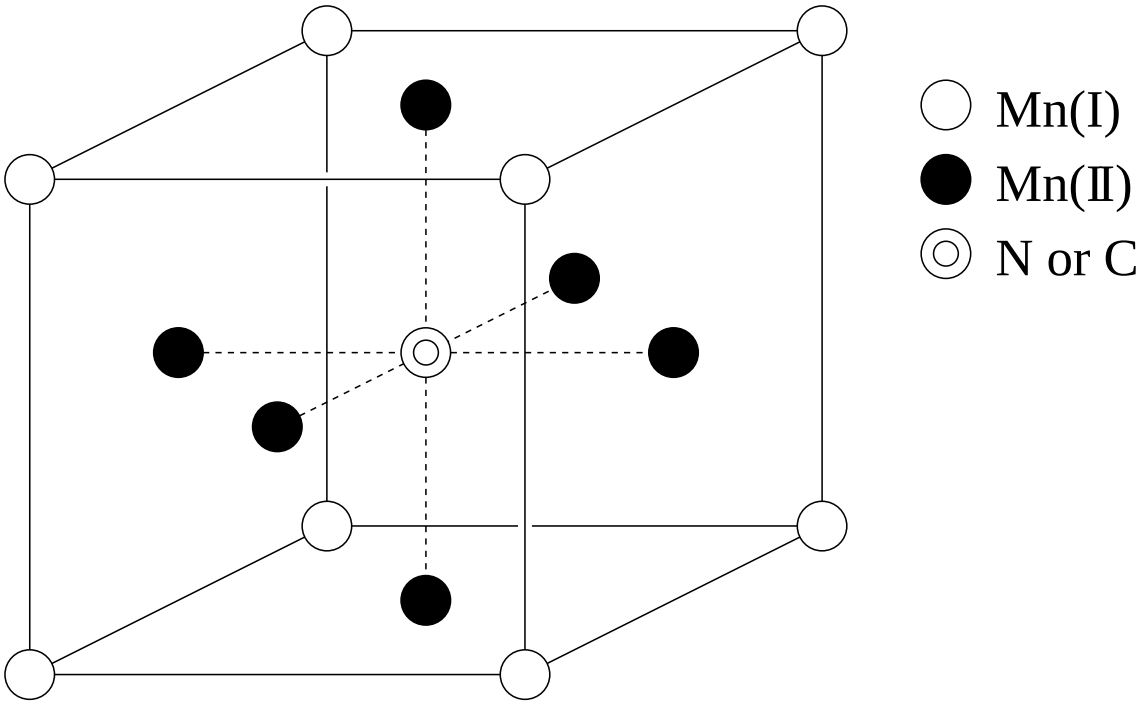

Figure 1.1: The crystal structure of Mn_4N and Mn_4C.

Chapter 2

Recursion Method

The recursion method is originally formulated by Heydock [7]. The concept of the recursion method is given by Refs. [7] and [8]. Therefore we would like to describe practical formulation of the recursion method.

2.1 Formulation

The starting Hamiltonian is assumed as

$$\begin{aligned}\mathcal{H} &= \sum_{ij}\sum_{mn}\sum_{\sigma} \mid i,m,\sigma\rangle t_{ij}^{mn}\langle j,n,\sigma \mid + \sum_{i,m}\sum_{\sigma} \mid i,m,\sigma\rangle E_{im}\langle i,m,\sigma \mid \\ &\quad - \sum_{i,m}\sum_{\sigma} \mid i,m,\sigma\rangle\sigma\Delta_i\langle i,m,\sigma \mid ,\end{aligned} \tag{2.1}$$

where $\mid i,m,\sigma\rangle$ denotes the atomic wave function of the m-th orbital with spin $\sigma(=\pm\frac{1}{2})$ at the i-th atom. The orthogonality relation

$$\langle i,m,\sigma \mid j,n,\sigma'\rangle = \delta_{ij}\delta_{mn}\delta_{\sigma\sigma'} \tag{2.2}$$

is assumed. The first term in the Hamiltonian represents the transfer terms between the nearest neighboring(n.n.) Mn(I) and Mn(II), Mn(II) and Mn(II) and Mn(II) and N or C as shown in Fig. 2.1, and t_{ij}^{mn} describes the transfer integral between the m-th orbital of the i-th atom and the n-th orbital of j-th atom. In the second term E_{im} denotes the site energy of the m-th orbital at the i-th atom. The last term of the Hamiltonian describes the exchange splitting for each atomic state in the ferrimagnetic state. The exchange splitting Δ_i is assumed to be independent in orbital. In the non-magnetic state this last term is vanishing.

In the recursion method we first construct from the basis function $\mid i,m,\sigma\rangle$ (atomic orbital) the new orthonormal basis functions which tri-diagonalize the Hamil-

tonian (2.1). The construction of the new basis functions are performed in a recursive way as follows. We first choose an initial atomic state $\mid i_0, m_0, \sigma\rangle \equiv |0\}$ and then a new basis function $|1\}$ which is orthogonal to $|0\}$ is determined from

$$\mathcal{H}|0\} = a_0|0\} + b_1|1\}. \tag{2.3}$$

Since the Hamiltonian (2.1) is diagonal with respect to spin states, we drop the spin suffix σ for simplicity from now on. If we choose a_0 as $a_0 = \{0| \mathcal{H} |0\}$, we obtain the orthogonality relation

$$\{0|1\} = 0. \tag{2.4}$$

The value of b_1 can determined from the normalization condition $\{1|1\} = 1$ and given by

$$|b_1|^2 = \{0|(\mathcal{H} - a_0)^\dagger(\mathcal{H} - a_0)|0\}. \tag{2.5}$$

Next, we operate the Hamiltonian to the new basis function $|1\}$ and express the result as follows:

$$\mathcal{H}|1\} = c_0|0\} + a_1|1\} + b_2|2\}. \tag{2.6}$$

From equation (2.6), the following two relations are obtained:

$$\{0| \mathcal{H} |1\} = c_0 + b_2\{0|2\}, \qquad \{1| \mathcal{H} |1\} = a_1 + b_2\{1|2\}. \tag{2.7}$$

Then if c_0 and a_1 are chosen as

$$\{0| \mathcal{H} |1\} = c_0, \qquad \{1| \mathcal{H} |1\} = a_1, \tag{2.8}$$

the following orthogonality is satisfied:

$$\{0|2\} = \{1|2\} = 0. \tag{2.9}$$

Furthermore, c_0 equals b_1 because

$$\{1| \mathcal{H} |0\} = a_0\{1|0\} + b_1\{1|1\} = b_1. \tag{2.10}$$

The value of b_2 is determined by the normalization condition $\{2|2\} = 1$. After repeating a similar procedure, we get the general relation as follows:

$$\begin{aligned}
\mathcal{H}|l\} &= b_l|l-1\} + a_l|l\} + |l+1\}, && (2.11)\\
a_l &= \{l| \mathcal{H} |l\} && (2.12)\\
|b_{l+1}|^2 &= \Big|(\mathcal{H} - a_l)\,|l\} - b_l|l-1\}\Big|^2, && (2.13)\\
\{l|l'\} &= \delta_{ll'} && (2.14)
\end{aligned}$$

with

$$|0\} \equiv |\ i_0, m_0, \sigma\rangle, \qquad |-1\} \equiv 0. \tag{2.15}$$

The local density of states(DOS) arising from the m_0 orbital with spin σ at the i_0 site is given by

$$\begin{aligned} D^{i_0}_{m_0,\sigma}(E) &= -\frac{1}{\pi}\mathrm{Im}\langle i_0, m_0, \sigma\,|\,\frac{1}{E-\mathcal{H}}|\ i_0, m_0, \sigma\rangle \\ &= -\frac{1}{\pi}\mathrm{Im}\{0|\frac{1}{E-\mathcal{H}}|0\}. \end{aligned} \tag{2.16}$$

Hence $D^{i_0}_{m_0,\sigma}(E)$ can be obtained by calculating the imaginary part of the $(0,0)$ component of the inverse matrix of $E-\mathcal{H}$. Since the matrix representation of the Hamiltonian with respect to the new basis function $|l\}$ becomes

$$\mathcal{H} = \begin{bmatrix} a_0 & b_1 & 0 & 0 & \cdots \\ b_1 & a_1 & b_2 & 0 & \\ 0 & b_2 & a_2 & b_3 & \ddots \\ 0 & 0 & b_3 & & \ddots \\ \vdots & & \ddots & \ddots & \end{bmatrix}, \tag{2.17}$$

$D^{i_0}_{m_0,\sigma}(E)$ can be expressed by

$$D^{i_0}_{m_0,\sigma}(E) = -\frac{1}{\pi}\mathrm{Im}\frac{D_1}{D_0}, \tag{2.18}$$

where D_0 and D_1 are defined by

$$D_0 = \begin{vmatrix} E-a_0 & -b_1 & 0 & \cdots \\ -b_1 & E-a_1 & -b_2 & \\ 0 & -b_2 & E-a_2 & \ddots \\ \vdots & & \ddots & \ddots \end{vmatrix}, \tag{2.19}$$

$$D_1 = \begin{vmatrix} E-a_1 & -b_2 & 0 & \cdots \\ -b_2 & E-a_2 & -b_3 & \\ 0 & -b_3 & E-a_3 & \ddots \\ \vdots & & \ddots & \ddots \end{vmatrix}, \tag{2.20}$$

Now we express D_0 as

$$D_0 = (E-a_0)D_1 - b_1^2 D_2, \tag{2.21}$$

where

$$D_2 = \begin{vmatrix} E-a_2 & -b_3 & 0 & \cdots \\ -b_3 & E-a_3 & -b_4 & \\ 0 & -b_4 & E-a_4 & \ddots \\ \vdots & & \ddots & \ddots \end{vmatrix}, \tag{2.22}$$

and then $D^{i_0}_{m_0,\sigma}(E)$ is written in the following form:

$$D^{i_0}_{m_0,\sigma}(E) = -\frac{1}{\pi}\mathrm{Im}\frac{1}{E-a_0-b_1^2\dfrac{D_2}{D_1}}. \tag{2.23}$$

Repeating the same procedure for $\frac{D_2}{D_1}, \cdots$, we can express $D^{i_0}_{m_0,\sigma}(E)$ by the following continued fraction:

$$D^{i_0}_{m_0,\sigma}(E) = -\frac{1}{\pi}\mathrm{Im}\cfrac{1}{E-a_0-\cfrac{b_1^2}{E-a_1-\cfrac{b_2^2}{E-a_2-\cfrac{b_3^2}{\ddots}}}}. \tag{2.24}$$

If the values of a_l and b_l converge to some constant values a and b, respectively, for $l \geq L$, then $D^{i_0}_{m_0,\sigma}(E)$ is further rewritten as

$$D^{i_0}_{m_0,\sigma}(E) = -\frac{1}{\pi}\mathrm{Im}\cfrac{1}{E-a_0-\cfrac{b_1^2}{E-a_1-\cfrac{b_2^2}{\ddots\cfrac{}{E-a_{L-1}-\cfrac{b_L^2}{\Omega(E)}}}}}, \tag{2.25}$$

where

$$\begin{aligned} \Omega(E) &= E-a-\cfrac{b^2}{E-a-\cfrac{b^2}{\ddots}} \\ &= E-a-\frac{b^2}{\Omega}. \end{aligned} \tag{2.26}$$

Solving equation (2.26) for Ω we obtain

$$\Omega(E) = \frac{1}{2}\left[E-a \pm \sqrt{(E-a)^2-b^2}\right]. \tag{2.27}$$

The density of states exists for the energy range in which $\Omega(E)$ is complex, *i.e.* for $|E-a| < |b|$.

2.2 Parameter Setting

In practical calculations by the recursion method for $Mn_4N_{1-x}C_x$, we take into account only the $3d$ orbitals for Mn atom and $2p$ orbitals for N or C atom. The transfer integral between two atoms can be represented by the Slater-Koster(SK) two center integrals $t(dd\sigma)$ *etc.* and the direction cosine of the vector connecting the two atoms. As mentioned before and as shown in Fig. 2.1 we consider the transfer integrals only for the n.n. atoms. Therefore we have three kinds of SK integrals, $t(dd\sigma)$, $t(dd\pi)$ and $t(dd\delta)$, for the n.n. Mn(I) and Mn(Ⅱ) and for the n.n. Mn(Ⅱ) and Mn(Ⅱ), and two kinds of SK integrals, $t(pd\sigma)$ and $t(pd\pi)$, for the n.n. Mn(Ⅱ) and N (or C). We have further considered different orbital energies for different atoms. For the purpose to evaluate the SK integrals and the orbital energies, we have performed the tight-binding band calculation for the non-magnetic state of Mn_4N and Mn_4C, and determined them so as to reproduce the band energies at the symmetry points in the Brillouin zone calculated by the APW method [6]. Their determined values are listed in Table 2.1. The SK integrals for the n.n. Mn(I)-Mn(Ⅱ) and the n.n. Mn(Ⅱ)-Mn(Ⅱ) are different in principle from symmetry although their interatomic distances are the same. For simplicity, however, we have assumed the same SK integrals for both the n.n. Mn(I) and Mn(Ⅱ) and the n.n. Mn(Ⅱ) and Mn(Ⅱ). It is seen from Table 2.1 that large differences between Mn_4N and Mn_4C lie in the values of the SK integral $t(pd\pi)$ and the orbital energy E_p.

Table 2.1: The Slater-Koster (SK) integrals and the site energies for Mn_4N and Mn_4C (in unit of Ryd).

SK integral		Mn_4N	Mn_4C
Mn(I)-Mn(Ⅱ) Mn(Ⅱ)-Mn(Ⅱ)	$t(dd\sigma)$	-0.03	-0.035
	$t(dd\pi)$	0.025	0.033
	$t(dd\delta)$	0.0	0.0
Mn(Ⅱ)-N Mn(Ⅱ)-C	$t(pd\sigma)$	0.12	0.118
	$t(pd\pi)$	0.1	0.08

site energy		Mn_4N	Mn_4C
Mn(I)	E_ε	0.61	0.61
	E_γ	0.5	0.5
Mn(Ⅱ)	$E_\varepsilon(xy)$	0.55	0.55
	$E_\varepsilon(yz, zx)$	0.58	0.58
	$E_\gamma(x^2 - y^2)$	0.52	0.52
	$E_\gamma(3z^2 - r^2)$	0.60	0.60
N	E_p	0.28	
C	E_p		0.42

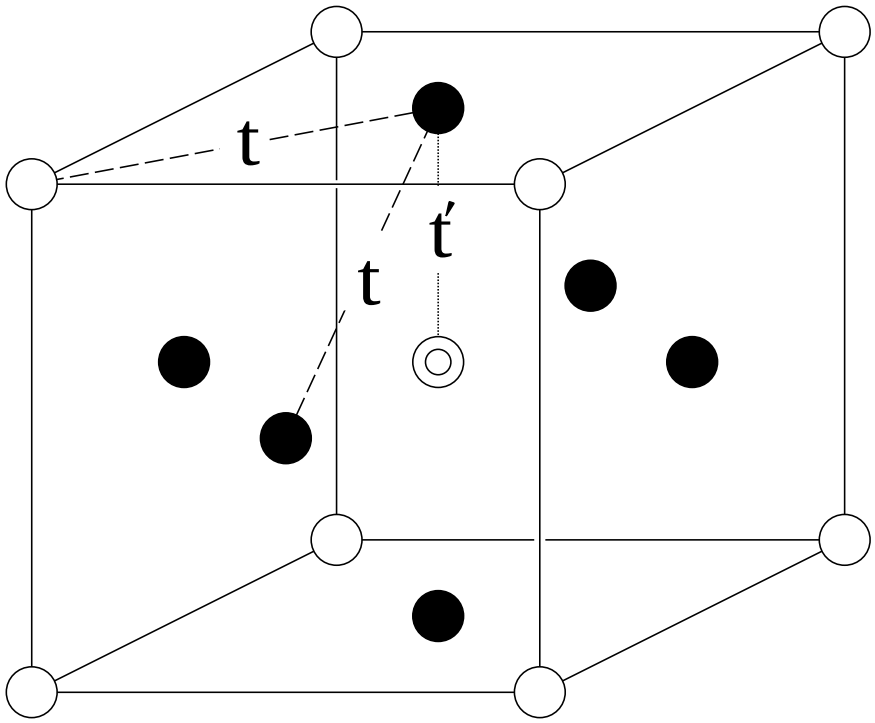

Figure 2.1: Transfer integrals between Mn(I)-Mn(Ⅱ), Mn(Ⅱ)-Mn(Ⅱ) and Mn(Ⅱ)-N are taken into account in the recursion calculation.

Chapter 3

Results

3.1 Mn_4N and Mn_4C

First, we applied the recursion method to the non-magnetic state of Mn_4N and Mn_4C. Figure 3.1 shows the recursion coefficients a_l and b_l for the non-magnetic state of Mn_4N when the initial state is chosen as $3d\gamma(x^2 - y^2)$ of Mn(Ⅱ). It is seen certainly that a_l and b_l show converging behavior for large l. In actual calculation we have adopted an approximate procedure, *i.e.* we have assumed $a_l = a$ and $b_{l+1} = b$ for $l \geq 13$. The values of a and b have been evaluated by taking the average over $l = 11$, 12 and 13. Then, the local DOS of Mn(Ⅱ) $3d\gamma(x^2 - y^2)$ orbital is calculated from equation (2.25). Carrying out the same calculational procedure for other atomic orbitals, we have calculated the partial DOS's of Mn(I) $3d$, Mn(Ⅱ) $3d$ and N $2p$ (or C $2p$) and the total DOS. The results are shown in Fig. 3.2 for Mn_4N and in Fig. 3.3 for Mn_4C. These DOSs do not reproduce quite precisely the DOSs calculated by the APW method [6], but we can regard that the overall profile of the DOS by APW has been reproduced.

The total DOS of Mn_4N is divided into three parts : (i) the low energy part between 0.0 and 0.3 Ryd, (ii) the intermediate energy range between 0.4 and 0.7 Ryd and (iii) the high energy part between 0.7 and 0.9 Ryd. The $3d$ orbitals of Mn(Ⅱ) are hybridized with the $2p$ orbitals of N in part (i) and (iii), and are mixed with the $3d$ orbitals of Mn(I) in part (ii). The $3d$ orbitals of Mn(I) mix little with $2p$ orbitals of N because we have neglected the direct transfer between Mn(I) and N. This feature is seen in the DOS calculated by APW method [6]. The Fermi level E_F is located in the part (ii). The DOS of Mn_4C is similar to Mn_4N except that the part (i) region of Mn_4C moves to the higher energy side compared with Mn_4N.

To calculate the DOS for the ferrimagnetic state of Mn_4N, the exchange splittings Δ_i are introduced for up and down spin states of the $3d$ orbitals at Mn(I) and Mn(Ⅱ) sites. We have assumed Δ_i is independent of the orbital m and determined its value so as to reproduce the observed Mn moments of pure Mn_4N. The total and partial DOS's calculated for the ferrimagnetic state of Mn_4N are shown in Fig. 3.4. The exchange splittings Δ_i, the values of the DOS's at E_F and the magnetic moments m_i at each atom are listed in Table 3.1. As seen from the table very small magnetic moment is induced on the N site through the hybridization between the Mn $3d$ and the N $2p$ orbitals. From the values of the exchange splitting Δ_i and the magnetic moment m_i we have evaluated the exchange energy $I_i = \Delta_i / |m_i|$. The results are 0.063 Ryd for Mn(I) and 0.048 Ryd for Mn(Ⅱ). These values are comparable with that of fcc Mn, 0.059 Ryd [9]. Using the total DOS at E_F, the coefficient of the electronic specific heat γ of Mn_4N is estimated to be $24 \mathrm{mJK^{-2}mol^{-1}}$. On the other hand, the observed value of γ is $42 \pm 2 \mathrm{mJK^{-2}mol^{-1}}$ [1]. Then, the mass enhancement factor due to electron correlation and/or electron-phonon interaction is evaluated to be $\lambda = 0.75$.

3.2 $Mn_4N_{1-x}C_x$

For the mixed compounds of $Mn_4N_{1-x}C_x$, detail study has been performed on $Mn_4N_{0.75}C_{0.25}$ compound [2]. So that we calculate the DOS for the non-magnetic and the ferrimagnetic state of $Mn_4N_{0.75}C_{0.25}$. In principle the recursion method itself can treat random system, but in such calculation we must determine a number of transfer integral and site energy parameters. Therefore we have approximated the crystal by a periodic array of cluster each of which consists of eight unit cells($2\times2\times2$) of Mn_4N lattice and hence contains 32 Mn atoms, 6 N atoms and 2 C atoms. As shown in Fig. 3.5 there are three types of clusters (a), (b) and (c) depending on different C configurations. The ratio of statistical probabilities of (a), (b) and (c) cases is 3 : 3 : 1.

It is further noted that for each type of cluster there exist several inequivalent sites for Mn(I), Mn(Ⅱ) and N atoms. In calculating the DOS we have taken average over all of the inequivalent atomic sites as well as over all of the configurations. As for the parameters such the SK integrals $t(pd\sigma)$ *etc*, the orbital energies of the $3d$ or $2p$ states and the exchange splitting Δ_i, we have used the values listed in Table 2.1 and Table 3.1. Since C concentration is small, we have used tentatively the same

values of $t(dd\sigma)$, $t(dd\pi)$ and $t(dd\delta)$ as those determined for Mn_4N. The effect of the substitution of N atoms by C atoms is taken only by a difference of the orbital energy of $2p$.

The averaged DOS's calculated by the recursion method for the non-magnetic and ferrimagnetic states of $Mn_4N_{0.75}C_{0.25}$ are shown in Figs. 3.6 and 3.7, respectively. The averaged magnetic moment at each atomic site is given in Table 3.2 together with the DOS's at E_F. In Fig. 3.8 we show the magnetic moments calculated for ferrimagnetic $Mn_4N_{1-x}C_x$ ($x = 0$, 0.25 and 1). Calculations for $x = 1$, *i.e.* for pure Mn_4C have been performed by using the same exchange splittings as those of Mn_4N. In the mixed compound $Mn_4N_{0.75}C_{0.25}$, the calculated magnetic moment of Mn(I) is found to be almost unchanged compared with that of Mn_4N while the absolute value of Mn(II) moment increases and in total the net ferromagnetic moment decreases. These results are in good agreement with the experimental results.

Table 3.1: Magnetic moment (m: [μ_B/atom]), DOS at Fermi energy (N(E_F: [states/Ryd atom] or [states/Ryd f.u.]), exchange energy (I: [Ryd]) and exchange splitting (Δ: [Ryd]), obtained for Mn_4N.

	m	$N(E_F)$			I	Δ
		up	down	total		
Mn(I)	3.9	11.4	2.8	14.2	0.063	0.248
Mn(II)	−0.88	26.7	13.6	120.9	0.048	0.042
N	0.07	0.6	0.5	1.1		
total	1.33	92.1	44.1	136.2		

Table 3.2: Magnetic moment(m: [μ_B]) and DOS at Fermi energy (N(E_F): [states/Ryd atom] or [states/Ryd f.u.]) obtained for $Mn_4N_{0.75}C_{0.25}$.

	m	$N(E_F)$		
		up	down	total
Mn(I)	3.9	11.7	4.3	16.0
Mn(II)	−0.95	25.5	15.8	124.0
total	1.1	88.2	51.8	140.7

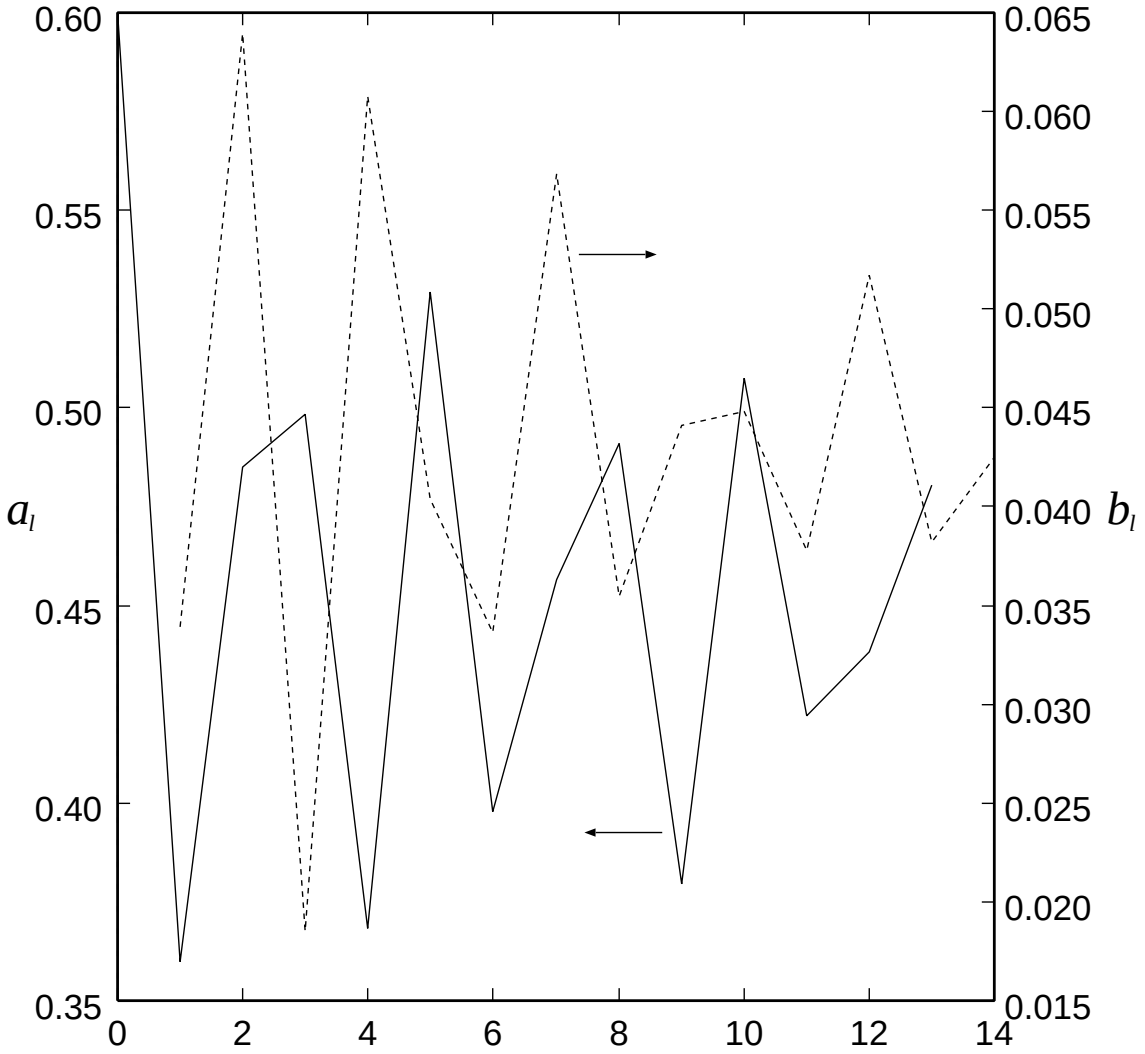

Figure 3.1: Recursion coefficient a_l and b_l for $d\gamma(x^2 - y^2)$ orbital of Mn(II)

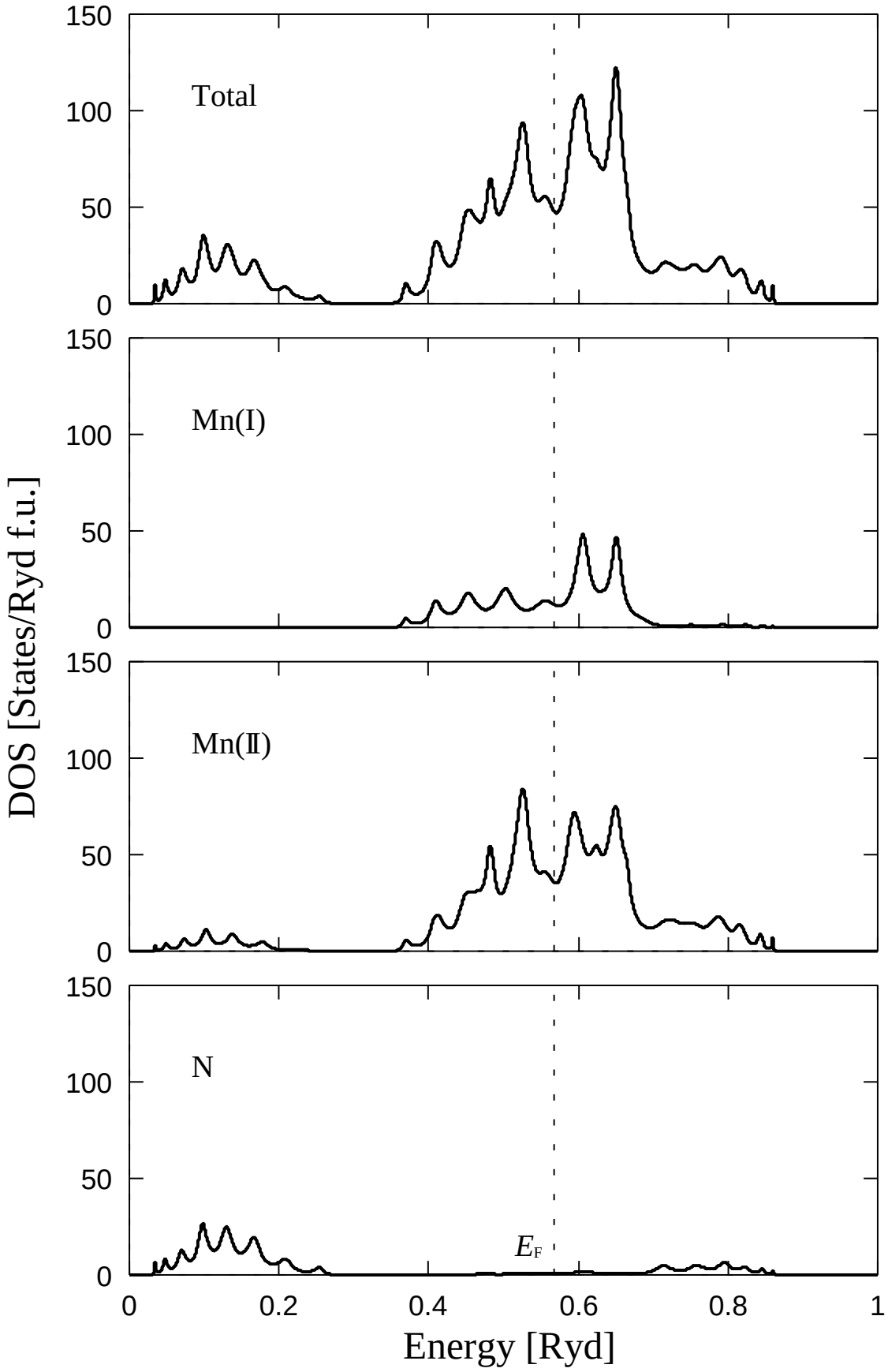

Figure 3.2: DOS for Mn_4N in non-magnetic state

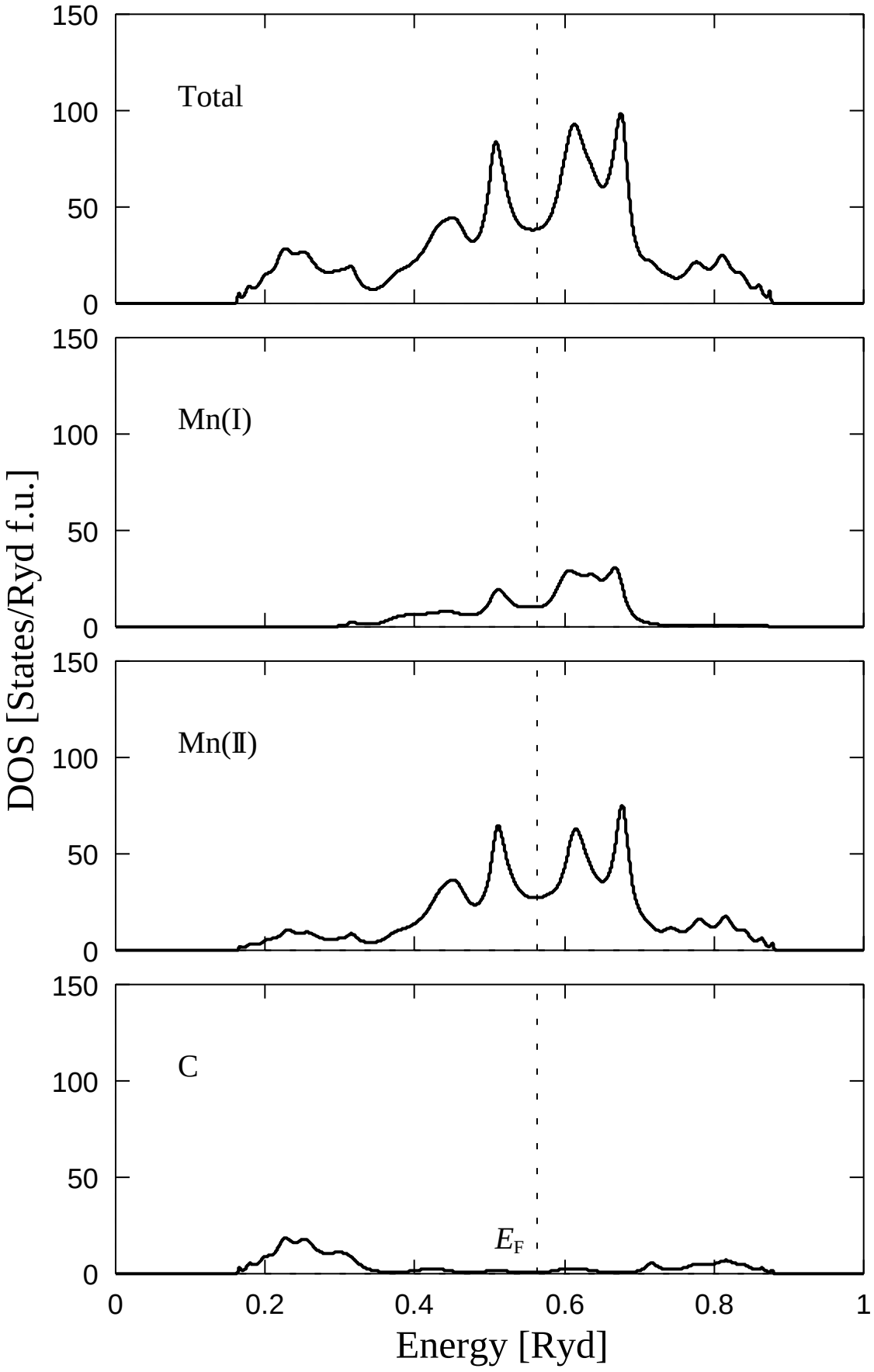

Figure 3.3: DOS for Mn_4C in non-magnetic state

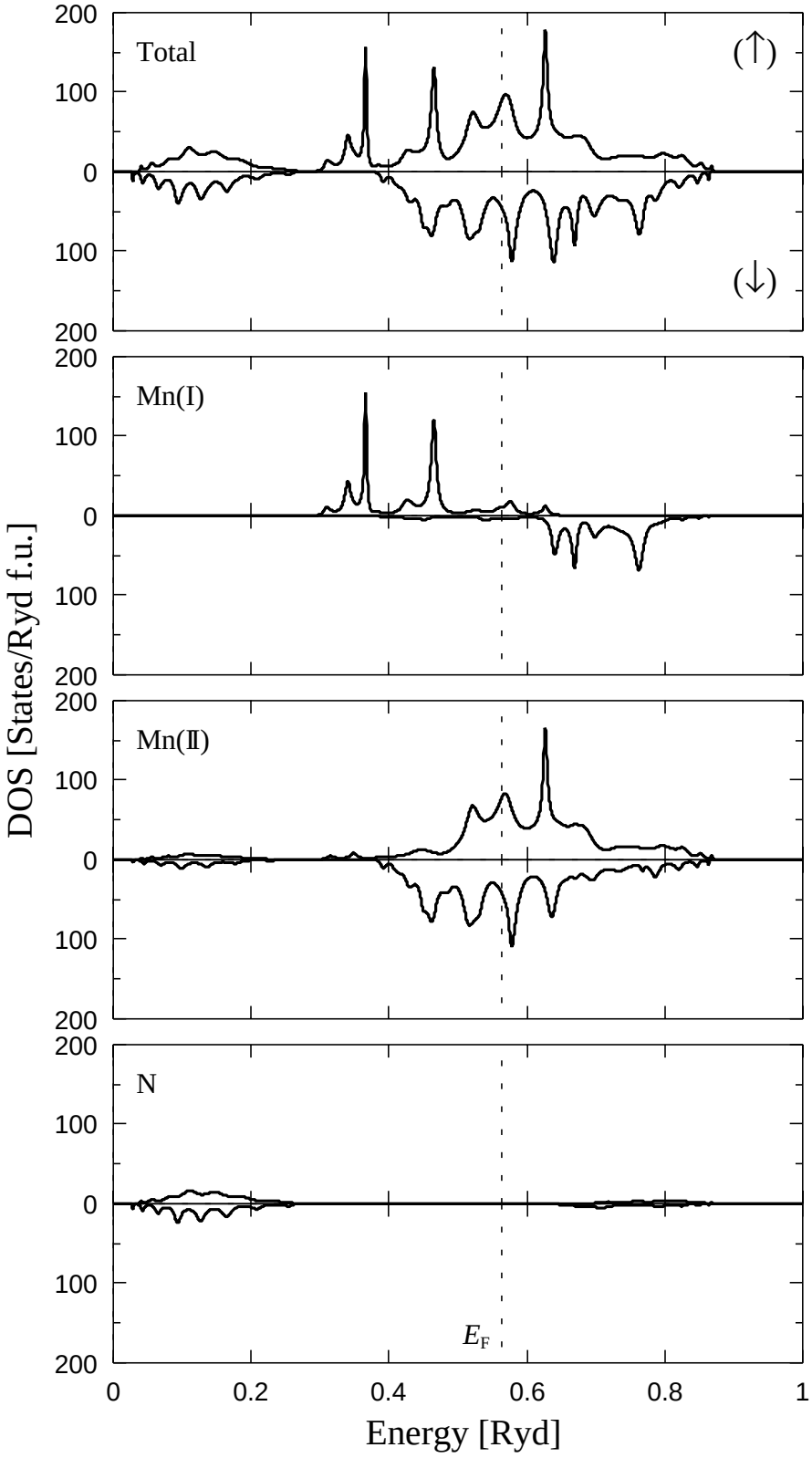

Figure 3.4: DOS for Mn_4N in ferrimagnetic state

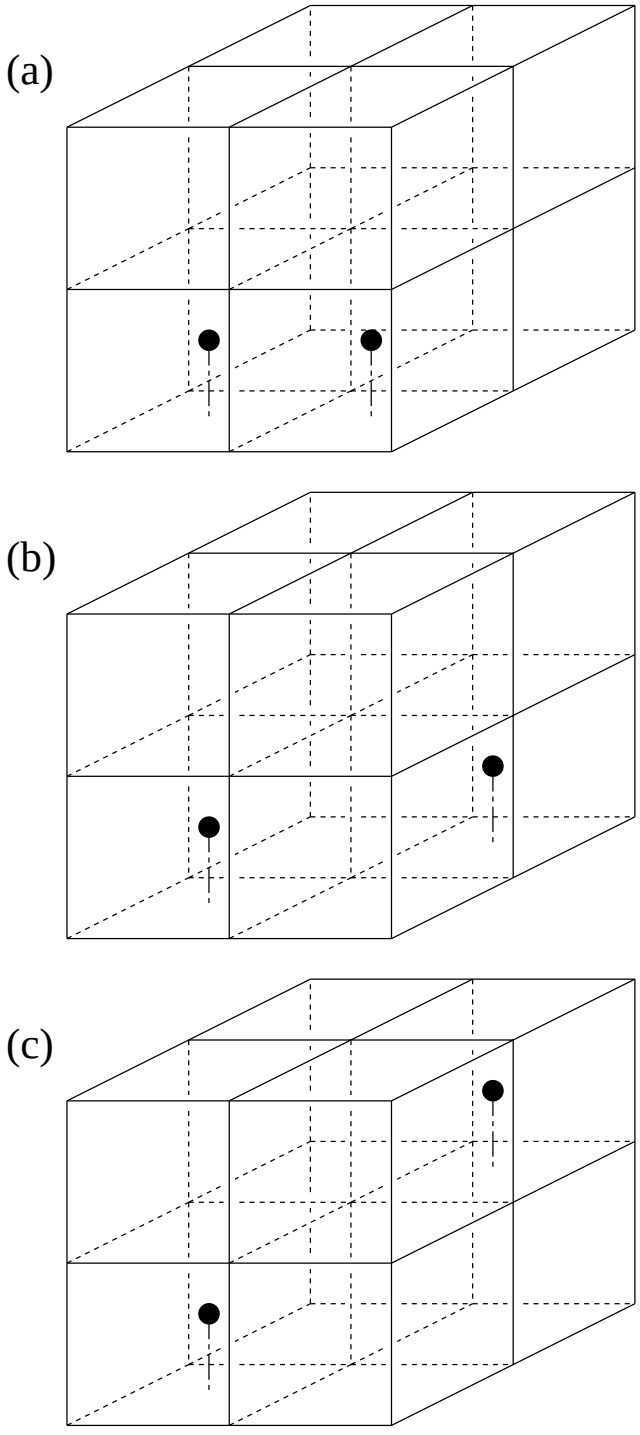

Figure 3.5: The three types of super cell depending on the configuration of two C atoms. Each cell contains 32 Mn atoms, 6 N atoms and 2 C atoms. In the figure only the C positions are depicted.

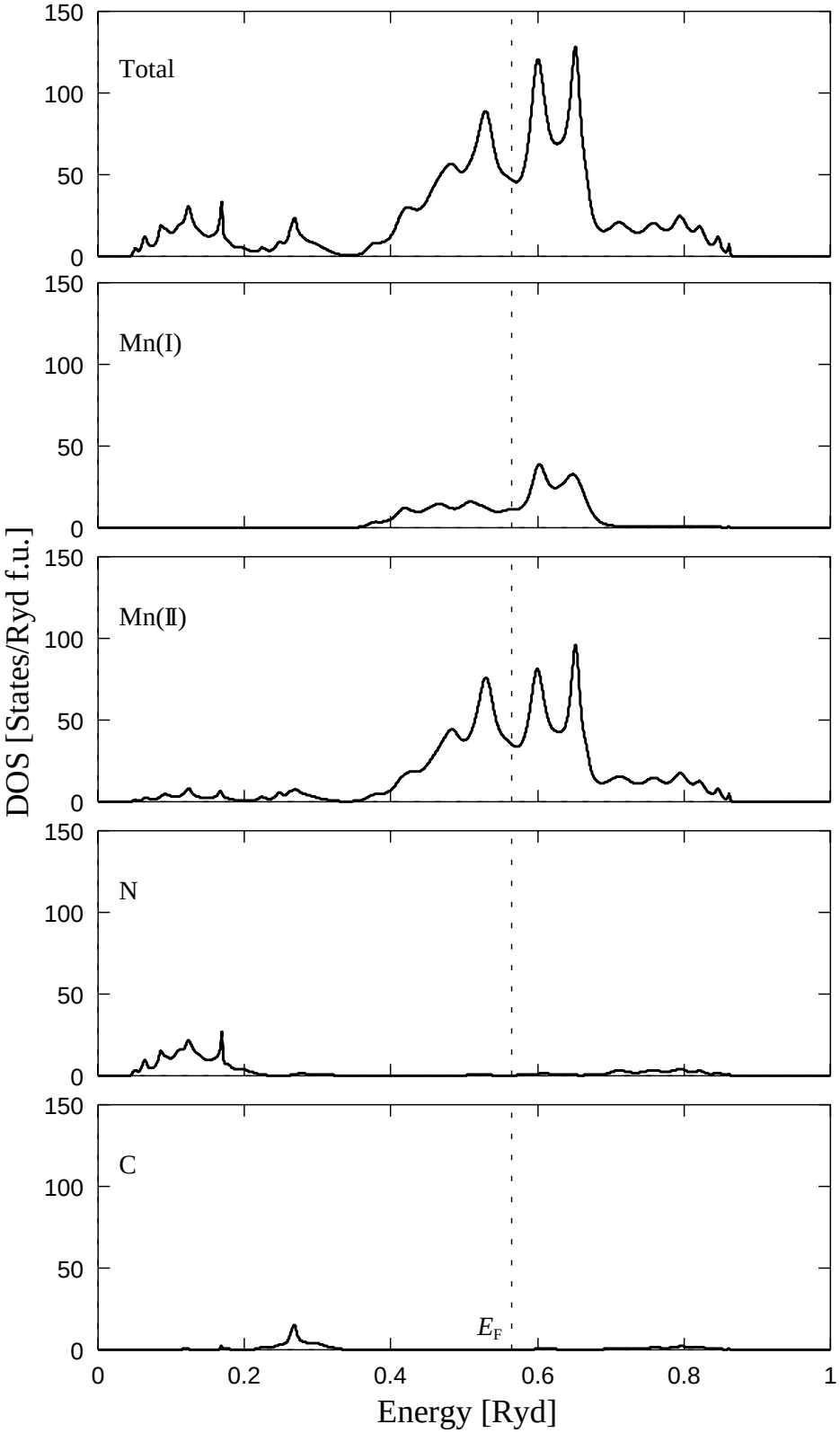

Figure 3.6: DOS for $Mn_4N_{0.75}C_{0.25}$ in non-magnetic state

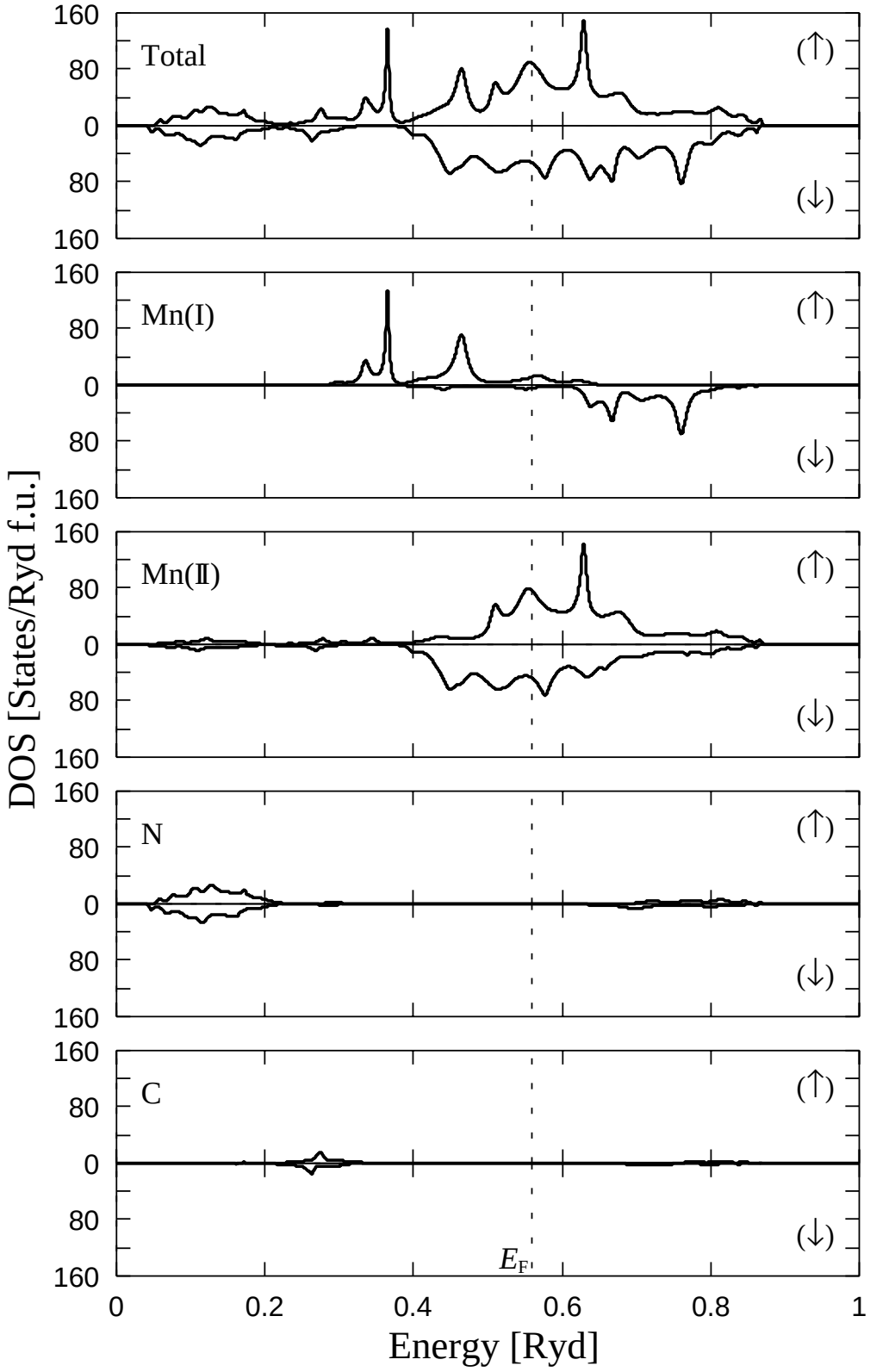

Figure 3.7: DOS for $Mn_4N_{0.75}C_{0.25}$ in ferrimagnetic state

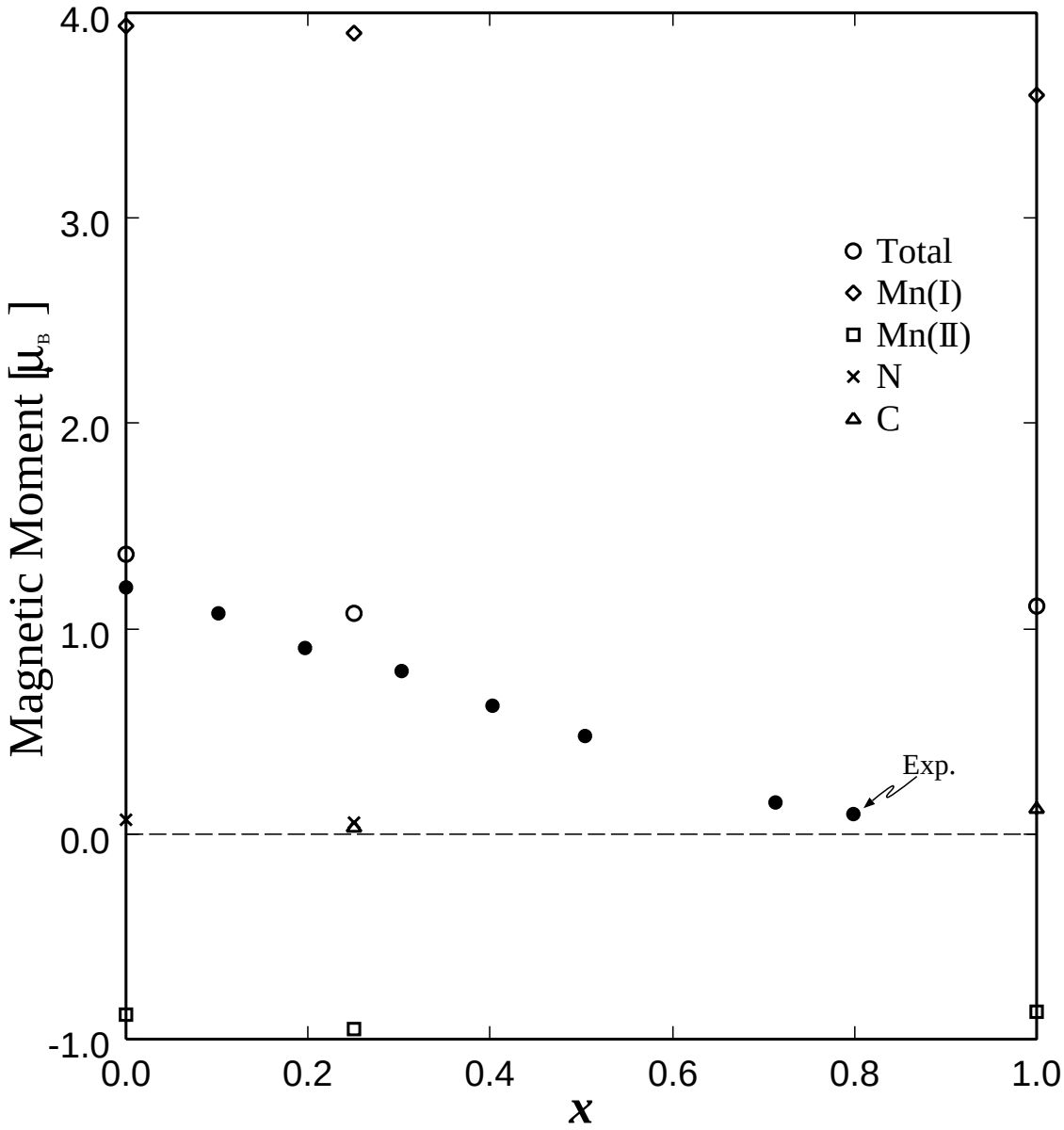

Figure 3.8: Magnetic moment of $Mn_4N_{1-x}C_x$ as a function of x. The unit is μ_B/f.u. (total) or μ_B/atom (Mn(I), Mn(Ⅱ), N and C). Meaning of each symbol is as follows: ○: total, ◇: Mn(I), □: Mn(Ⅱ) ,×: N and △: C. ● denotes the observed total moment referred from [5].

Chapter 4

Discussion

The different behaviors of Mn(I) and Mn(Ⅱ) moments for substitution of C atoms for N atoms can be understood physically as follows. First we note that Mn(I) and Mn(Ⅱ) atoms show different nature of hybridization with N atoms. The $3d$ states of Mn(I) hybridize little with the N $2p$ states, and Mn(I) has a large moment. Reflecting this localized character, the Mn(I) moment is less affected by substitution of C for N. On the other hand, the $3d$ states of Mn(Ⅱ) hybridize strongly with the N $2p$ states, and as the result Mn(Ⅱ) has a small moment reflecting the large band width of Mn(Ⅱ) $3d$ states. When N atoms are substituted with C atoms, the band width of the Mn(Ⅱ) $3d$ states is reduced due to the small SK integrals between Mn(Ⅱ) and C compared with those between Mn(Ⅱ) and N. As a result, the Mn(Ⅱ) moment increases with increasing the number of substituted C atoms.

Experimentally the total magnetic moment decreases with increasing the C concentration x and seems to go down to 0 before x reaches 1. Our results of $x = 0$ and $x = 0.25$ are in good agreement with the experimental results. However, if the concentration is increased further, the theoretical value is expected to deviate significantly from the experimental value, judging from the value of magnetic moment calculated at $x = 1$, *i.e.* for Mn_4C ($\sim 1.0\ \mu_B$/f.u.). This discrepancy may be ascribed to that the SK parameters between Mn and N atoms, the site energies and the exchange splitting of Mn atoms determined for Mn_4N have been used also for $Mn_4N_{1-x}C_x$ irrespective of the x value.

Bibliography

[1] J. García, J. Bartolomé, D. Gonzáles, R. Navarro and D. Fruchart, *J. Chem. Thermodyn.*, **15** (1983) 465.

[2] W. J. Takei, R. R. Heikes and G. Shirane, *Phy. Rev.*, **125** (1962) 1893.

[3] D. Fruchart, D. Givord, P. Convert, P. l'Héritier and J. P. Sénateur, *J. Phys. F:Metal Phys.*, **9** (1979) 2431.

[4] E. R. Morgan, *J. Metal*, **6** (1954) 983.

[5] R. Jusa and H. Puff, *Z. Elektrochem.*, **61** (1957) 810.

[6] Y. Tagawa and K. Motizuki, *J. Phys. Condens. Matter*, **3** (1990) 1753.

[7] R. Heydock, *Solid State Phys.*, **35** (1980) 215.

[8] D. G. Pettifor and D. L. Weaire, *The Recursion Method and Its Application* (Springer-Verleg, Berlin, Heidelberg, New York, Tokyo,1985).

[9] V. L. Moruzzi, J. R. Janak and A. R. Williams, *Calculated Electronic Properties of Metals* (Pergamon Press Inc., New York, 1978).

Part II

Systematic First Principles Study on Electronic, Structural and Magnetic Properties of Transition-Metal Mononitrides

Chapter 1

Introduction

1.1 What Is Transition-Metal Mononitrides

In contrast to the $3d$ transition-metal monoxides (MOs) which have been studied by a lot of people, $3d$ transition-metal mononitrides (MNs) have been studied only by a few workers [1],[2]. Most of MNs have the NaCl-type crystal structure (space group O_{h}^{5}) as most of MOs do. There are also some MNs which have the ZnS-type crystal structure (space group T_{d}^{2}) (see Table 1.1 and Figure 1.1).

In the past only ScN, TiN, VN and CrN have been synthesized and all of them have the NaCl-type structure. These compounds have received much interest by their own peculiar properties as well as their common properties of having a high melting point and being a hard material. ScN has been reported to be a semiconductor with a band gap of 2.1 eV [3]. TiN and VN have been extensively investigated both experimentally and theoretically because they become superconductors [4]. It is noted that it is hard to synthesize these two compounds in stoichiometric form and they include a lot of defects of N atoms. CrN becomes an antiferromagnet with Néel temperature $T_{\mathrm{N}} = 273$ K [5],[6]. This magnetic phase transition accompanies a structural phase transition from orthorhombic structure (low temperature phase) to NaCl-type structure (high temperature phase).

Fe and N atoms make many kinds of compounds, but if the proportionality of Fe and N atoms is restricted to 1:1, there were only a few report about amorphous phase FeN [7],[8]. Recently, however, FeN has been synthesized by the sputtering method [9],[10]. It is reported that FeN has two kinds of structures depending on the condition of sample making. One is the NaCl-type structure and another is the ZnS-type structure, and both of them contain some deficiencies of N atoms. From

^{57}Fe Mössbauer spectroscopy measurements performed by Nakagawa *et.al.* [9], it has been clarified that for NaCl-type FeN there are two kinds of Fe sites which have very large hyperfine fields of 49T and 30T. For ZnS-type FeN, on the other hand, no hyperfine field has been observed at the Fe site. Suzuki *et.al.* [10] also synthesized ZnS-type FeN and the lattice constant ($a_0 \sim 4.3$Å) observed by them is in good agreement with that of Nakagawa *et.al.*. Quite recently CoN with the ZnS-type structure has been synthesized by Suzuki *et.al.* [11], but nothing is still reported about MnN, NiN and CuN.

1.2 Purpose of This Work

In this part Ⅱ we carry out systematic first-principles band calculations for the whole series of $3d$ transition-metal mononitrides MN, first to understand the observed structural and magnetic properties of ScN, TiN, VN and CrN, and secondly to explain or predict the electronic, structural and magnetic properties of MnN, FeN, CoN, NiN and CuN whose physical properties are little known or which have not been synthesized. Particular attention is paid to understand the origin of the two kinds of large hyperfine fields observed on Fe sites in NaCl-type FeN.

In chapter 2 we first describe our actual band calculational procedures of FLAPW (full-potential linearized augmented-plane-wave) method, which is used throughout this part Ⅱ. Then, general aspects of the non-magnetic band structures of both NaCl-type and ZnS-type MNs are outlined.

In chapter 3 detailed calculational results for each MN except for FeN are presented. First the equilibrium lattice constants of non-magnetic ScN, TiN, VN and CrN with the NaCl-type structure are determined from total energy calculations and the results are compared with the observations. The bulk moduli of these four compounds are calculated also. Further the magnetic properties are investigated by calculating the generalized electronic susceptibility and by performing band calculations for the ferromagnetic state. Secondly the equilibrium lattice constants are evaluated for both the NaCl-type and the ZnS-type structures of non-magnetic MnN, CoN, NiN and CuN, and then the stable state is determined by comparing the total energies. A possibility of magnetic order for each compound is investigated by analyzing the density-of-states (DOS) at the Fermi level and the generalized electronic susceptibility and by carrying out ferromagnetic band calculations.

In chapter 4 detailed calculations are performed for both NaCl-type and ZnS-type

FeN. Particularly, in order to decide what kind of magnetic ordered state is the most stable for NaCl-type FeN, calculations of the band structure and the total energy are carried out for non-magnetic, ferromagnetic and two kinds of antiferromagnetic states of NaCl-type FeN. Band calculations for pure fcc Fe are also carried out to get insight into the effect of N atom deficiencies contained in real FeN samples. Hyperfine fields on Fe sites are calculated for each magnetic state of NaCl-type FeN as well as for pure fcc Fe, and then the origin of the two kinds of large hyperfine fields observed by Nakagawa *et.al.* [9] is proposed.

Finally the summary of Part Ⅱ is given in chapter 5.

Table 1.1: Crystal structure and physical properties of $3d$ transition-metal mononitrides synthesized thus far.

	Crystal structure	Lattice constant[Å]	Physical property
ScN	NaCl	4.50	semiconductor
TiN	NaCl	4.243	paramagnet
VN	NaCl	4.133	superconductor ($T_{\rm C}$ ∼6K for TiN,∼7K for VN)
CrN	NaCl	4.15	antiferromagnet Orthorhombic $\xrightarrow{273\text{K}}$ paramagnet NaCl
FeN	NaCl	4.5	antiferromagnet, large hyperfine field
	ZnS	4.3	paramagnet
CoN	ZnS	4.297	paramagnet

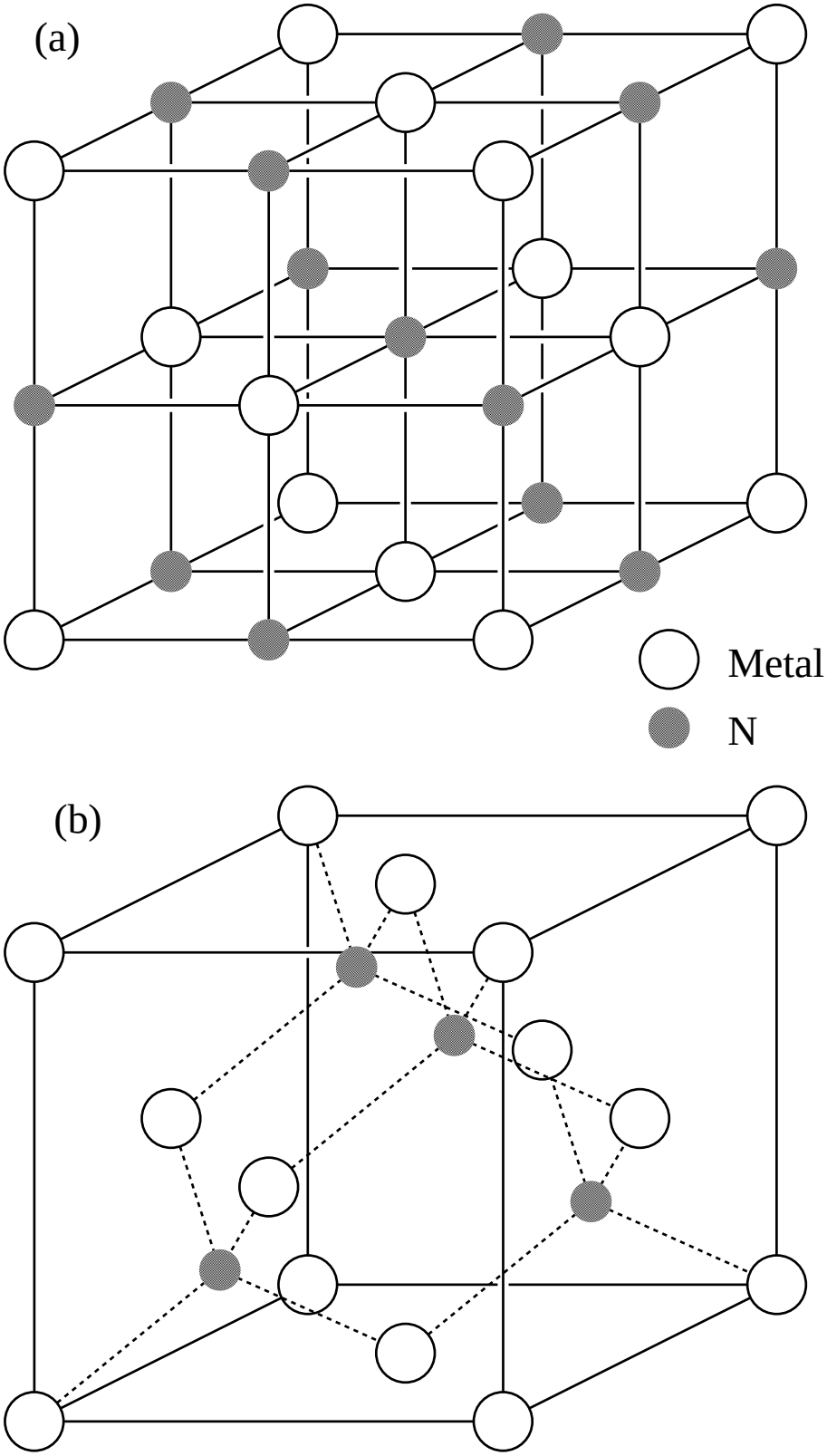

Figure 1.1: Crystal structure of $3d$ transition-metal mononitrides MN: (a) NaCl-type and (b) ZnS-type.

Chapter 2

FLAPW Band Calculations

Throughout this Part Ⅱ we use the band calculational method called FLAPW (full-potential linearized augmented-plane-wave), which is one of the most reliable methods in the framework of the local-density functional approximation (LDA). Detailed formalism of this method is provided in Refs. [12],[13],[14], and here we simply explain our actual calculational procedure in section 2.1. Then, in section 2.2 we outline general aspects of the non-magnetic band structures of both NaCl-type and ZnS-type MNs. Detailed calculational results for each compound are given in separate chapters.

2.1 Calculational Procedure

For the exchange correlation potential we have used the form of Gunnarsson and Lundqvist [15]. The core states are solved in every iteration step with the scalar relativistic formalism (only ignoring the effect of spin-orbit interaction). The Muffin-Tin (MT) radii are determined so that the core electrons stay inside the MT spheres as well as the MT spheres do not overlap with each other. The basis functions in the MT spheres are constructed by spherical harmonics with $l \leq 7$. We consider the reciprocal lattice vectors $\boldsymbol{K}$ satisfying $|\boldsymbol{k} + \boldsymbol{K}| < |\boldsymbol{K}|_{\max}$ whose value is chosen so that the number of APWs per one atom is almost the same for each compound and for each structure. The charge density inside the MT spheres is expanded in spherical harmonics up to $l \leq 7$ and in the interstitial region it is expanded by plane waves each of which satisfy $|\boldsymbol{k}| < 2|\boldsymbol{K}|_{\max}$. In every iteration step for self-consistency the charge density is calculated by using an appropriate number of sampling point in the reduced zone of the first Brillouin zone. Finally we

repeat the iteration until the r.m.s. difference between input potential and output potential becomes smaller than 10^{-5}Ryd.

FLAPW band calculations are performed for the whole series of MNs with NaCl-type crystal structure (space group $O_{\rm h}^5$) as well as with ZnS-type structure (space group $T_{\rm d}^2$). Calculations are carried out also for FeN and Fe with the structures specified by space groups, $D_{\rm 3d}^6$, $D_{\rm 3d}^5$, $D_{\rm 4h}^{17}$ and $D_{\rm 4h}^1$. In Table 2.1 we list our calculational criteria used for each structure such as the MT radius, the number of sampling $\boldsymbol{k}$ points, the value of $|\boldsymbol{K}|_{\rm max}$ and so on.

2.2 General Aspect of Non-magnetic Band Structure of MNs

We have performed band calculations for the whole series of MN with the NaCl-type structure. As an example of the non-magnetic band structures of NaCl-type MN the energy dispersion curves along the symmetry lines and the density-of-states (DOS) obtained for NaCl-type FeN are shown in Figs. 2.1 and 2.2. The lowest-lying band in the figure is the $2s$ states of N atoms. The energy region separated by a large gap above the $2s$ band contains mainly bonding states of the metal $3d\gamma$ and the N $2p$ orbitals, and its counterpart, namely the anti-bonding bands are located at the highest energy region in the figure. The intermediate region between the bonding and the anti-bonding bands consists mainly of the metal $3d\varepsilon$ states. Here we note that the shape of the DOS for MN is quite similar to each other and only the Fermi energy is shifted according to different number of $3d$ electrons. In this sense the rigid-band model can be applicable well for NaCl-type MN.

Before proceeding to the band structures of ZnS-type MN we describe the band structure of NaCl-type ScN in more detail. Figure 2.3 shows the DOS of NaCl-type ScN enlarged in scale around the Fermi level. The valence bands consist of the Sc $d\gamma$ and the N $2p$ states, and main component of the lower part of the valence bands is the Sc $d\varepsilon$ state. As it can be seen from the figure, at the Γ point there is a small hole pocket of the valence band which consists almost of the N $2p$ states, and at the X point there is a small electron pocket. Although this overlap is very small, our band calculations give a semimetallic behavior for NaCl-type ScN. This result contradicts with the experimental result that ScN is a semiconductor with a band gap of 2.1 eV ($\sim$0.15 Ryd) [3]. This discrepancy may be ascribed to LDA itself because this approximation usually underestimates the gap energy.

Recently it is reported that FeN and CoN with the ZnS-type structure have been synthesized. Hence we have performed band calculations also for ZnS-type MnN, FeN, CoN, NiN and CuN. As an example of the non-magnetic band structure of ZnS-type MN the dispersion curves and the DOS of FeN is shown in Figs. 2.4 and 2.5. The lowest band in the figure consists again of the $2s$ states of N atoms. Separated by a large gap above this $2s$ band there are hybridized bands of the metal $3d\varepsilon$ state and the N $2p$ state (bonding bands). The two bands separated by a small gap above this bonding bands consist mainly of the metal $3d\gamma$ states, and the highest bands are the anti-bonding states of the $3d\varepsilon$-$2p$ hybridized bands. From comparison with the band structures of NaCl-type MN it is clearly seen that the nature of hybridization between $3d$ and $2p$ states is different for NaCl-type and ZnS-type. This difference originates from the different coordinate of the N atoms around metal atoms in respective structure, *i.e.* they are located at the octahedral sites in NaCl-type whereas at the tetrahedral sites in ZnS-type. It is finally noted that the rigid-band model can be applicable also for ZnS-type MNs.

Table 2.1: Criteria of FLAPW band calculations. r_{MT} is the Muffin-Tin radius in unit of $|\boldsymbol{a}|$. The unit of $|\boldsymbol{K}|_{\max}$ is $|\boldsymbol{a}^*|$. The symbol "N", "F" and "A" indicate non-magnetic, ferromagnetic and antiferromagnetic state, respectively.

space group		r_{MT}		sampling point($\boldsymbol{k}$)	Number of APW		Number of P.W. expanding charge
		Metal	N		$\lvert\boldsymbol{K}\rvert_{\max}$	at Γ point	
O_{h}^5(NaCl)	ScN∼CuN	0.27	0.18	85	5.8	181	1639
T_{d}^2(ZnS)	ScN∼CuN	0.234	0.155	85	5.8	181	3007
$D_{3\mathrm{d}}^6$	FeN(N,F)	0.35	0.30	85	3.61	409	3037
	Fe(N,F)	∼0.5		85	2.74	203	1265
$D_{3\mathrm{d}}^5$	FeN(A)	0.35	0.30	85	3.61	409	3471
	Fe(A)	∼0.5		85	2.74	203	1503
$D_{4\mathrm{h}}^{17}$	FeN(N,F)	∼0.382	∼0.255	115	4.1	181	1639
	Fe(N,F)	∼0.382		115	4.15	181	1687
$D_{4\mathrm{h}}^1$	FeN(A)	∼0.382	∼0.255	75	4.15	403	3379
	Fe(A)	∼0.382		75	4.15	403	3379

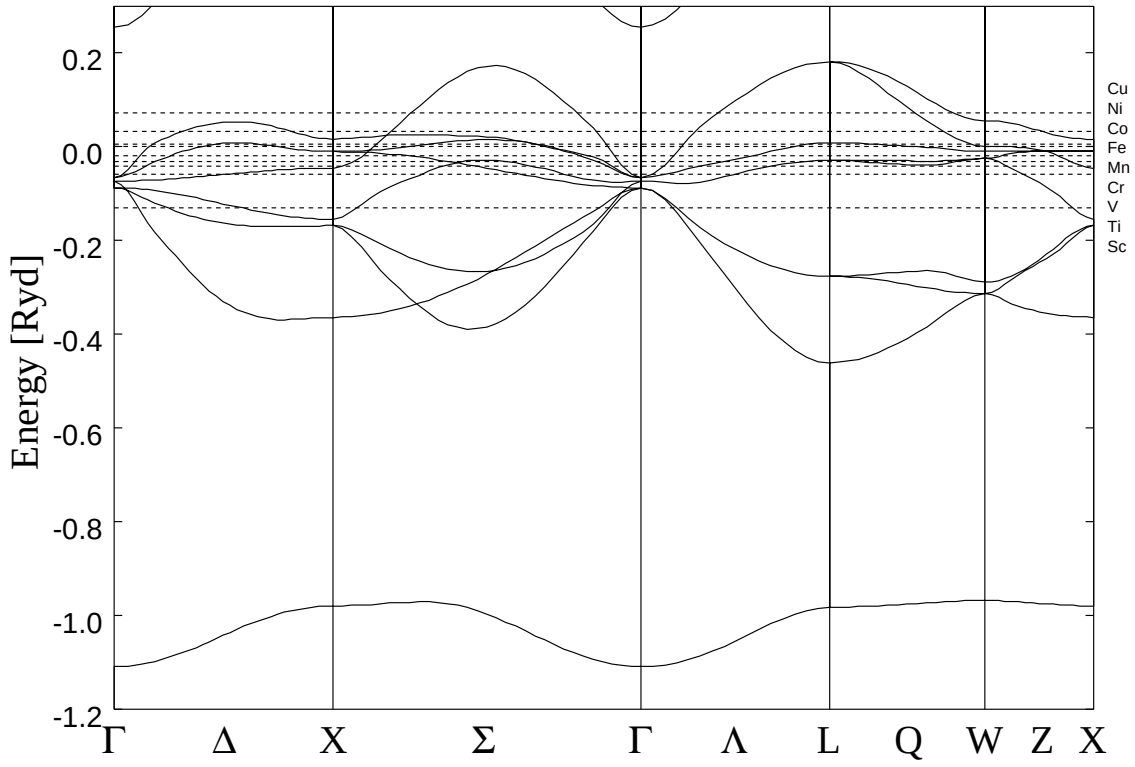

Figure 2.1: Electronic band structure of non-magnetic state of NaCl-type FeN with lattice constant a=4.00Å. If we shift the Fermi level according to the valence electron number, we could get the band structure of each MNs. The dotted lines indicate the Fermi level of MN other than FeN. Energy origin is set at the Fermi level of FeN.

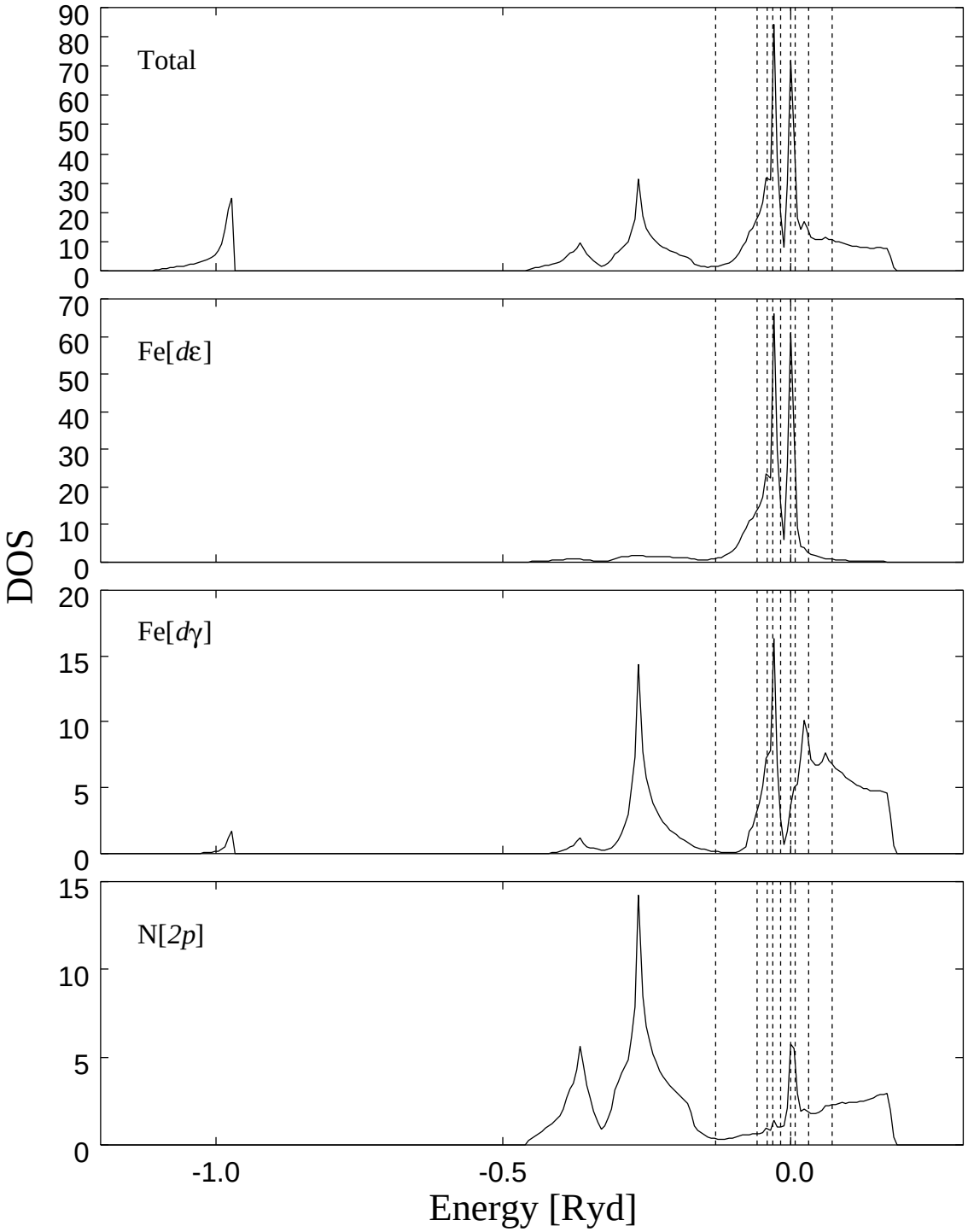

Figure 2.2: Density of states of non-magnetic state of NaCl-type FeN with lattice constant a=4.00Å. The unit of DOS is states/Ryd per formula unit and per spin. If we shift the Fermi level according to the valence electron number, we could get the DOS of each MNs. The dotted lines indicate the Fermi level of MN other than FeN. Energy origin is set at the Fermi level of FeN.

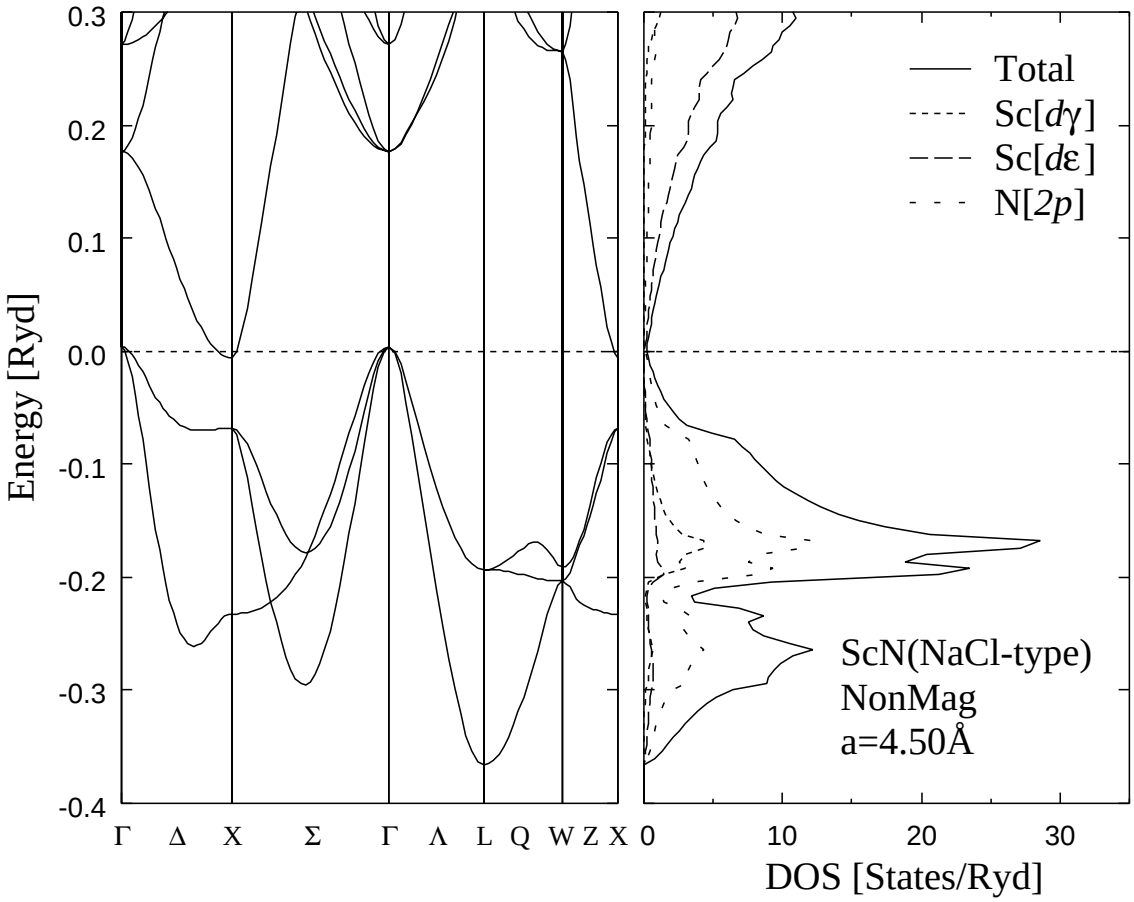

Figure 2.3: The dispersion curves and the DOS of NaCl-type ScN enlarged in scale around the Fermi level.

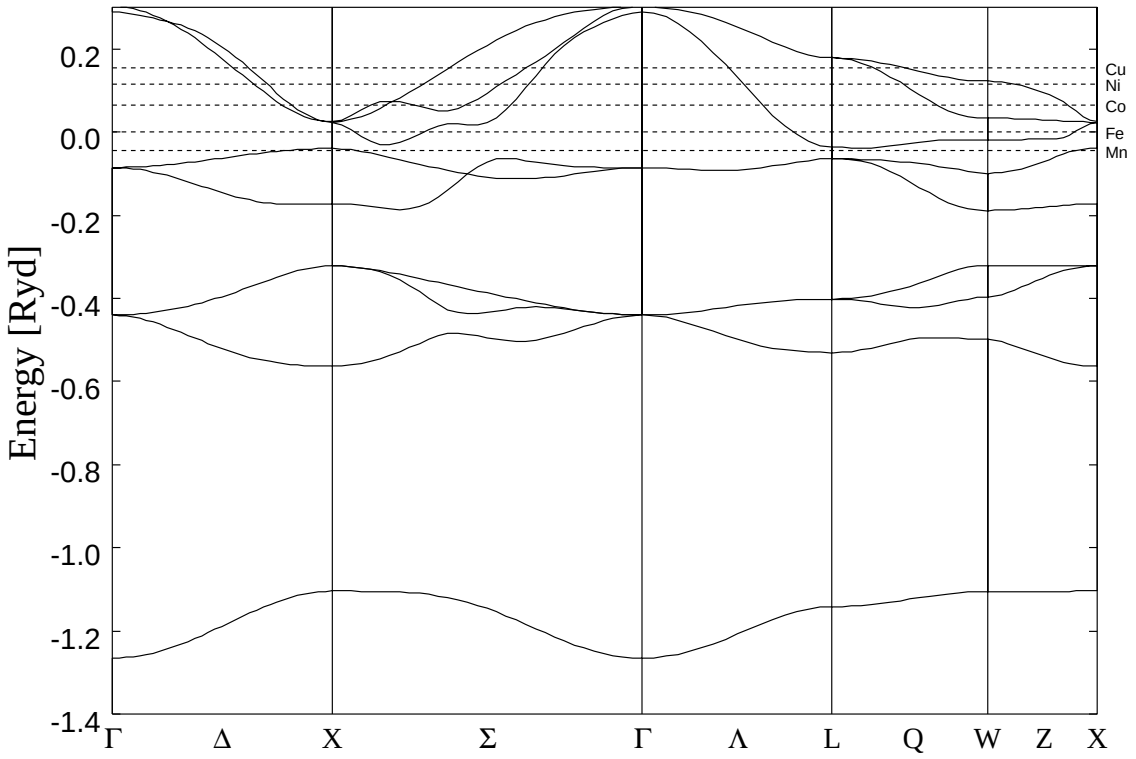

Figure 2.4: Electronic band structure of non-magnetic state of ZnS-type FeN with lattice constant a=4.20Å. If we shift the Fermi level according to the valence electron number, we could get the band structure of each MNs. The dotted lines indicate the Fermi level of MN other than FeN. Energy origin is set at the Fermi level of FeN.

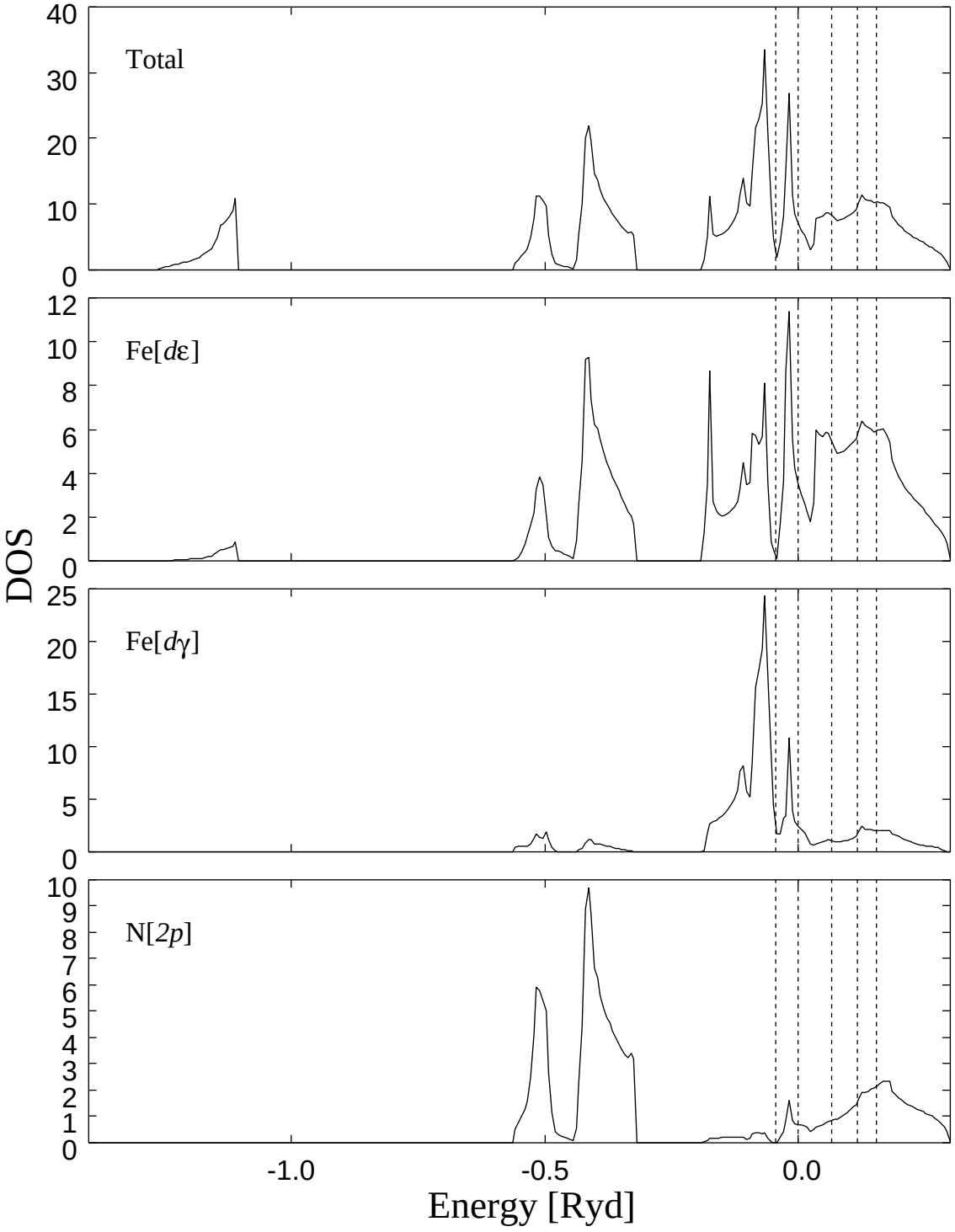

Figure 2.5: Density of States of non-magnetic state of ZnS-type FeN with lattice constant a=4.20Å. The unit of DOS is states/Ryd per formula unit and per spin. If we shift the Fermi level according to the valence electron number, we could get the DOS of each MNs. The dotted lines indicate the Fermi level of MN other than FeN. Energy origin is set at the Fermi level of FeN.

Chapter 3

Calculational Results for MNs except for FeN

3.1 ScN, TiN, VN and CrN

3.1.1 Lattice Constant and Bulk Modulus

In order to estimate the equilibrium lattice constant (a_0) at T=0 K for ScN, TiN, VN and CrN we have calculated the total energy of the non-magnetic state for each compound as a function of volume. We considered only the NaCl-type crystal structure because ScN∼CrN have been reported to have the NaCl-type crystal structure in the non-magnetic state. The equilibrium lattice constant or the equilibrium volume is estimated as follows. First we calculate the total energy E for several discrete values of unit cell volume v, and then the calculated energies are fitted to the Murnaghan equation of states [16] expressed by

$$E = \frac{cv}{ck}\left\{\frac{1}{ck-1}\left(\frac{v_0}{v}\right)^{ck} + 1\right\} + const. \tag{3.1}$$

Three parameters, v_0, c and k, in the above equation are determined by a least-square method. Here it is noted that v_0 represents the equilibrium unit cell volume and c the bulk modulus. The derivation of the Murnaghan equation of states is given in Appendix A.

As an example of the total energy as a function of the unit cell volume we show in Fig. 3.1 the total energy calculated for ScN and the results fitted to the Murnaghan equation of states. The value of v_0 is determined as v_0=23.4Å^3/ScN , and we obtain the equilibrium lattice constant a_0=4.54Å. The equilibrium lattice constants for

TiN, VN and CrN have been determined in the same way, and the results are shown in Fig. 3.2 and Table 3.1 together with the experimental results. We can see the theoretical results are in good agreement with the experimental ones. Therefore we can regard that the FLAPW method is a quite useful method to estimate properly the equilibrium lattice constant of MNs. A little bit large discrepancy between the theoretical and the experimental results for CrN may be ascribed to the fact that CrN becomes an antiferromagnet with orthorhombic symmetry below T_{N}=273 K.

It has been said that these nitrides display a refractory property, which is related to the bulk modulus. Therefore we have estimated also the bulk modulus for each of these compounds from the total-energy curve as a function of the unit cell volume. For TiN bulk modulus becomes 3.05 Mbar from our estimation. This result is in good agreement with the experiment. For VN our estimated value is about two times as large than experimental value. The results of the equilibrium lattice constant and the bulk moduli are given in Table 3.1. We see a trend that mixing with N atoms make these transition metals hard. We could naively understand this trend as follows. NaCl-type and ZnS-type MN can be regarded to be obtained from fcc transition metals by N atoms occupying the octahedral or the tetrahedral interstitial site of the fcc structure. Then the distance between the nearest neighboring atoms is shortened. Of course the lattice is expanded by the occupancy, but the expansion is not so large to compensate the shortening of the nearest-neighboring interatomic distance. As the results the metal atoms are not able to move easily from their equilibrium position, *i.e.* it becomes hard. Although not all of the transition-metals have the fcc structure in its single crystal phase, it could be seen generally that the distance of the nearest neighboring transition-metal atoms is somewhat expanded from its single phase value but the distance between the metal atom and the N atom is shorter than the distance of the nearest neighboring transition-metal atoms of its single crystal phase [17].

3.1.2 Magnetism

To study the magnetic properties of these four compounds we first calculated the total and the partial density-of-states (DOS) of the non-magnetic state for the equilibrium lattice constant. The results are shown in Figs. 3.4, 3.5, 3.6 and 3.7. It is clearly seen that the shape of DOS is similar with each other, and therefore the rigid-band model can be applied well. In order to investigate the effect of the Fermi surface nesting we have calculated also the generalized electronic susceptibility

$\chi_0(\boldsymbol{q})$, which is defined by,

$$\chi_0(\boldsymbol{q}) = \sum_{\boldsymbol{k}} \sum_{n,m} \frac{f(\varepsilon_{n\boldsymbol{k}}) - f(\varepsilon_{m\boldsymbol{k}+\boldsymbol{q}})}{\varepsilon_{m\boldsymbol{k}+\boldsymbol{q}} - \varepsilon_{n\boldsymbol{k}}}. \tag{3.2}$$

here $\varepsilon_{n\boldsymbol{k}}$ denotes the band energy of wave vector $\boldsymbol{k}$ and band suffix n, and $f(\varepsilon_{n\boldsymbol{k}})$ represents Fermi distribution function. From the calculational results of $\chi_0(\boldsymbol{q})$ we may get information about the wave vectors which specify possible magnetic states. Moreover we have calculated the total energy of the ferromagnetic state for each compound and compared the result with that of the non-magnetic state.

For NaCl-type ScN the Fermi level is located at the bottom of the DOS. So that the DOS at the Fermi level, $N(\varepsilon_{\mathrm{F}})$, is very small, that is $N(\varepsilon_{\mathrm{F}})$=0.1 states/Ryd·spin. As mentioned previously ScN is semiconducting experimentally. From these theoretical and experimental results ScN is expected not to order magnetically. For completeness we have performed ferromagnetic band calculations for the equilibrium lattice constant of the non-magnetic state, but no self-consistent solution has been obtained.

For both TiN and VN the Fermi level lies at the slope of the DOS. The values of $N(\varepsilon_{\mathrm{F}})$ are 4.2 and 10.3 states/Ryd·spin for TiN and VN, respectively. The value of 4.2 is rather small to satisfy the Stoner condition of ferromagnetism, $N(\varepsilon_{\mathrm{F}}) \times I > 1$ with I being the exchange interaction energy, if we use tentatively the value of $I \sim 50$ mRyd) estimated for single crystal of Ti [17]. Certainly no self-consistent solution has not been obtained for ferromagnetic band calculations for TiN. For VN the value of $N(\varepsilon_{\mathrm{F}})$ is also small to satisfy the Stoner condition and ferromagnetic band calculations have no solution again. Furthermore, $\chi_0(\boldsymbol{q})$ calculated for TiN and VN does not have any large peak as a function of $\boldsymbol{q}$ (see Fig. 3.8 for TiN and VN). From these reasons we could conclude that both TiN and VN do not have any kind of magnetic ordered state. This result is consistent with the experiment.

The Fermi level of CrN is located at one of the peaks of DOS and we obtain a fairly large value of $N(\varepsilon_{\mathrm{F}})$, that is, $N(\varepsilon_{\mathrm{F}})$=27.1 states/Ryd·spin. This suggests a possibility that CrN may have a certain kind of magnetic ordered state. In fact we have carried out tentatively ferromagnetic band calculations and obtained certainly a self-consistent solution. The obtained ferromagnetic moment is about $1.27\mu_{\mathrm{B}}$/Cr, and the total energy of the ferromagnetic state is lower by about $\sim$5 mRyd/CrN

(Fig. 3.9) than that of the non-magnetic state. Experimentally CrN becomes an antiferromagnet below $T_{\rm N}$=273 K with accompanying orthorhombic distortion from the NaCl-type structure ($O_{\rm h}^5 \rightarrow D_{\rm 2h}^{16}$) [5]. The antiferromagnetic structure of this compound is rather complicated [5]. If we ignore the orthorhombic distortion and take a unit cell of the cubic structure, the CrN's magnetic structure is illustrated as shown in Fig. 3.3. Such a magnetic structure cannot be described by a single $\boldsymbol{q}$. Band structure calculations for this complicated magnetic structure of CrN have been done already by Mavromaras *et.al.* [6].

3.2 MnN, CoN, NiN and CuN

We have seen in the previous section that the FLAPW method can give the equilibrium lattice constants which are in good agreement with those observed for ScN, TiN, VN and CrN. In this section we carry out in detail the FLAPW band calculations for MnN, CoN, NiN and CuN which have not been synthesized yet except CoN. The equilibrium lattice constants are evaluated and magnetic properties are discussed. The calculations are performed for both the NaCl-type and the ZnS-type crystal structures because it has been reported that CoN has the ZnS-type structure [11]. As for FeN, its electronic, structural and magnetic properties are investigated in detail in the following chapter.

3.2.1 Lattice Constant and Equilibrium State

The equilibrium lattice constants of the non-magnetic state evaluated for both the NaCl-type and the ZnS-type structures are shown in Fig. 3.2 and Table 3.1. For ZnS-type CoN the theoretical value agrees well with the experimental one.

Looking around Fig. 3.2, two remarks should be mentioned. First, as a function of atomic number of the transition metal the equilibrium lattice constant has the minimum value at CoN for both the structures. Secondly, the equilibrium lattice constants of ZnS-type MNs are larger by about 0.3Å than those of NaCl-type MNs. In ZnS-type MNs, the N atoms are located at the tetrahedral site of the fcc structure of transition-metal atoms. This site is rather closer to neighboring transition-metal atoms compared with the octahedral site of the N atoms in the NaCl-type structure. In this sense it seems reasonable that we have obtained larger lattice constants for ZnS-type MNs.

The structural difference between NaCl-type and ZnS-type MNs is the relative

position of N atom to transition-metal atom (octahedral site for NaCl-type and tetrahedral site for ZnS-type), and it is interesting to clarify which structure is energetically favorable. Therefore, for each MN (M = Mn, Co, Ni, Cu) we have compared the total energy at the respective equilibrium lattice constant of the NaCl-type and the ZnS-type structures. As the results, we have found that for all the four compounds the NaCl-type structure is more stable than the ZnS-type one (see Table 3.2). It is noted, however, that for CoN the total energy of the ZnS-type structure is almost the same as that of the NaCl-type one if we consider the numerical accuracy.

We have calculated also the bulk modulus of the four compounds for both the structures. The results are given in Table 3.1 together with the bulk modulus obtained for fcc transition metals themselves. We see again that mixing with N atoms makes the transition metals hard also for Mn, Co, Ni and Cu. This will be understood by the same discussion as given in the previous section.

3.2.2 Magnetism

Next we have investigated the possibility of appearance of magnetic ordered state in these four compounds. The DOSs at the Fermi energy of the non-magnetic state of NaCl-type MnN, CoN, NiN and CuN are $N(\varepsilon_{\rm F})$=33.7, 24.1, 9.1 and 6.1 states/Ryd·spin, respectively. On the other hand, for ZnS-type MnN, CoN, NiN and CuN they are $N(\varepsilon_{\rm F})$=4.5, 7.7, 10.7 and 7.8 states/Ryd·spin, respectively. These values are obtained for the equilibrium lattice constant of the respective structure. The NaCl-type MNs have rather large values of $N(\varepsilon_{\rm F})$. But it should be noted that if we decompose $N(\varepsilon_{\rm F})$ into the partial DOS, the $3d$-component of the transition-metal is not so large. In fact, ferromagnetic band calculations have obtained no self-consistent solution except for NaCl-type CoN. Furthermore, the calculated values of $\chi_0(\boldsymbol{q})$ are rather small and it has no particular peak as a function of wave vector $\boldsymbol{q}$. Therefore we cannot expect any magnetic ordered state except for NaCl-type CoN.

For NaCl-type CoN we obtain a ferromagnetic self-consistent solution and the calculated magnetic moment is about $0.15\mu_{\rm B}$/Co. Furthermore, from comparison of the total energy it has been found that the ferromagnetic state is more stable than the non-magnetic state. This result appears to contradict with the experimental result that CoN is paramagnetic and has the ZnS-type structure [11]. Here it should be noted, however, that the sample of CoN used for the experiment has been grown by using Cu substrate. Therefore it is considered that there is a large misfit of the lattice constant. Thus we would like to say that if a pure bulk sample of CoN is

synthesized it may have the NaCl-type structure and show some kind of magnetic order, at least ferromagnetic order. Further experimental study is desired.

Table 3.1: Equilibrium lattice constant of MNs (in unit of Å). For TiN and VN the last column is experimental value of the bulk modulus for each compounds. The last column of FeN is our calculated value of the bulk modulus for non-magnetic state fcc Fe. For other metals the last column is calculated value of the bulk modulus for single phase of transition-metal in non-magnetic state with fcc structure referred from [17]. The unit of bulk modulus is Mbar.

		Lattice Constant		Bulk Modulus	
		Calc.	Exp.	Calc.	
ScN		4.54	4.50[18]	2.18	0.57
TiN		4.24	4.24[19]	3.05	2.88
VN		4.07	4.13[20]	4.14	2.33[21]
CrN		4.00	4.15[5]	3.90	2.70[21]
MnN	NaCl	3.95		4.43	2.91
	ZnS	4.30		3.51	
FeN	NaCl	4.00	4.5[9]	3.49	3.05
	ZnS	4.24	4.33[9]	3.73	
			4.307[10]		
CoN	NaCl	3.90		4.82	2.84
	ZnS	4.20	4.29[11]	2.45	
NiN	NaCl	3.96		3.20	2.20
	ZnS	4.26		3.44	
CuN	NaCl	4.05		3.07	1.55
	ZnS	4.34		3.05	

Table 3.2: Stable state of transition-metal mononitrides. Total energy is lower in right hand side than left hand side. The lattice constant is chosen as the equilibrium one in the non-magnetic state.

	unstable	stable
MnN	ZnS-type(NonMag)	NaCl-type(NonMag)
CoN	ZnS-type(NonMag)$\sim$NaCl-type(NonMag)	NaCl-type(Ferro)
NiN	ZnS-type(NonMag)	NaCl-type(NonMag)
CuN	ZnS-type(NonMag)	NaCl-type(NonMag)

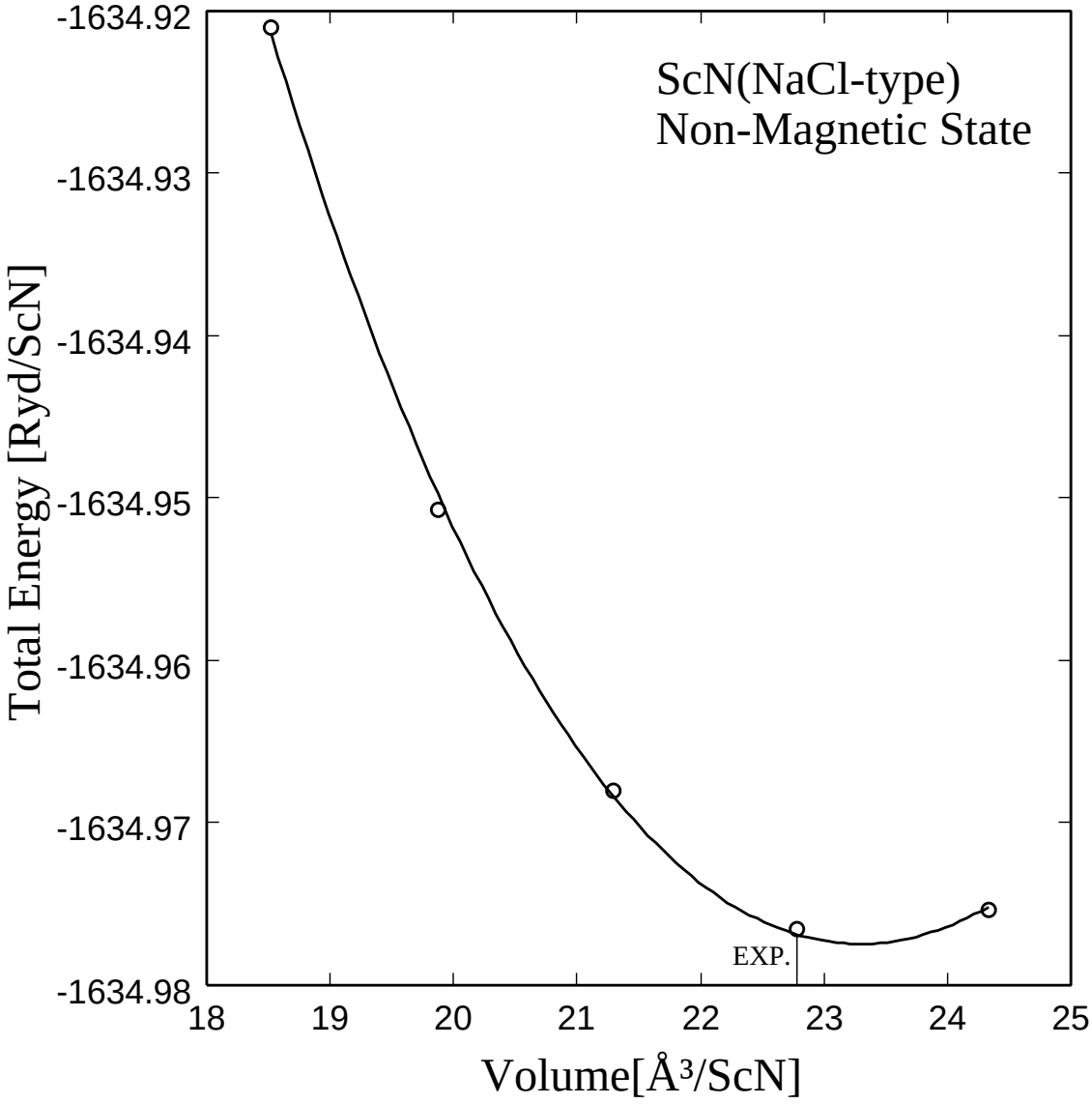

Figure 3.1: Total energy of non-magnetic state NaCl-type ScN as a function of unit cell volume.

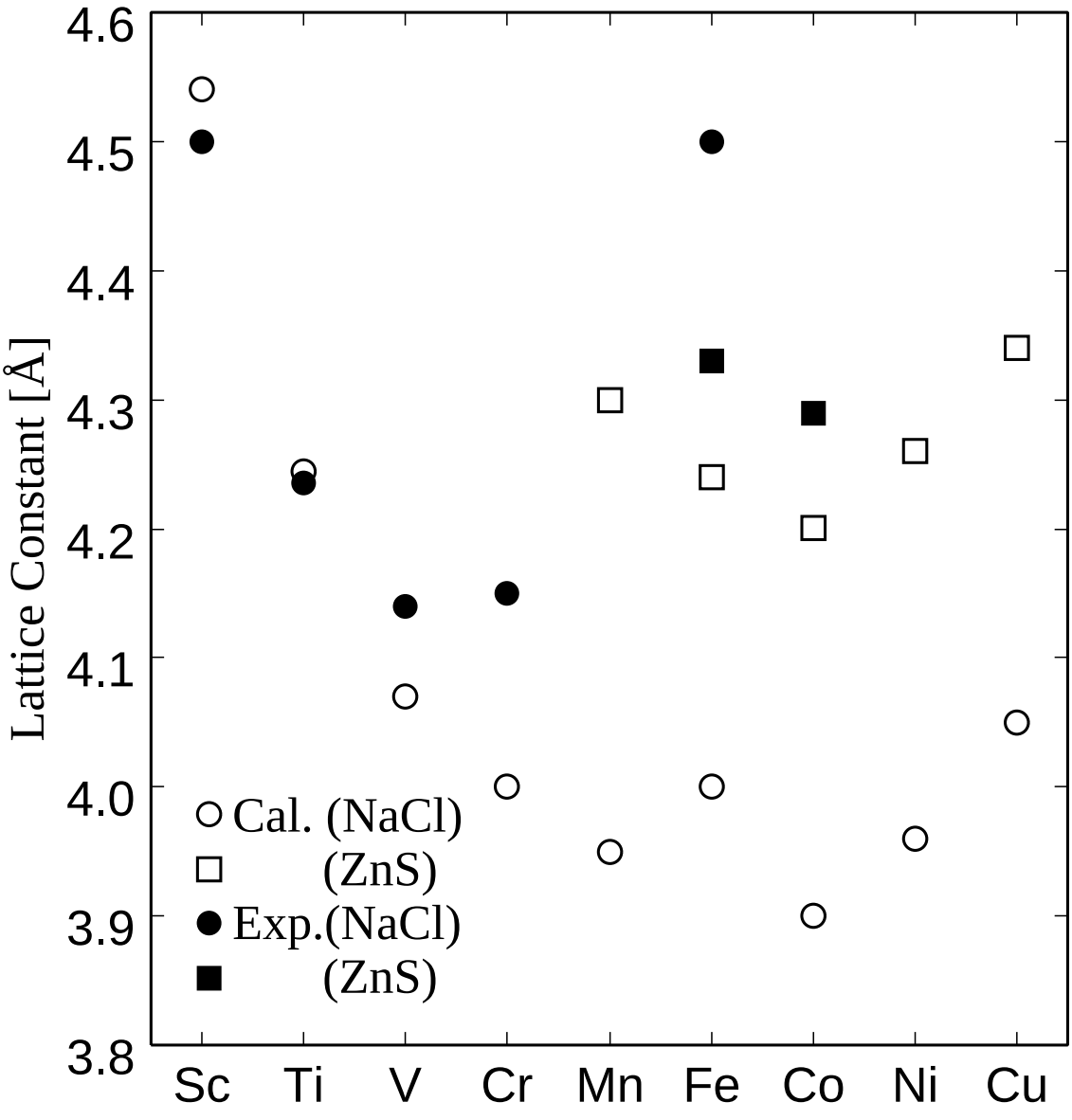

Figure 3.2: Equilibrium lattice constant of MNs

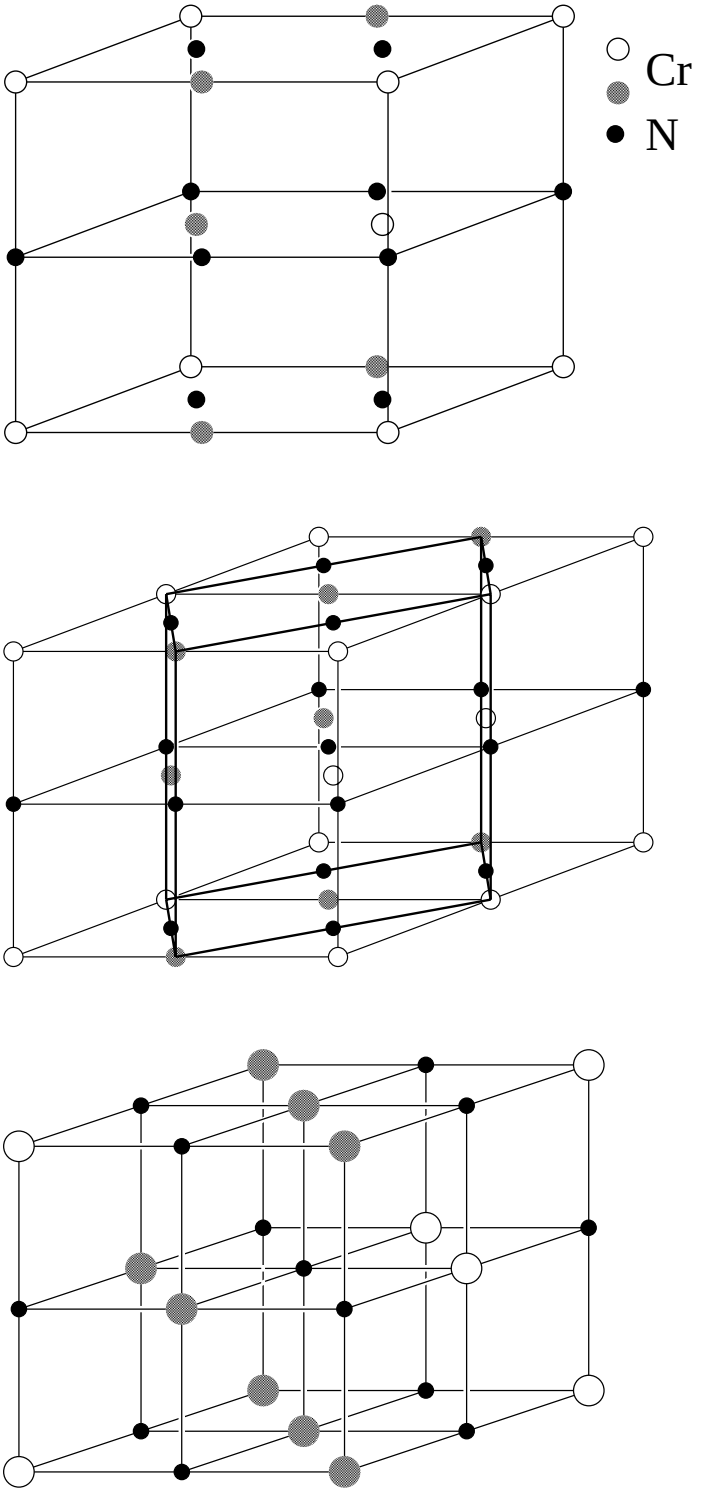

Figure 3.3: Upper panel is a unit cell of antiferromagnetic state of CrN, middle one is a cell which is doubled in volume. Thick line is a unit cell in cubic symmetry. A unit cell in cubic symmetry is shown in the lower panel in which orthorhombic distortion is neglected. The two kind of big circles are chromium atoms whose spin directions are antiparallel each other.

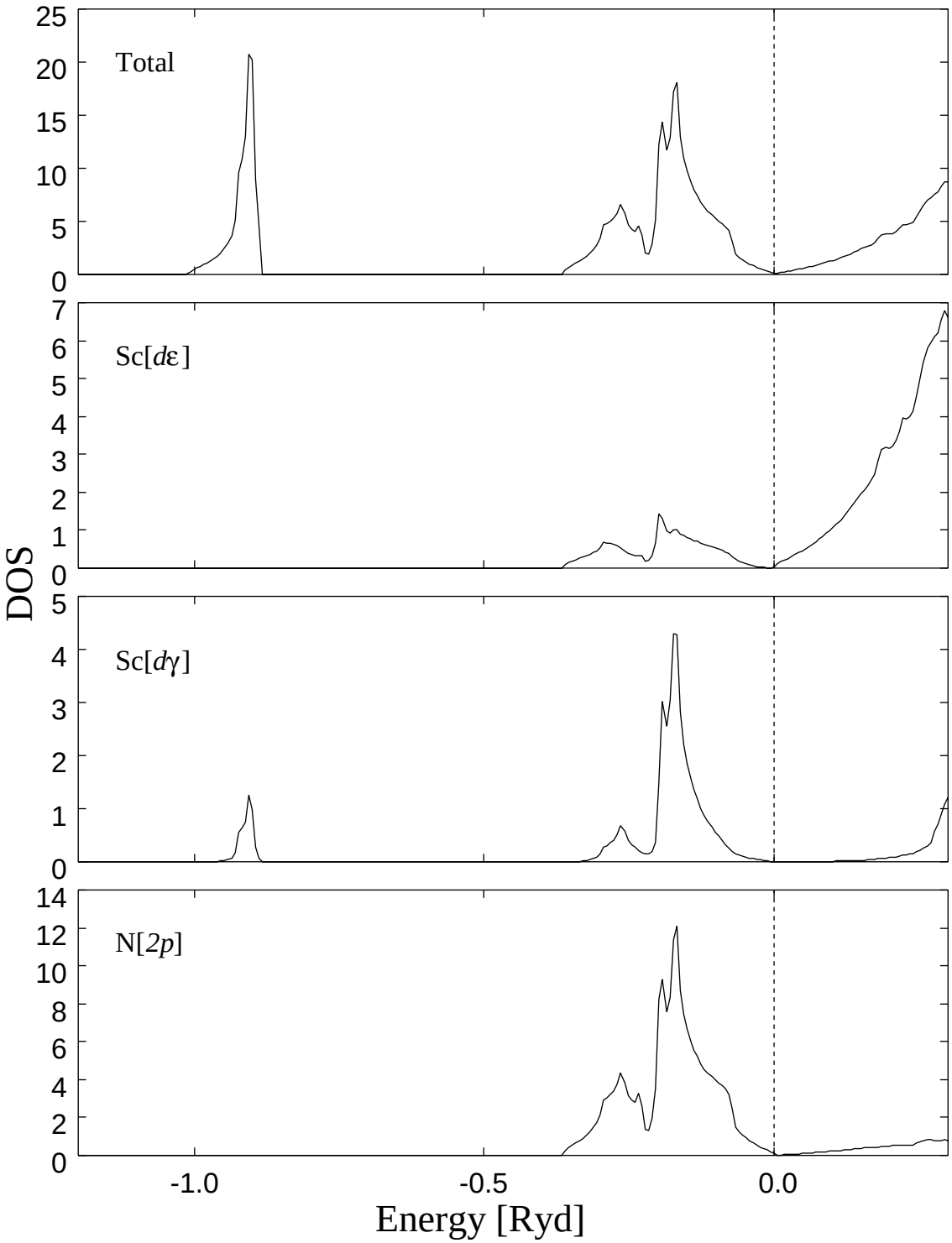

Figure 3.4: Density of states of NaCl-type ScN with lattice constant a=4.50Å in non-magnetic state. The unit of DOS is states/Ryd per formula unit and per spin.

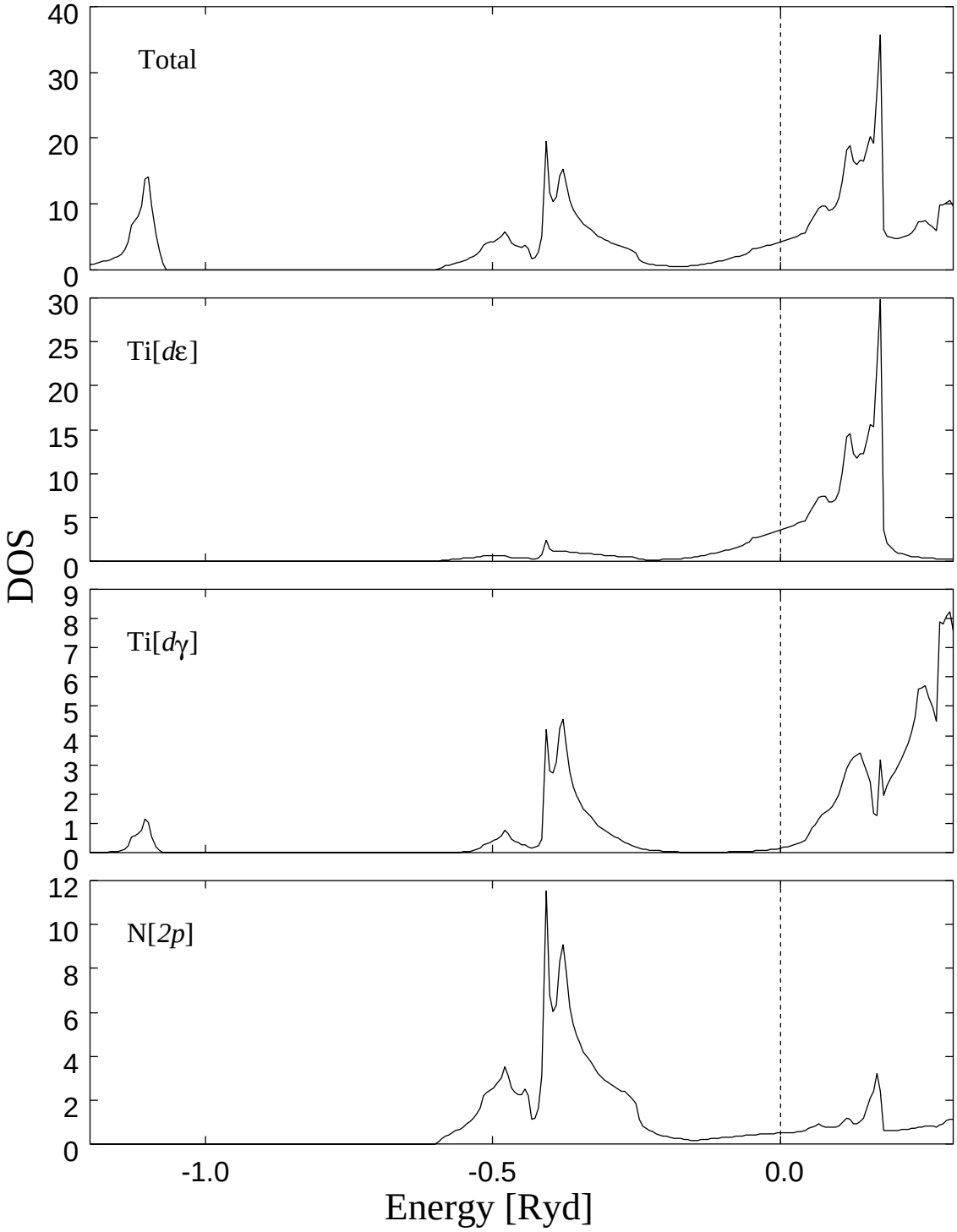

Figure 3.5: Density of states of NaCl-type TiN with lattice constant a=4.23Å in non-magnetic state. The unit of DOS is states/Ryd per formula unit and per spin.

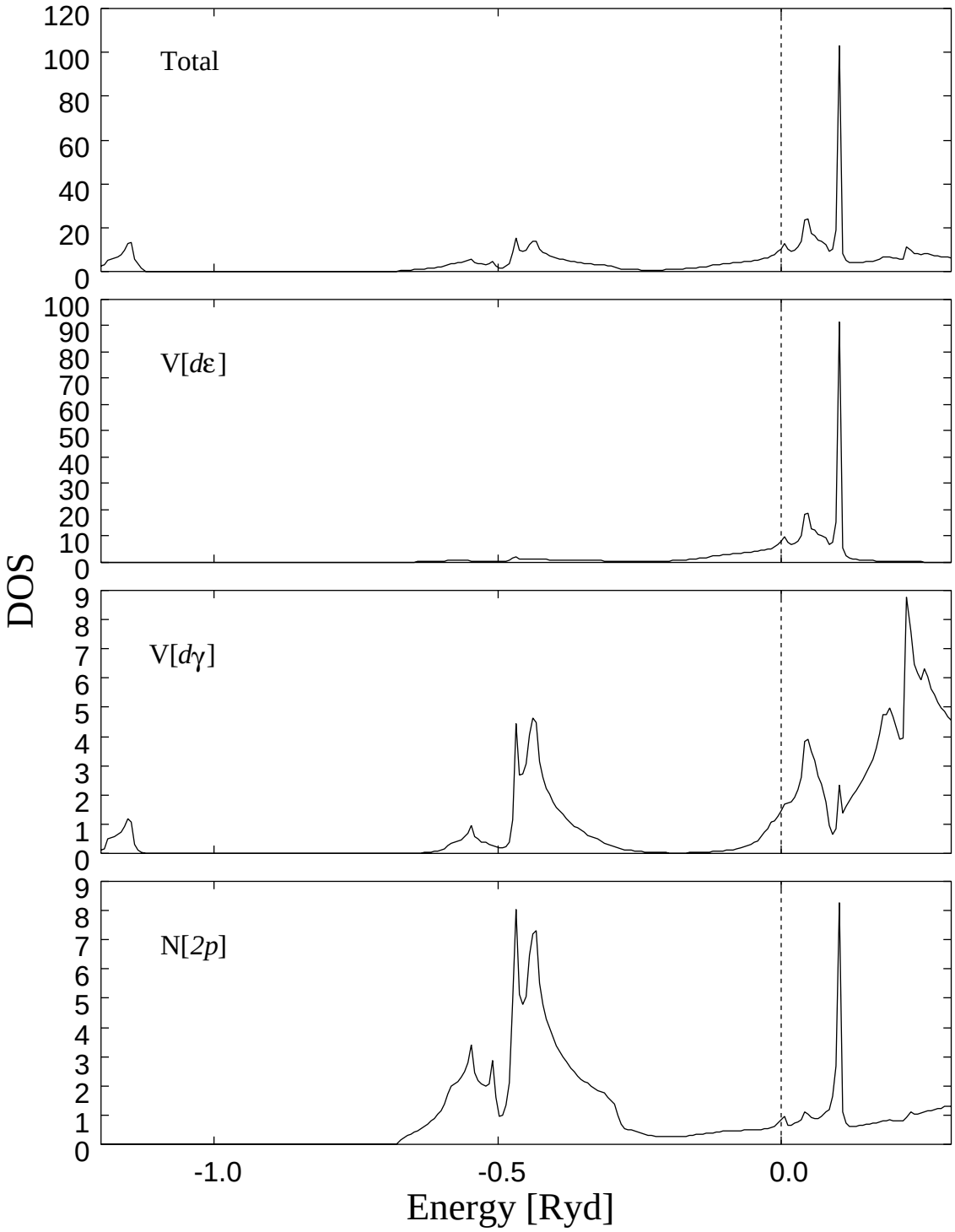

Figure 3.6: Density of States of NaCl-type VN with lattice constant a=4.07Å in non-magnetic state. The unit of DOS is states/Ryd per formula unit and per spin.

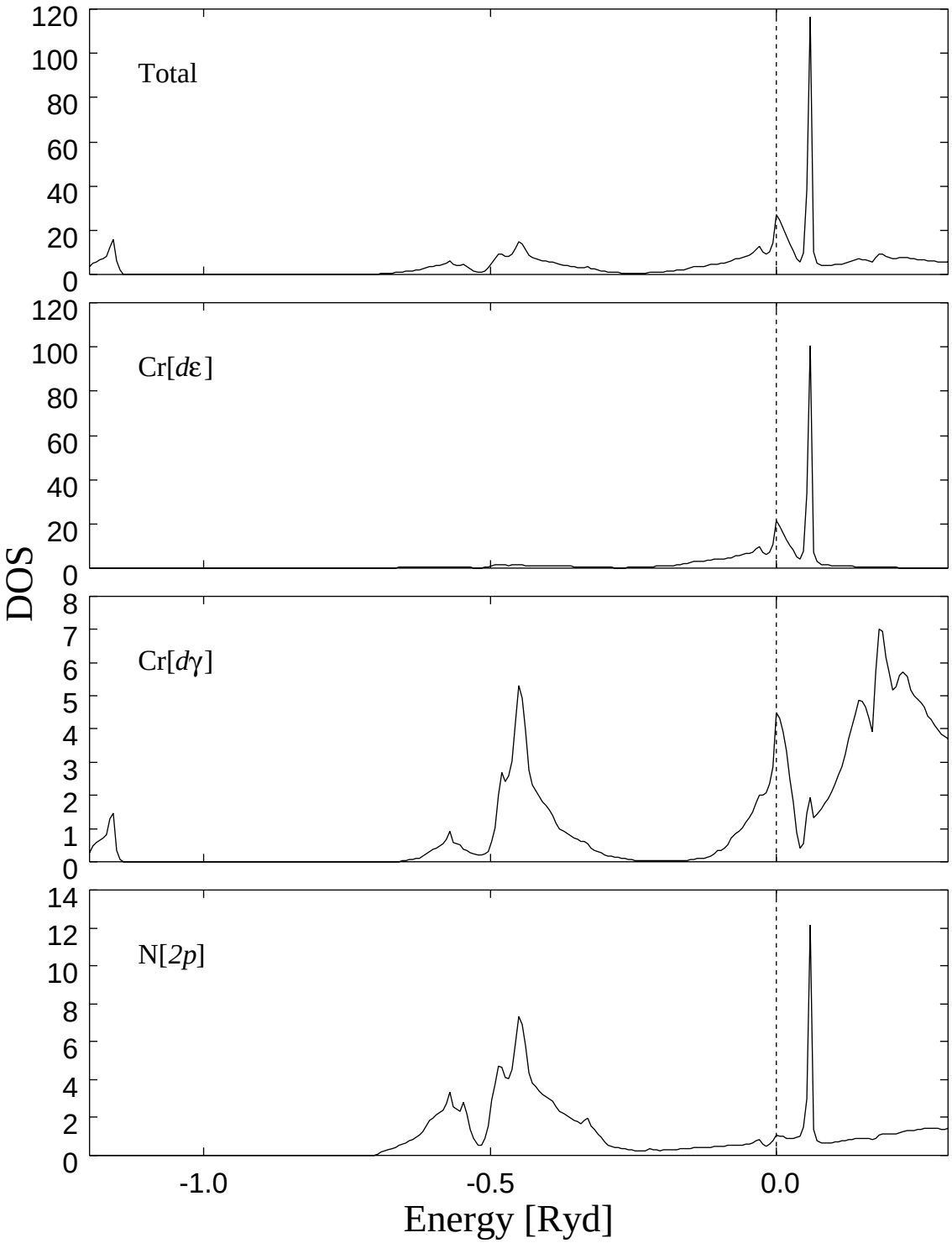

Figure 3.7: Density of states of NaCl-type CrN with lattice constant a=4.00Å in non-magnetic state. The unit of DOS is states/Ryd per formula unit and per spin.

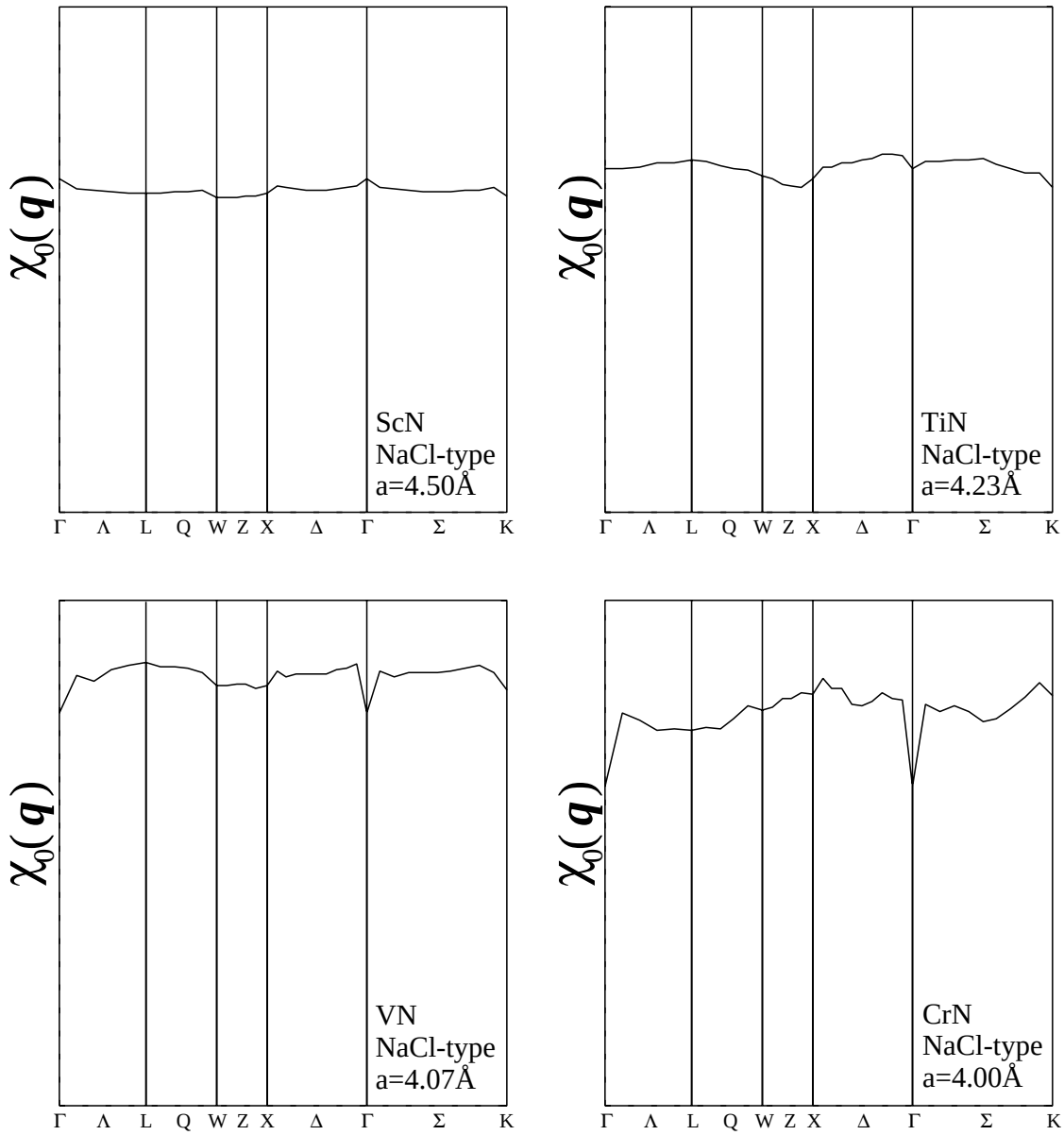

Figure 3.8: Generalized electronic susceptibility $\chi_0(\boldsymbol{q})$ of non-magnetic state of NaCl-type ScN, TiN, VN and CrN. The unit of $\chi_0(\boldsymbol{q})$ is arbitrary.

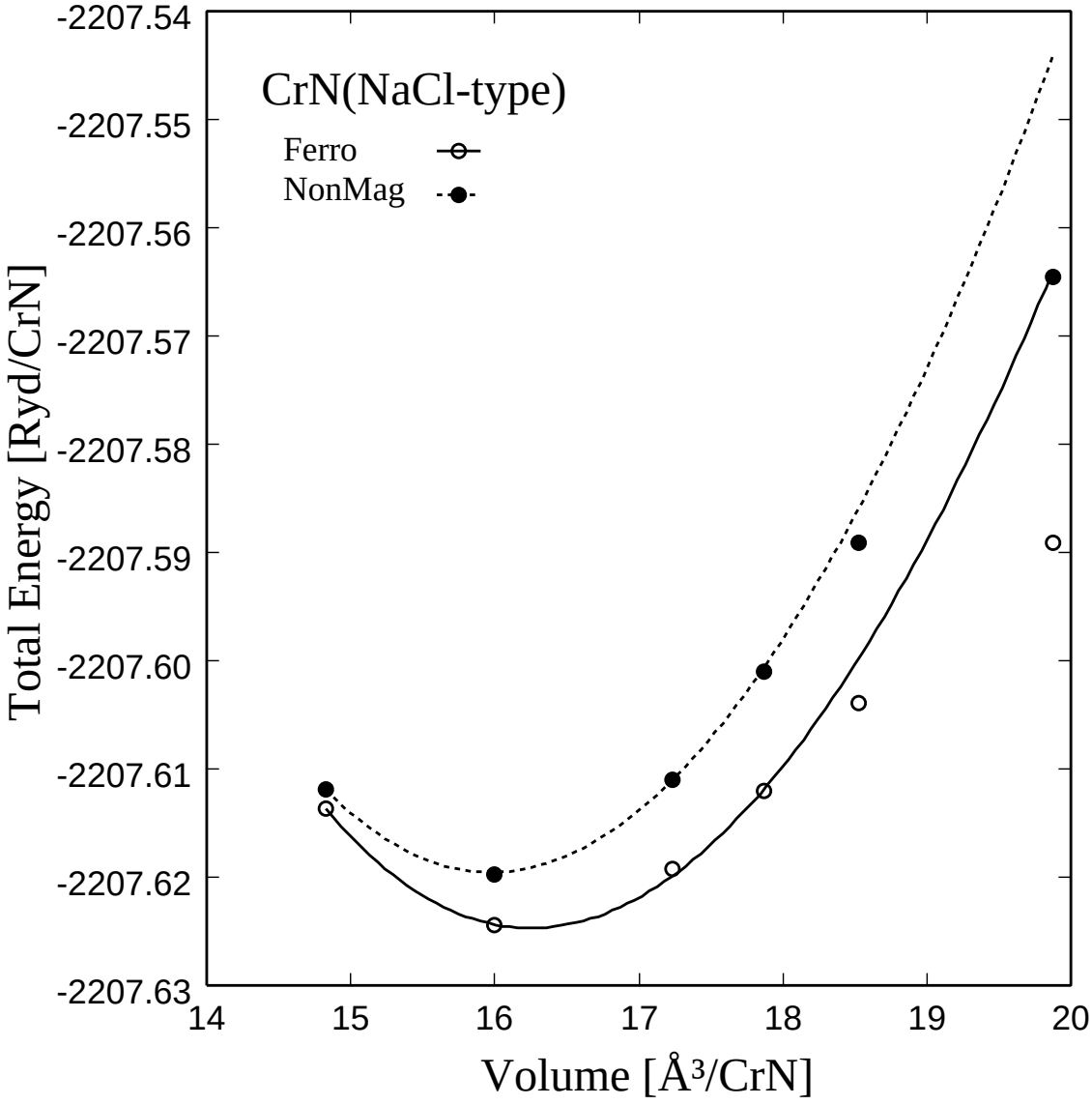

Figure 3.9: Total energy of non-magnetic and ferromagnetic state NaCl-type CrN. The solid and dashed lines are results of the fitting of Murnaghan's equation (A.4).

Chapter 4

Iron Nitride FeN

Iron nitride (FeN) has been reported to have strange properties of taking two kind of crystal structure (NaCl-type and ZnS-type) and having a large lattice constant and two kinds of large hyperfine field at Fe site [9],[10]. It can be seen from Table 3.1 that the observed lattice constant 4.50Å of NaCl-type FeN seems abnormal. Further the observed hyperfine fields are much larger than the experimantal value of α-Fe. In this chapter we try to make clear the origin of these peculiar properties of FeN.

4.1 Equilibrium State of FeN

In order to determine the equilibrium state of FeN, we adopted the same procedure as used in the previous chapter. First we calculate the total energies of NaCl-type and ZnS-type FeN in the non-magnetic state. From the results we estimate the equilibrium lattice constant and bulk modulus. The calculational results are shown in Fig. 3.2 and Table 3.1. Experimentally the lattice constant of NaCl-type FeN has been reported as 4.50Å, which is much larger than the calculated lattice constant 4.00Å. For ZnS-type FeN, on the other hand, the theoretical and experimental results are in good agreement. Comparing the observed lattice constant of NaCl-type FeN with that of other NaCl-type MN, it is hard to believe that the FeN sample used in the experiments has the equilibrium state of its bulk system. Therefore we speculate that such a large lattice constant as observed might be caused by the effects of surface and/or boundary (interface to substrate). In fact the synthesized sample [9] is thin film and have a lot of N atom deficiency.

Next we compare the total energies of NaCl-type and ZnS-type FeN to determine

which structure is more stable. The total energies as a function of unit cell volume are shown in Fig. 4.1. The minimum total energy of NaCl-type FeN is lower than that of ZnS-type FeN, but as seen from the figure the difference between the two is very small ($\sim$0.3 mRyd). Therefore we cannot say conclusively which structure is more stable, if we take account of numerical accuracy of our calculations.

Finally, as seen in other MN, the bulk modulus calculated for NaCl-type and ZnS-type FeN is also larger than that of Fe metal itself (see Table 3.1).

4.2 Magnetism of FeN

Experimentally, it is suggested that NaCl-type FeN is an antiferromagnet. But this suggestion is based only on the results of Mössbauer measurements, which cannot definitely determine a magnetic structure. Therefore, as a first step to get insight into the magnetic structure of NaCl-type FeN from the theoretical side we carry out band calculations for ferromagnetic state and two kinds of antiferromagnetic states specified by $\boldsymbol{q} = [111]$ and $\boldsymbol{q} = [001]$.

If we assume the antiferromagnetic state of $\boldsymbol{q} = [111]$, the space group reduces to trigonal ($D^5_{3\mathrm{d}}$), and if we assume the antiferromagnetic state of $\boldsymbol{q} = [001]$, the space group reduces to tetragonal ($D^1_{4\mathrm{h}}$). Hence this section is divided into three subsections according to the symmetry: section 4.2.1 for cubic, section 4.2.2 for trigonal and section 4.2.3 for tetragonal symmetry. For ZnS-type FeN, it has been reported to be a paramagnet. Therefore it is described in section 4.2.1.

4.2.1 Cubic Symmetry

Fig. 4.2 shows the DOS of non-magnetic state of NaCl-type FeN, which is obtained for the lattice constant a=4.00 Å. It is noted that the overall feature of DOS does not depend sensitively on the value of the lattice constant. Similar to the CrN, the Fermi level lies at one of the peaks of DOS, and the DOS at the Fermi level is large , that is , $N(\varepsilon_{\mathrm{F}})$=38.1 states/Ryd·spin. Hence, if we apply the Stoner's model, we could expect that NaCl-type FeN will have a certain magnetic ordered state. Since we could say nothing about what kind of magnetic order is realized in this compound only from the DOS, we next calculate $\chi_0(\boldsymbol{q})$ for two lattice constant, a=4.00 Å and a=4.50 Å. The results are shown in Fig. 4.3. For a=4.00Å the calculated $\chi_0(\boldsymbol{q})$ has rather flat structure whereas for a=4.50Å it has a peak at the L point ($\boldsymbol{q} = [111]$). This result indicates that if such a large lattice

constant as a=4.50 Å is realized by some reason, an antiferromagnetic structure corresponding to $\boldsymbol{q} = [111]$ is a strong candidate for the stable magnetic state.

If we assume the ferromagnetic state, the cubic symmetry is retained and the calculation can be carried out with use of the cubic symmetry. However, we perform the ferromagnetic band calculations with the hypothetical doubled unit cell, which has the trigonal symmetry, in order that we can make comparison between the ferromagnetic and the antiferromagnetic states on the equal footing. Therefore the results of the ferromagnetic band calculations are presented in the following subsection.

Figure 4.4 shows the DOS of non-magnetic state of ZnS-type FeN, which is obtained for the lattice constant a=4.20 Å. For all values of a, the DOS has a rather small value at the Fermi level, and we could not expect that this compound has any magnetic ordered state. In fact, we made ferromagnetic band calculations, but we were not able to obtain a self-consistent solution. Therefore we conclude that ZnS-type FeN is a paramagnet, which agrees with the experimental result.

Recently Suzuki *et. al.* reported this compound shows mictomagnetism [10]. If this is true, each Fe atom has a magnetic moment and this moment must induce hyperfine field on Fe atom. But according to the result of Mössbauer measurements performed by Nakagawa *et. al.* [9], there is no hyperfine field at Fe site in ZnS-type FeN. Further experiments for this compound are desired.

4.2.2 Trigonal Symmetry

If we assume the $\boldsymbol{q} = [111]$ antiferromagnetic state, Fe in (111)-plane order ferromagnetically and the spin direction alternates every other plane in the [111]-direction. Then, by taking a trigonal unit cell as shown in Fig. 4.5 two Fe atoms are included in the unit cell, one with up-spin and the other with down spin. To make comparison on the equal footing we performed band calculations for the non-magnetic and the ferromagnetic states by taking the same unit cell as that of the $\boldsymbol{q} = [111]$ antiferromagnetic state.

The total energies calculated for the non-magnetic, the ferromagnetic and the antiferromagnetic states are shown as a function of unit cell volume in Fig. 4.6. As seen from the figure the total energy has its minimum value at around a=4.00Å for all the three states. So we are not able to obtain such a large equilibrium lattice constant as a=4.50 Å even if we assume the magnetic states. By comparing the minimum total energies it is found that the ferromagnetic state is the most stable

among the three states. But if we assume the lattice constant of a=4.50 Å, the antiferromagnetic state is more stable than the ferromagnetic state although the energy difference is very small.

We have calculated also the magnetic moment and the hyperfine field on Fe site as a function of the lattice constant or the unit cell volume for both the ferromagnetic and the antiferromagnetic states. The definition of the hyperfine field in this thesis is as follows:

$$H_{\mathrm{HF}} = -\frac{16\pi}{3}\mu_{\mathrm{B}}\left(|\psi_{s\downarrow}(0)|^2 - |\psi_{s\uparrow}(0)|^2\right). \tag{4.1}$$

where μ_{B} is the Bohr magneton and $\psi_{s\sigma}(0)$ represents the value of s-component wave function at the nucleus position. In actual calculations we estimate $\psi_{s\sigma}(0)$ at $r \sim 10^{-4}$au (see Appendix B for details). The calculational results of the magnetic moment and the hyperfine field at Fe site are listed in Table 4.2 as a function of the lattice constant.

It is seen from Table 4.2 that the magnetic moment of Fe atom monotonically increases with increasing the lattice constant in both the ferromagnetic and the antiferromagnetic states. At lattice constant of a=4.00 Å the magnetic moments are 1.34μ_{B} for both the states while at a=4.50 Å they are 3.17 μ_{B} and 3.34 μ_{B} for the ferromagnetic and the antiferromagnetic states, respectively.

In contrast to the magnetic moment the hyperfine field behaves as a function of the lattice constant differently for both the states. This different behavior mainly comes from the difference of the contribution from the valence ($4s$) states. In the ferromagnetic state both contributions from the core and the valence electrons monotonically increase in magnitude with increasing the lattice constant, and as the sum of both the contributions the total hyperfine field becomes a decreasing function of lattice constant. In the antiferromagnetic state, on the other hand, the core contribution increases monotonically while the valence contribution is almost constant, as a function of lattice constant. As the result the total hyperfine field increases with increasing the lattice constant.

The origin of the hyperfine field contributed from core states is understood as follows. The intra-atomic exchange interaction between core and valence $3d$ electron spins is different for down and up spins because of the spin polarization of $3d$ state. This produces distinction for the radial distribution of core states for each spin. The distinction at the nuclear position is the origin of the core state contribution to the hyperfine field. In this thesis the hyper fine field is defined as the equation (4.1) and the sign of hyperfine field contributed from core states becomes "minus". This

means the population of the core states with spin parallel to the magnetic moment is less than that of another spin state at the nuclear position. In contrast to the core state contribution, the valence electron($4s$) contribution is complex to understand. But it is common for both the ferromagnetic and the antiferromagnetic states that the sign of the valence contribution is opposite to that of the core contribution.

At a=4.00 Å ($\sim$ equilibrium lattice constant) the values of hyperfine field of both the ferromagnetic and the antiferromagnetic states are too small to explain the experimental values. It should be noted, however, that if we assume a=4.50 Å and the antiferromagnetic state, the magnitude of the hyperfine field becomes 35 T which is comparable to one of the two observed values, 30 T. Therefore we propose here that the lower field among the observed two hyperfine fields originates from the antiferromagnetic structure with the lattice constant a=4.50 Å, although realization of this lattice constant is open to question. Furthermore the origin of the larger hyperfine field, 49 T, is also open to question.

In order to get insight into the origin of the larger hyperfine field, we investigate effects of N atom deficiencies which are contained in the sample of NaCl-type FeN synthesized by Nakagawa *et. al.* [9]. If all the N atoms are removed from NaCl-type FeN, the remaining Fe atoms form the fcc structure. Then we consider that domains of such fcc Fe may exist if a lot of N atom deficiencies are contained, and we carry out the band calculations for the non-magnetic, the ferromagnetic and the antiferromagnetic states of fcc Fe. The calculations have been performed for the lattice constant a=4.50 Å. The results of calculations such as total energy, magnetic moment and hyperfine field are give in Table 4.1 together with the results for NaCl-type FeN. As seen from the table, for fcc Fe the ferromagnetic state is more stable than the antiferromagnetic state, but the energy difference is very small. Quite interestingly, the magnitude of the hyperfine field at Fe site is 48.2 and 14.8 T for the ferromagnetic and the antiferromagnetic states, respectively. It should be noted that the magnitude of the hyperfine field 48.2 T of the ferromagnetic state is close to the larger one of the observed fields, 49 T.

Combining all the results obtained in this subsection we conclude that the results of Mössbauer measurements can be explained reasonably if we assume the sample used in the experiment contains two regions, antiferromagnetic NaCl-type FeN and ferromagnetic fcc Fe with the lattice constant a=4.50 Å.

4.2.3 Tetragonal Symmetry

We have performed band calculations also for another kind of antiferromagnetic state specified by $\boldsymbol{q} = [001]$. In this case the magnetic moments on the (001)-plane order ferromagnetically, and the spin direction alternates every other plane in the [001]-direction. Then we can reconstruct the cubic unit cell into the tetragonal one as shown in Fig. 4.7. In order to make comparison on the equal footing we have perform the band calculations also for the non-magnetic and the ferromagnetic state by using the tetragonal cell. The lattice constant was chosen as a=4.50 Å. The calculational results of the total energy, the magnetic moment and the hyperfine field are listed in Table 4.3. In this symmetry the most stable state is the antiferromagnetic one, and the hyperfine field at Fe site is 12.8 and 1.6 T for the antiferromagnetic and the ferromagnetic states, respectively. These values are too small to explain the experimental results. Therefore we can rule out this $\boldsymbol{q} = [001]$ antiferromagnetic state from the candidate for the observed magnetic state of NaCl-type FeN.

Table 4.1: Total energy, magnetic moment and hyperfine field of NaCl-type FeN (upper table) and fcc Fe (lower table) at a=4.50 Å. These results are obtained by using the unit cell of trigonal symmetry.

		non-magnetic state	ferromagnetic state	antiferromagnetic state $\boldsymbol{q} = [111]$
Total Energy [Ryd/FeN]		−2650.8816	−2650.9429	−2650.9433
Magnetic Moment [μ_B/Fe]			3.17	3.34
Hyperfine Field [T] at Fe	core		−41.4	−44.2
	valence		42.7	9.2
	total		1.3	−35.0

Total Energy [Ryd/Fe]		−2541.8375	−2541.9167	−2541.9163
Magnetic Moment [μ_B/Fe]			2.89	3.26
Hyperfine Field [T] at Fe	core		−39.4	−42.2
	valence		−8.8	27.4
	total		−48.2	−14.8

Table 4.2: Hyperfine field and magnetic moment for ferromagnetic and antiferromagnetic states of NaCl-type FeN as a function of lattice constant. Core and valence represent the contribution to the hyperfine field from core and valence electrons, respectively, and total denotes the sum of the two. The unit of hyperfine field is T. These results are obtained by using the unit cell of trigonal symmetry.

a[Å]	ferromagnetic state			
	core	valence	total	m[μ_B/Fe]
3.70	−10.7	19.8	9.1	0.91
3.80	−12.3	20.3	8.0	1.02
3.90	−14.0	20.5	6.5	1.14
4.00	−16.7	21.5	4.8	1.34
4.10	−24.5	29.0	4.5	1.96
4.20	−31.6	35.3	3.6	2.47
4.30	−34.9	37.4	2.5	2.71
4.40	−38.4	40.4	2.1	2.95
4.50	−41.4	42.7	1.3	3.17

a[Å]	antiferromagnetic state			
	core	valence	total	m[μ_B/Fe]
3.70	−9.6	4.6	−5.0	0.77
3.80	−11.5	4.8	−6.7	0.94
3.90	−14.2	5.3	−8.9	1.14
4.00	−17.1	5.7	−11.4	1.34
4.10	−22.1	5.7	−16.4	1.70
4.20	−28.1	5.1	−23.0	2.16
4.30	−35.7	5.6	−30.1	2.75
4.40	−41.4	7.2	−34.2	3.14
4.50	−44.2	9.2	−35.0	3.34

Table 4.3: Total energy, magnetic moment and hyperfine field of NaCl-type FeN (upper table) and fcc Fe (lower table) at a=4.50 Å. These results are obtained by using the unit cell of tetragonal symmetry.

		non-magnetic state	ferromagnetic state	antiferromagnetic state $\boldsymbol{q}$=[001]
Total Energy [Ryd/FeN]		−2650.8601	−2650.9408	−2650.9434
Magnetic Moment [$\mu_{\rm B}$/Fe]			3.22	3.17
Hyperfine Field [T] at Fe	core		−41.3	−40.8
	valence		42.9	28.0
	total		1.6	−12.8

Total Energy [Ryd/Fe]		−2541.8255	−2541.9135	−2541.9039
Magnetic Moment [$\mu_{\rm B}$/Fe]			3.15	3.18
Hyperfine Field [T] at Fe	core		−42.2	−41.9
	valence		6.2	48.7
	total		−36.0	6.8

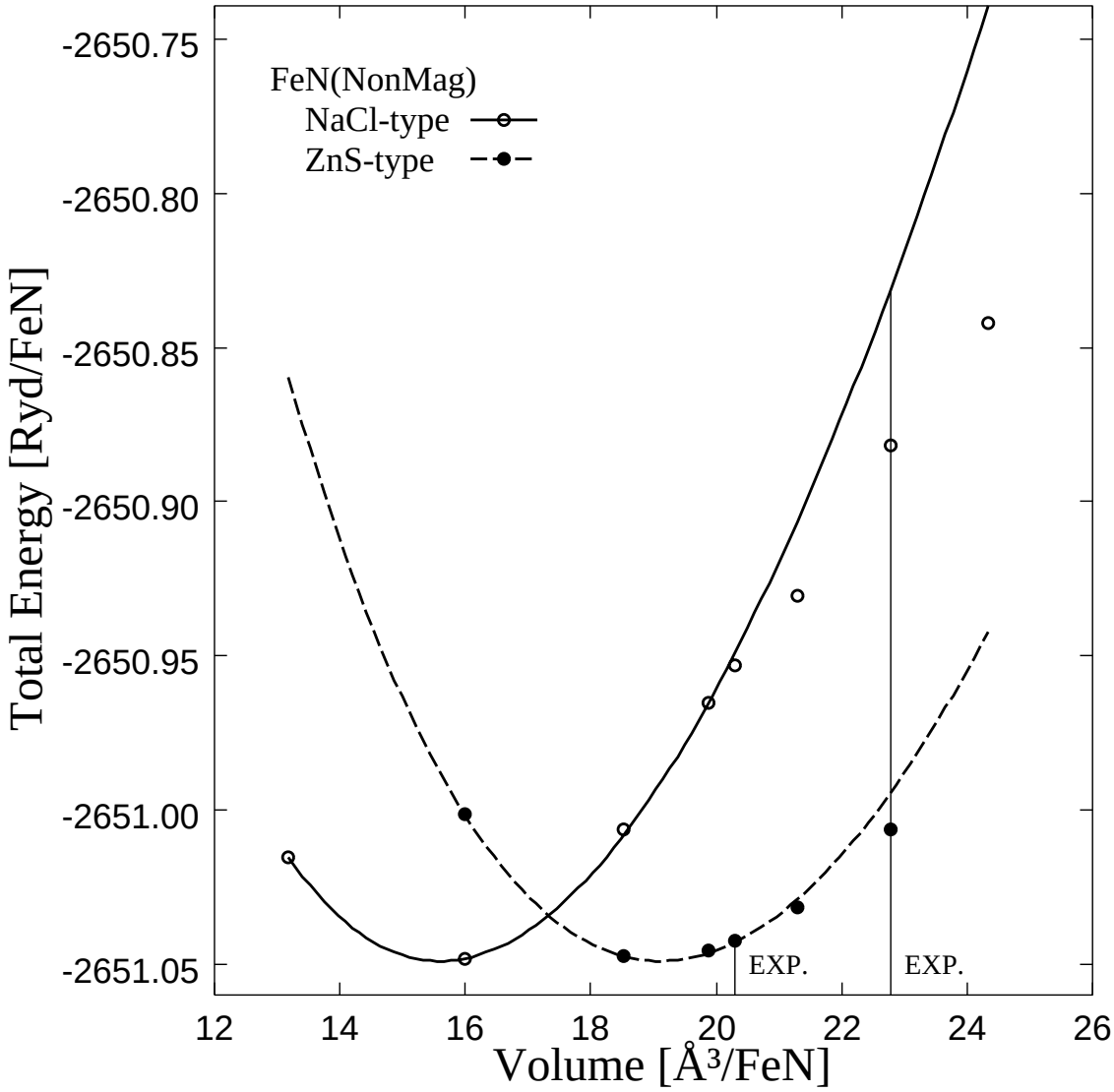

Figure 4.1: Total energy of non-magnetic NaCl-type and ZnS-type FeN as a function of unit cell volume. The solid and dashed lines are result of the fitting by using the Murnaghan's equation (A.4).

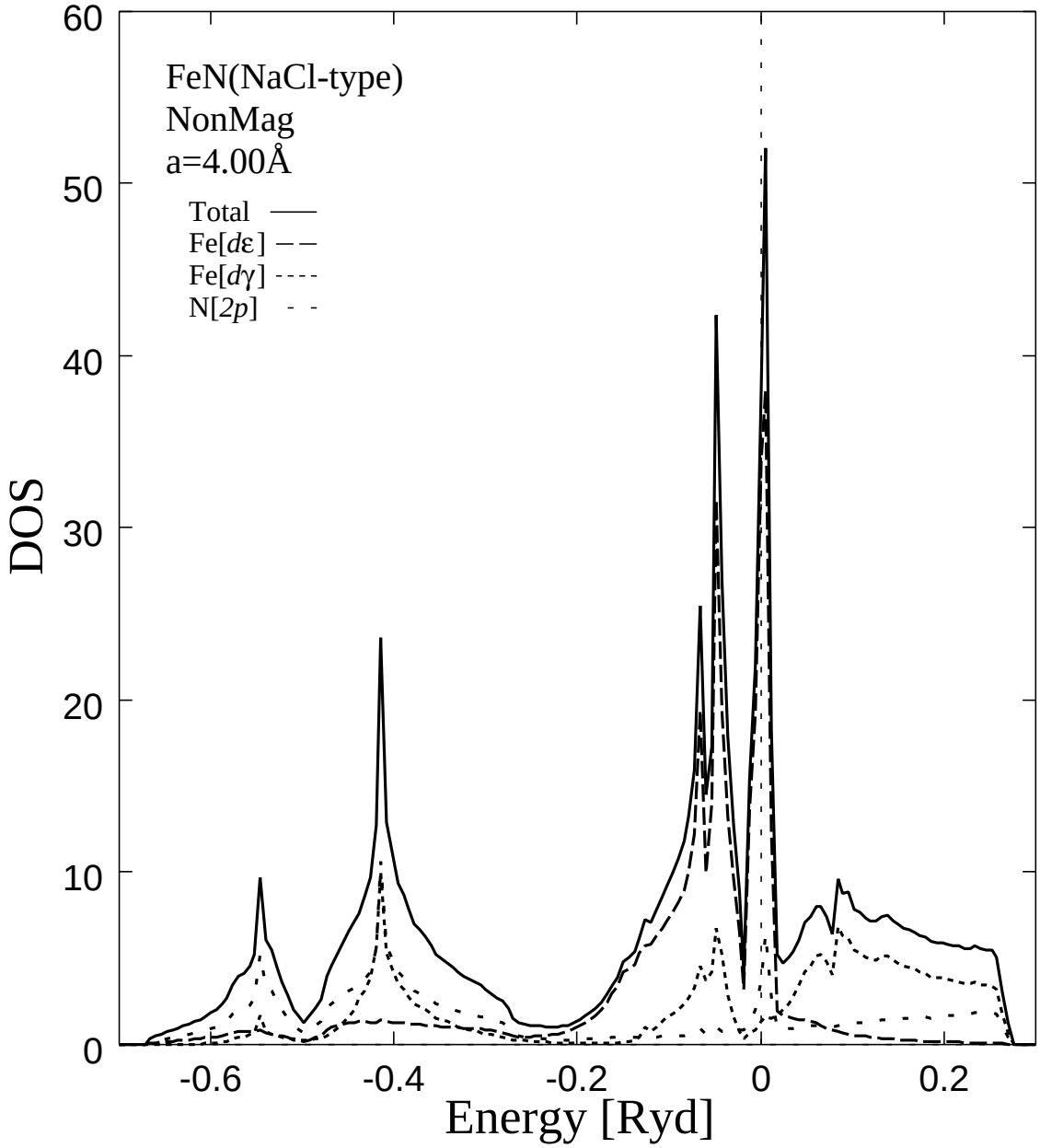

Figure 4.2: DOS for non-magnetic NaCl-type FeN at a=4.00Å. The unit of DOS is states/Ryd per formula unit and per spin.

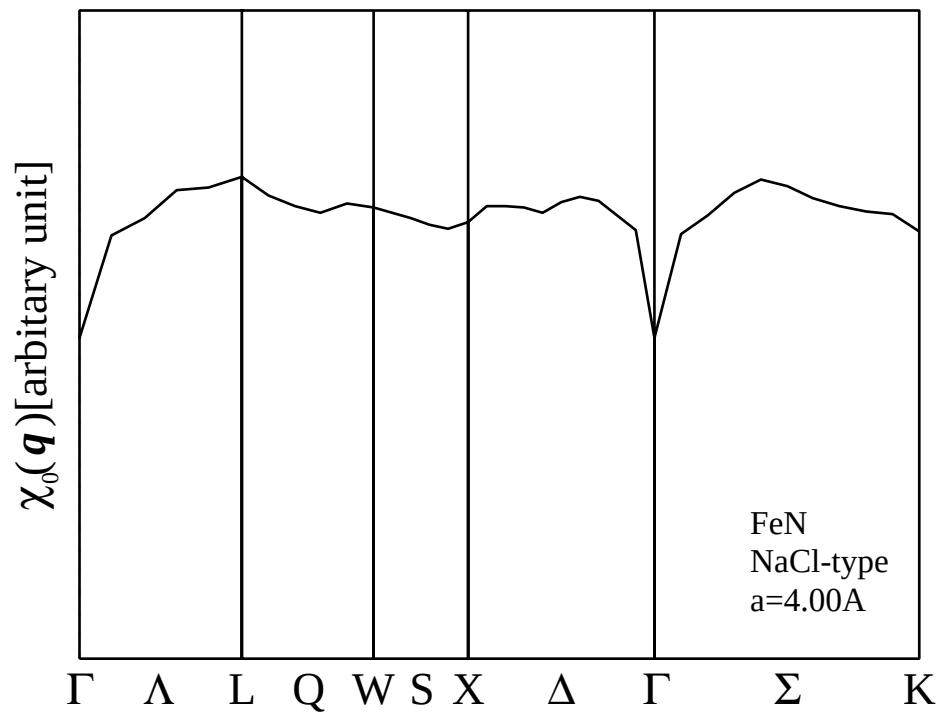

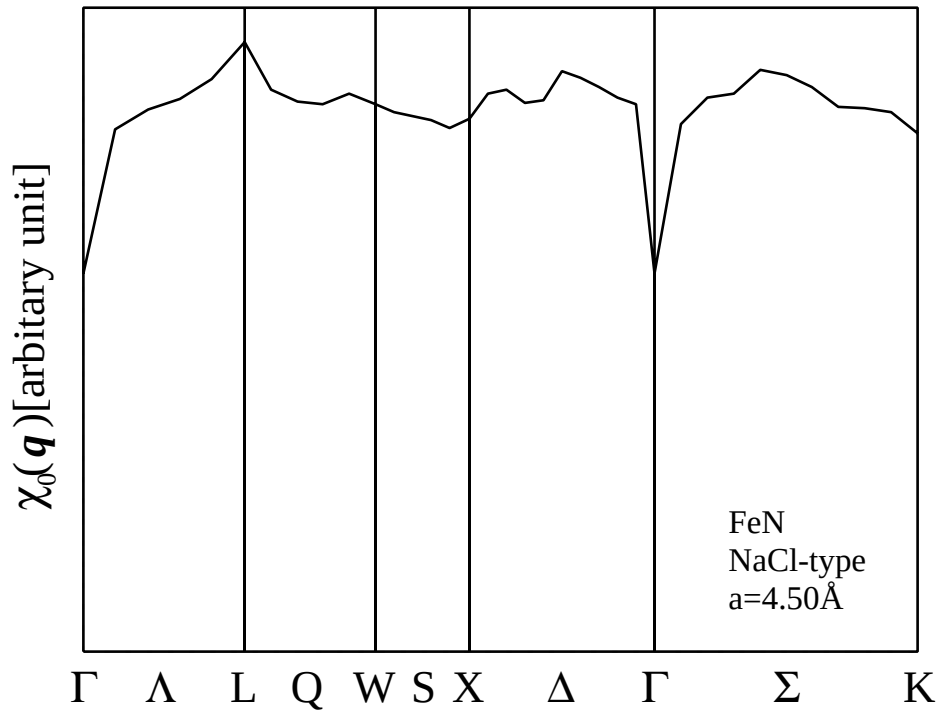

Figure 4.3: $\chi_0(\boldsymbol{q})$ of non-magnetic state of NaCl-type FeN. The unit of $\chi_0(\boldsymbol{q})$ is arbitrary.

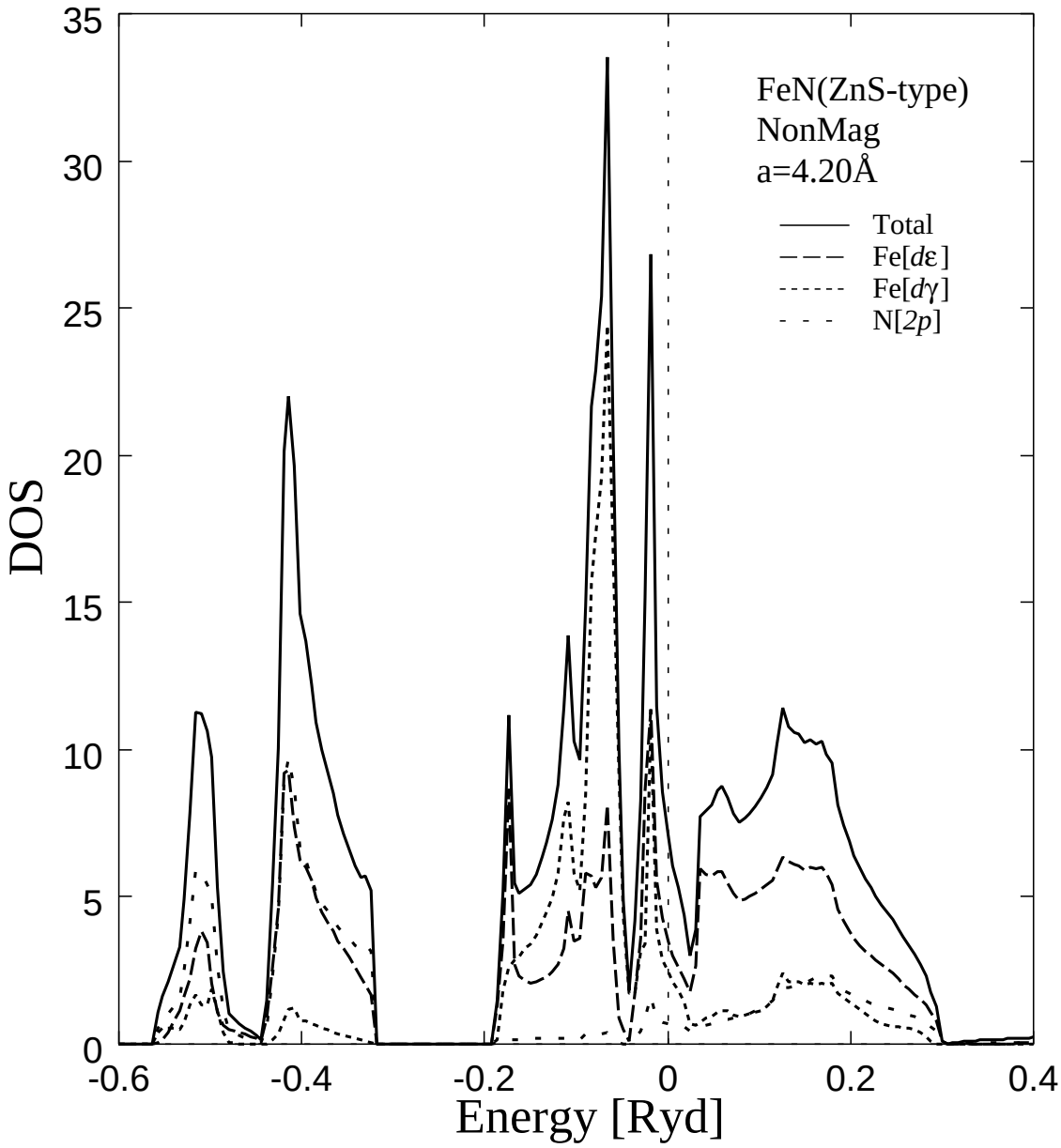

Figure 4.4: DOS for non-magnetic ZnS-type FeN at a=4.20Å. The unit of DOS is states/Ryd per formula unit and per spin.

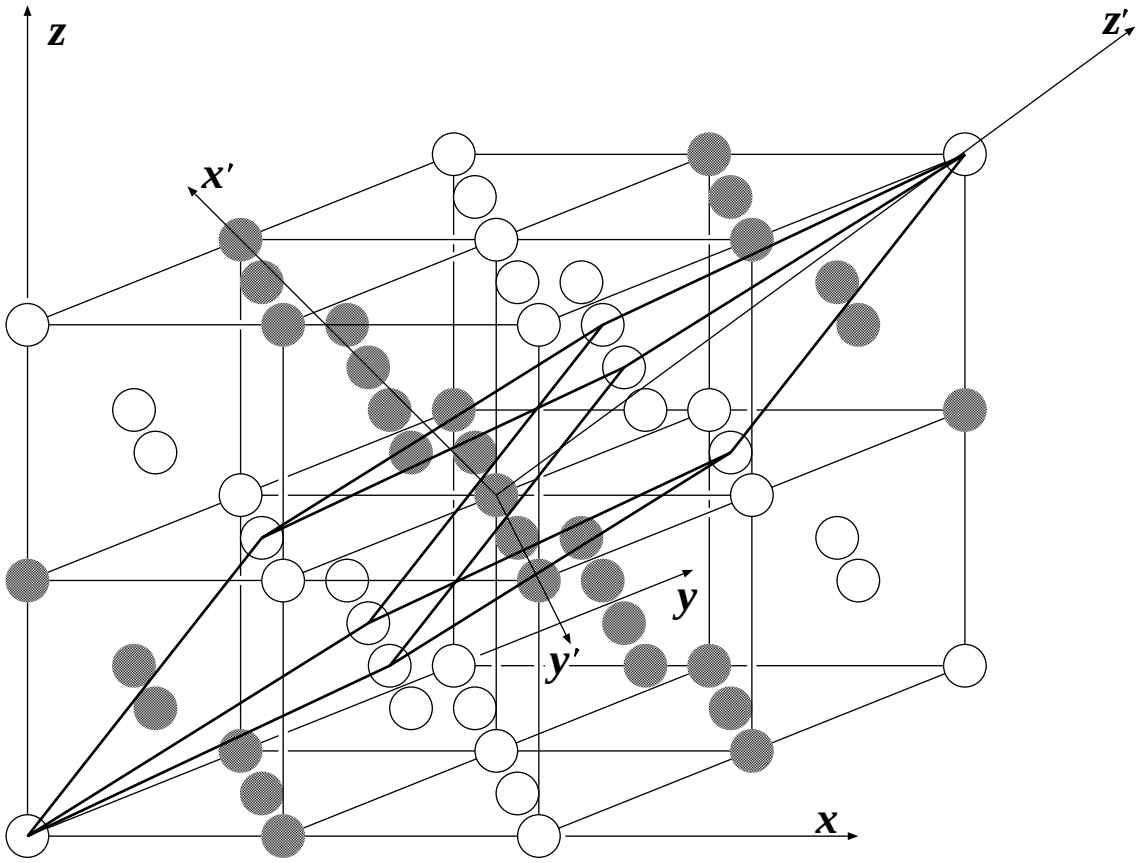

Figure 4.5: Coordinate and unit cell of D_{3d}^5 symmetry ($\boldsymbol{q} = [111]$ antiferromagnetic state). The white and shaded circles are Fe sites which have opposite spin direction each other. If we consider these two Fe sites equivalent, it becomes unit cell of D_{3d}^6 symmetry and this is just the unit cell of non-magnetic and ferromagnetic state.

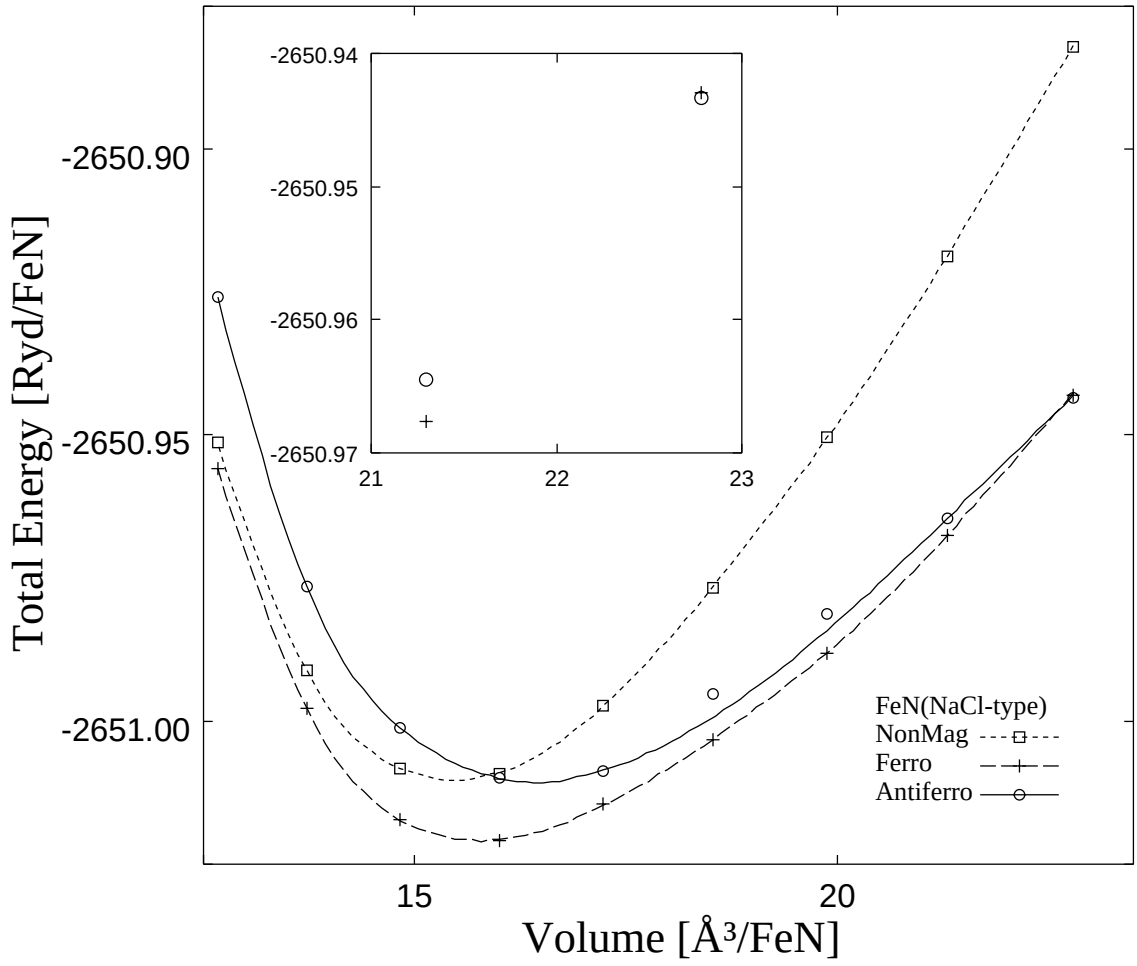

Figure 4.6: Total energy of non-magnetic, ferromagnetic and $\boldsymbol{q} = [111]$ antiferromagnetic states.

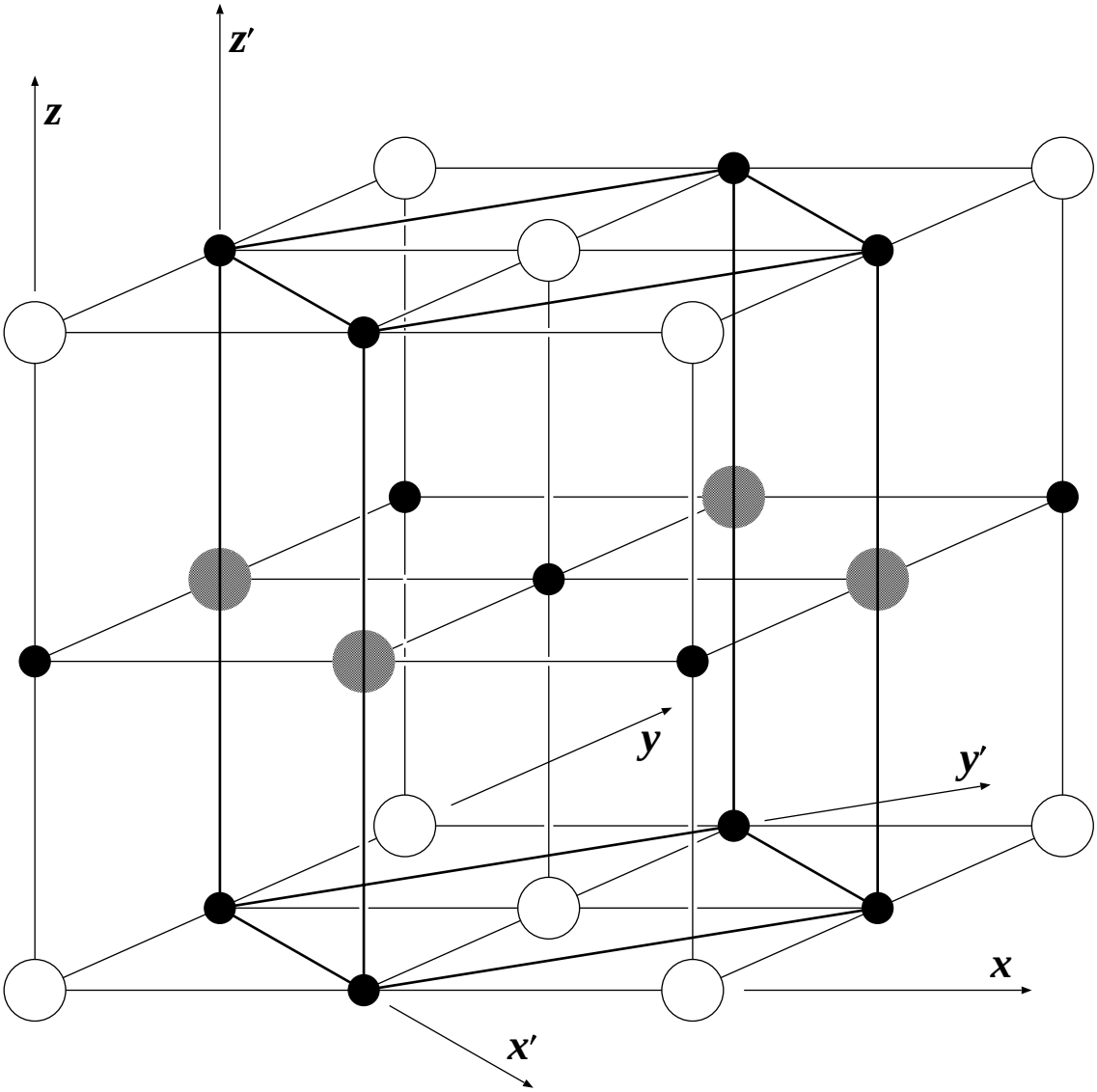

Figure 4.7: Coordinate and unit cell of D^1_{4h} symmetry ($\boldsymbol{q} = [001]$ antiferromagnetic state). The white and shaded circles are Fe sites which have opposite spin direction each other. The black small circle is N atom. If we consider these two Fe sites equivalent, it becomes unit cell of D^{17}_{4h} symmetry and this is just the unit cell of non-magnetic and ferromagnetic state.

Chapter 5

Summary

In this part Ⅱ we have carried out systematic FLAPW band calculations for the whole series of transition-metal mononitrides MN (M=3d transition metal). The main results are summarized as follows.

1. ScN, TiN, VN and CrN

   - The theoretical results for the equilibrium lattice constant of NaCl-type structure are in good agreement with the experimental ones.
   - The bulk moduli calculated for these transition-metal nitrides are larger than that of pure fcc transition metals. This trend is seen also for other transition-metal nitrides.

2. MnN, CoN, NiN and CuN
   Among these four compounds only CoN has been synthesized thus far.

   - The equilibrium lattice constants of the non-magnetic state have been evaluated for both the NaCl-type and the ZnS-type structures. The equilibrium lattice constants of ZnS-type MN are larger by about 0.3Å than those of NaCl-type MN, and for ZnS-type CoN the theoretical value agrees well with the experimental one.
   - Energetically NaCl-type MN is more stable than ZnS-type MN, and magnetic order is expected only for NaCl-type CoN.
   - For NaCl-type CoN we have obtained at least a ferromagnetic solution self-consistently and the energy of the ferromagnetic state is lower than that of the non-magnetic state. It is suggested that if a pure bulk sample

of CoN is synthesized it may have the NaCl-type structure and show some kind of magnetic order.

3. FeN

   - All of the equilibrium lattice constants calculated for the non-magnetic, the ferromagnetic and the $\boldsymbol{q} = [111]$ antiferromagnetic states of NaCl-type FeN are about 4.00 Å, which is much smaller than the observed value, a=4.50 Å.
   - The hyperfine field at Fe site calculated for the equilibrium lattice constant of both the ferromagnetic and the $\boldsymbol{q} = [111]$ antiferromagnetic states cannot explain the hyperfine fields observed by Mössbauer measurements
   - The results of Mössbauer measurements can be explained reasonably if we assume the sample used in the experiment contains two domains, $\boldsymbol{q} = [111]$ antiferromagnetic NaCl-type FeN and ferromagnetic fcc Fe with the lattice constant a=4.50 Å.
   - For ZnS-type FeN, no magnetic order is expected and the equilibrium lattice constant obtained from the band calculation for the non-magnetic state agrees well with the experimental data.

Appendix A

Equilibrium Lattice Constant

In order to estimate the equilibrium lattice constant for a system by FLAPW band calculation, there is one way to compare the total energy as a function of lattice constant. But we cannot calculate the total energy with changing lattice constant continuously, so that we must interpolate the calculated results by some method to estimate the equilibrium lattice constant. The simplest interpolation method is Hooke's Law in which the relation between volume (v) and pressure (p), $\frac{1}{K} = -\frac{1}{v}\left(\frac{\partial v}{\partial p}\right)_T$, is assumed. In this relation, K is a constant. The Hooke's Law, which postulates a linear relation between stress and strain, has a limited range of applicability. Therefore let us assume a linear relation [16]

$$-\frac{1}{v}\frac{dv}{dp} = \frac{1}{c\,(1+kp)}, \tag{A.1}$$

$$c = -\left(v\frac{dp}{dv}\right)_{p=0}, \tag{A.2}$$

$$ck = -\frac{d}{dp}\left(v\frac{dp}{dv}\right). \tag{A.3}$$

The homogeneity of stress has been assumed also, and dependence of temperature, is neglected because it is assumed that temperature is 0K in the band calculation. Equation (A.2) indicates the parameter c denotes isothermal bulk modulus(κ_T). From equation (A.1) and the relation between pressure and energy $p = -\left(\frac{\partial E}{\partial v}\right)_T$, the energy is written as follows:

$$E = \frac{cv}{ck}\left\{\frac{1}{ck-1}\left(\frac{v_0}{v}\right)^{ck} + 1\right\} + const. \tag{A.4}$$

where v_0 is the equilibrium volume at which pressure becomes 0. In practice, the parameters c and ck are determined by fitting the calculated results of energy versus volume to equation (A.4) by a least square method.

We apply this method to paramagnetic state of α-Fe and γ-Fe as a test to evaluate the equilibrium lattice constant and isothermal bulk modulus. The results are shown both in Figs. A.1 and A.2 and also in Table A.1. The obtained equilibrium lattice constant cannot reproduce quite well the experimental data, and this is considered to be due to the use of LDA. If we compare our lattice constant with the results of other calculations [22],[23], fairly good agreement can be seen. On the other hand, the bulk modulus does not agree with that of other calculation [22]. It might be due to different band calculational method and different fitting method. Seeing Fig. A.2, the fitting is not good in the range that the system is extended (right hand side of the figure). Therefore this method can be used well near the equilibrium state, but should not be applied to the range far from the equilibrium state.

Table A.1: The calculated equilibrium lattice constants and bulk moduli of α-Fe and γ-Fe.

	a_0[Å]		κ_T[Mbar]		other's calc.[24]	
	Calc.	Exp.	Calc.	Exp.	a_0	κ_T
α-Fe	2.73	2.86	2.37	1.7	2.75	2.8
γ-Fe	3.40		2.86		3.45	2.6

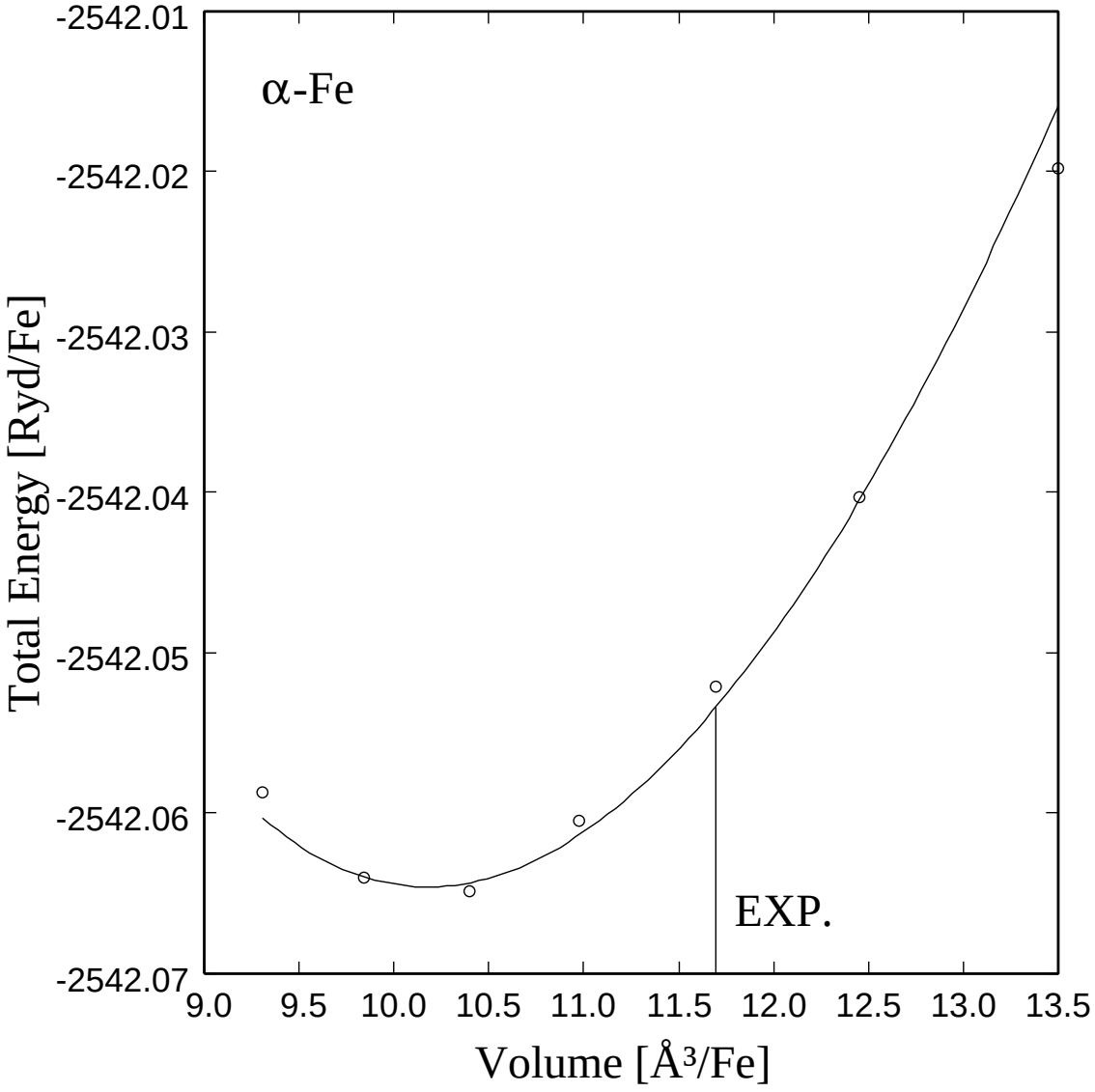

Figure A.1: Total energy versus volume for α-Fe. The circles denote calculated point. The solid line is fitting line.

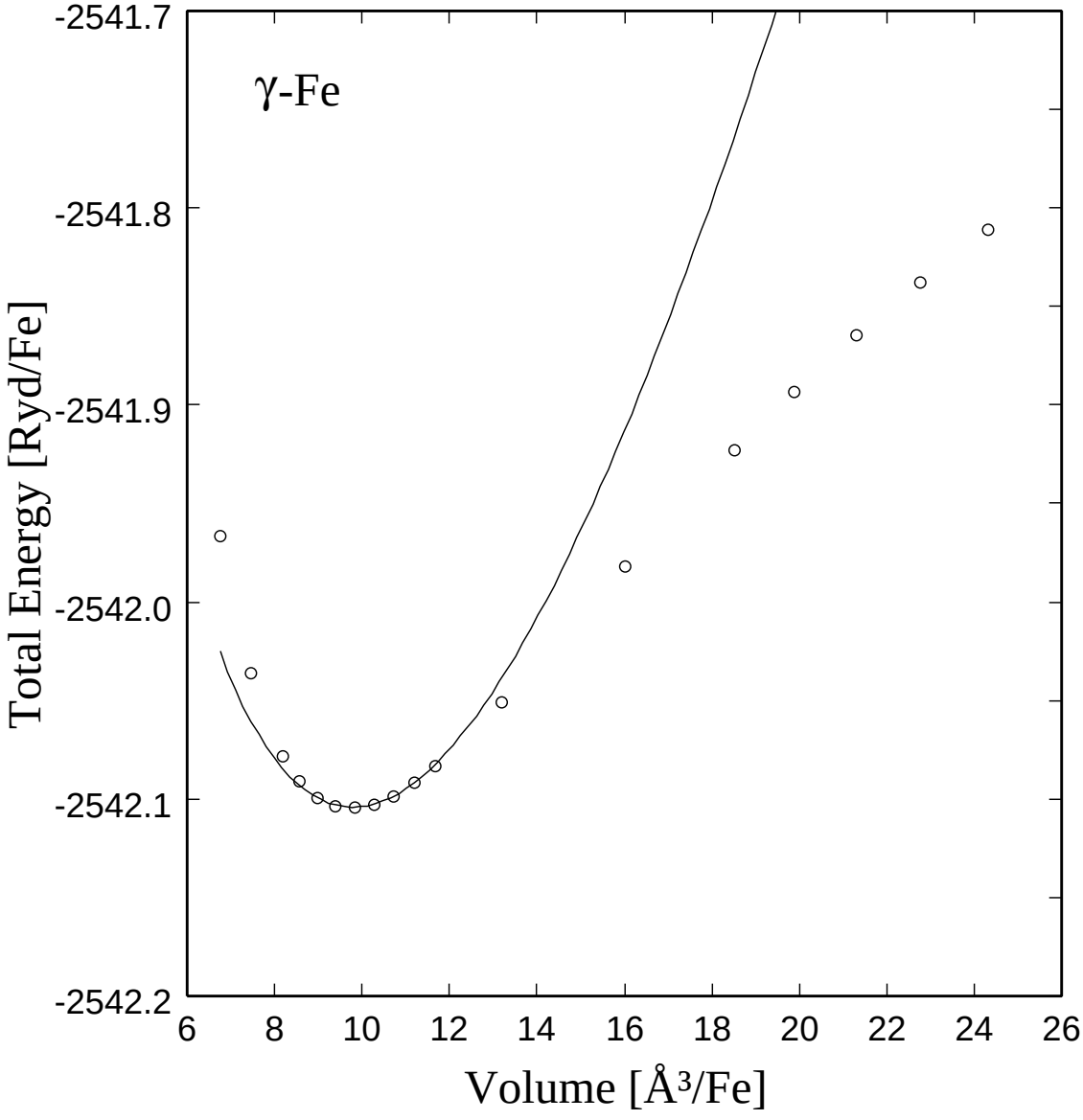

Figure A.2: Total energy versus volume for γ-Fe. The circles denote calculated point. The solid line is fitting line.

Appendix B

Mössbauer effect

B.1 Principle of the Mössbauer Effect

B.1.1 Nuclear γ-ray Resonance

Mössbauer spectroscopy measurement utilizes a transition of nuclear state, mostly between a ground and an excited state, to get information of an atom. The difference of energy level between a ground and an excited state is an individual character of atom. When a nucleus is in an excited state, that nucleus decays to a ground state with radiating γ-ray. This radiated γ-ray can afford to transfer another nucleus to the excited state. The energy of this γ-ray is so high that the atom receives a recoil when it is radiated or absorbed. This recoil energy is obtained as following way. Conservation of energy and momentum can be written as follows.

$$E = E_\gamma + E_R \tag{B.1}$$

$$0 = p_\gamma + Mv \tag{B.2}$$

where E, E_γ and E_R are difference of energy between the ground state and the excited state, energy of γ-ray and recoil energy, respectively. And p_γ, M, v are momentum of γ-ray, mass of nucleus and velocity of nucleus, respectively. The energy of γ-ray and recoil energy are expressed as

$$E_\gamma = c\,p_\gamma, \tag{B.3}$$

$$E_R = \frac{1}{2}Mv^2. \tag{B.4}$$

where c is light velocity. From the momentum conservation, the velocity of nucleus(v) is expressed as

$$v = -\frac{p_\gamma}{M} \tag{B.5}$$

$$= -\frac{1}{M}\frac{E_\gamma}{c}. \tag{B.6}$$

Substituting equation (B.6) into (B.4)

$$E_R = \frac{1}{2M}\left(\frac{E_\gamma}{c}\right)^2. \tag{B.7}$$

Suppose $E \sim E_\gamma$,

$$E_R \simeq \frac{1}{2M}\left(\frac{E}{c}\right)^2. \tag{B.8}$$

The energy gain of absorber is smaller than E about by amount of $2E_R$. So that the probability of such transition (occurrence of resonance) is very small.

B.1.2 Recoilless Nuclear γ-ray Resonance

In a solid all atoms are loosely bound to their surrounded atoms, so that any atom can't move freely. Roughly the recoil energy is received by a whole solid in the process of γ-ray emission or absorption. This means that the nuclear mass which appears in the equation (B.8) is replaced by the macroscopic mass of solid. Then the recoil energy is effectively zero. This is an oversimplification of the phenomenon. The crystal lattice possesses vibrational degrees of freedom, phonon, which expresses the displacement of atoms. If the recoil energy is enough to excite a phonon, the energy of γ-ray is reduced by amount of the excitation energy of the phonon. In such a case nuclear γ-ray resonance can't occur. But there is some probability that no phonon is excited in these γ-ray processes. Such a recoilless process is called Mössbauer effect and is important in the Mössbauer effect measurement. We think about the case that a nucleus receives recoil energy E_R. Furthermore we think that the probability of the occurrence for no phonon excited process is f(f is called recoilless fraction), and we restrict the transition of phonon state to the state which energy is higher than initial state by amount of $h\nu$. Then from the conservation of the energy,

$$E_R = (1-f)h\nu. \tag{B.9}$$

And the recoilless fraction becomes

$$f = 1 - \frac{E_R}{h\nu}. \tag{B.10}$$

It is necessary for the Mössbauer spectroscopy measurement that this f is not zero.

B.2 Mössbauer Spectrum

In the Mössbauer spectroscopy measurement, γ-decay of nucleus is used. For example, ^{57}Fe is very convenient for the investigation of the magnetism of the intermetallic compound of Fe. The energy level of this nucleus is shown in Fig. B.2. ^{57}Co which is unstable radio-isotope of ^{59}Co decays to ^{57}Fe which nuclear angular momentum is $I = \frac{5}{2}$. When this ^{57}Fe decays, its nuclear angular momentum decreases to $I = \frac{3}{2}$ and γ-ray is radiated. After that ^{57}Fe decays to the state which nuclear angular momentum $I = \frac{1}{2}$. Mössbauer spectroscopy measurement utilizes the γ-ray which is just radiated form the last process. The condition which must be satisfied by the energy level of ground state and excited state of source and absorber is

$$(E_e)_S - (E_g)_S = (E_e)_A - (E_g)_A, \tag{B.11}$$

where subscript e and g denotes the excited state and ground state, respectively, and S and A denotes the source and absorber, respectively. However the local environment around nucleus is different between source and absorber, so that the energy level is slightly different. This is why that there is a shift of peek position and there are a lot of peeks in a Mössbauer spectrum. If we know about the nucleus in the source, we can get information about nucleus in the absorber. And indirectly we can get information about electrons surrounding the nucleus.

Electrons which surround nucleus make both electric and magnetic field at the nucleus. These two fields cause a lot of changes in the nuclear state (Figure B.1). Mössbauer effect measurement is intended to get information about nucleus state in a solid. The other way we can get information about electrons, charge and spin density, indirectly from the nuclear state.

B.2.1 Interaction with Electric Field

A nucleus is surrounded by a lot of electrons which make electric field at the nucleus. The interaction between the electron and the nucleus is carried by the Coulomb interaction between the electron charge and the nucleus (proton) charge. We start to consider this interaction classically,

$$\mathcal{H}_{int} = \int \rho_n(\boldsymbol{R}) V(\boldsymbol{R}) d\boldsymbol{R}\,, \tag{B.12}$$

where $\rho_n(\boldsymbol{R})$ is the charge distribution of nucleus. The definition of $V(\boldsymbol{R})$ is written using the electron charge distribution $\rho_e(\boldsymbol{r})$ as

$$V(\boldsymbol{R}) = \int \frac{\rho_e(\boldsymbol{r})}{|\boldsymbol{r}-\boldsymbol{R}|} d\boldsymbol{r}. \tag{B.13}$$

The protons are located fairly close to $\boldsymbol{R} \sim 0$ so that we neglect the contribution of electric field from the electron inside $|\boldsymbol{r}| < |\boldsymbol{R}|$ and expand the $V(\boldsymbol{R})$ around $\boldsymbol{R} = 0$,

$$V(\boldsymbol{R}) = V(0) + \sum_i \left(\frac{\partial V}{\partial x_i}\right)_{\boldsymbol{R}=0} X_i + \frac{1}{2!}\sum_{i,j}\left(\frac{\partial^2 V}{\partial x_i \partial x_j}\right)_{\boldsymbol{R}=0} X_i X_j + \cdots, \tag{B.14}$$

i, j denote x, y or z. If we neglect the terms which are more than third order differential term,

$$\begin{aligned}
\mathcal{H} &\simeq \int \rho_n(\boldsymbol{R}) \left\{ V(0) + \sum_i \left(\frac{\partial V}{\partial x_i}\right)_{\boldsymbol{R}=0} X_i + \frac{1}{2}\sum_{i,j}\left(\frac{\partial^2 V}{\partial x_i \partial x_j}\right)_{\boldsymbol{R}=0} X_i X_j \right\} d\boldsymbol{R} \\
&= V(0)\int \rho_n(\boldsymbol{R}) d\boldsymbol{R} + \sum_i \left(\frac{\partial V}{\partial x_i}\right)_{\boldsymbol{R}=0} \int \rho_n(\boldsymbol{R}) X_i d\boldsymbol{R} \\
&+ \frac{1}{2}\sum_{i,j}\left(\frac{\partial^2 V}{\partial x_i \partial x_j}\right)_{\boldsymbol{R}=0} \int \rho_n(\boldsymbol{R}) X_i X_j d\boldsymbol{R}.
\end{aligned} \tag{B.15}$$

The first term of the equation (B.14) is the Coulomb interaction between electron and proton which is assumed to be located at $\boldsymbol{R} = 0$. The second term vanishes if we assume the parity of $\rho_n(\boldsymbol{R})$ is even. The third term is written as

$$\mathcal{H}_2 = \frac{1}{6}\sum_i V_{ii} \int \rho_n(\boldsymbol{R}) R^2 d\boldsymbol{R} + \frac{1}{6}\sum_{i,j} V_{ij} \int \rho_n(\boldsymbol{R}) \left(3X_i X_j - \delta_{ij} R^2\right) d\boldsymbol{R}, \tag{B.16}$$

$$\begin{aligned}
V_{ij} &= \left(\frac{\partial^2 V}{\partial x_i \partial x_j}\right)_{\boldsymbol{R}=0}, \\
R^2 &= X^2 + Y^2 + Z^2
\end{aligned}$$

The first term of the equation (B.16) expresses the energy shift caused by the spherically distributed protons' charge, and the second one is the energy shift caused by the asphericity of the protons' charge distribution. Each term of the equation

(B.16) is called electric monopole interaction and electric quadrupole interaction, respectively. From the Poisson's relation

$$\frac{\partial^2 V}{\partial x^2} + \frac{\partial^2 V}{\partial y^2} + \frac{\partial^2 V}{\partial z^2} = -4\pi\rho(\boldsymbol{r}), \tag{B.17}$$

we can rewrite the electric monopole interaction as follow,

$$\begin{aligned} \mathcal{H}_{mono} &= \frac{1}{6}\sum_i V_{ii} \int \rho_n(\boldsymbol{R}) R^2 d\boldsymbol{R} \\ &= -\frac{4\pi}{6}\rho_e(0) \int \rho_n(\boldsymbol{R}) R^2 d\boldsymbol{R} \end{aligned} \tag{B.18}$$

Furthermore if we assume that the protons' charge distribution is uniform in a sphere which radius is R,

$$\rho_n = \frac{Ze}{\frac{4}{3}\pi R^3} \tag{B.19}$$

where Z is the atomic number. Substituting the equation (B.19) into $\mathcal{H}_{mono}$

$$\mathcal{H}_{mono} = -\frac{4\pi}{6}\rho_e(0)\frac{3Ze}{4\pi R^3}\int_0^R R^2 d\boldsymbol{R} \tag{B.20}$$

$$= -\frac{4\pi}{6}\rho_e(0)\frac{3Ze}{4\pi R^3}\frac{4\pi}{5}R^5 \tag{B.21}$$

$$= -\frac{2Ze}{5}\pi\rho_e(0)R^2 \tag{B.22}$$

$$= \frac{2Ze^2}{5}\pi \left|\psi(0)\right|^2 R^2 \tag{B.23}$$

In the last equation we consider that the electron density is well approximated by $-e\left|\psi(0)\right|^2$. This $\mathcal{H}_{mono}$ will be different for two nuclei of the same charge but different charge distribution (isotopes), or for two nuclei of the same mass and charge but different nuclear states (isomers). So that Mössbauer spectrum has a peek at the position which is shifted by amount of δ which becomes

$$\delta = \frac{2Ze^2}{5}\pi\left(R_e^2 - R_g^2\right)\left(\left|\psi(0)_A^2\right| - \left|\psi(0)_S^2\right|\right). \tag{B.24}$$

This δ is called *isomer shift*.

Next we consider about the electric quadrupole interaction($\mathcal{H}_{quad}$).

$$\mathcal{H}_{quad} = \frac{1}{6}\sum_{i,j} V_{ij}Q_{ij} \tag{B.25}$$

where

$$V_{ij} = \left(\frac{\partial^2 V}{\partial x_i \partial x_j}\right)_{\boldsymbol{R}=0} = \int \rho_e(\boldsymbol{r})\frac{3r_i r_j - \delta_{ij}r^2}{r^5}d\boldsymbol{r}\,, \tag{B.26}$$

$$Q_{ij} = \int \rho_n(\boldsymbol{R})\left(3X_iX_j - \delta_{ij}R^2\right)d\boldsymbol{R}\,. \tag{B.27}$$

To obtain a quantum mechanical expression for the quadrupole interaction, we replace the classical $\rho_n(\boldsymbol{R})$ by its quantum mechanical operator $\hat{\rho}(\boldsymbol{R})$,

$$\rho_n(\boldsymbol{R}) \rightarrow \hat{\rho}(\boldsymbol{R}) = e \sum_p \delta(\boldsymbol{R} - \boldsymbol{R}_p) \tag{B.28}$$

Substituting the equation (B.28) into the classical definition of Q_{ij} (B.27), we obtain the quadrupole operator $\hat{Q}_{ij}$

$$\begin{aligned} \hat{Q}_{ij} &= e \sum_p \int \delta(\boldsymbol{R} - \boldsymbol{R}_p) \left(3X_i X_j - \delta_{ij} R^2\right) d\boldsymbol{R} \\ &= e \sum_p \left(3X_{pi} X_{pj} - \delta_{ij} R_p^2\right) \end{aligned} \tag{B.29}$$

Then we have a quadrupole term in a quantum mechanical form. In the Mössbauer spectroscopy measurement, in general, we are concerned only with the ground state of a nucleus or with the exited state which has sufficiently long life-time. Therefore a nuclear state can be specified by the total angular momentum ($\boldsymbol{I}$) of each state, a component of the angular momentum (I_z) and a set of other quantum numbers (η). The matrix elements of $\hat{Q}_{ij}$ which has non zero value are

$$\langle I, I_z, \eta \,|\hat{Q}_{ij}|\, I, I_z', \eta \rangle. \tag{B.30}$$

Now we introduce the irreducible tensor operator T_{2m} The definition of T_{2m} is listed in Table B.1. Then $\hat{Q}_{ii}$ can be expressed by a linear combination of T_{2m}.

$$\hat{Q}_{ij} = \sum_m \alpha_{ij,m} T_{2m}(\boldsymbol{r}). \tag{B.31}$$

And using the coefficients $\alpha_{ij,m}$, we could define new tensor as

$$\hat{Q}'_{ij} = \sum_m \alpha_{ij,m} T_{2m}(\boldsymbol{I}). \tag{B.32}$$

Applying the Wigner-Eckart's Theorem, we can make a relation between $\hat{Q}_{ij}$ and $\hat{Q}'_{ij}$.

$$\langle I, I_z, \eta \,|\hat{Q}_{ij}|\, I, I_z', \eta \rangle = C \langle I, I_z, \eta \,|\hat{Q}'_{ij}|\, I, I_z', \eta \rangle \tag{B.33}$$

where C is a constant which depends on I and η but same for all I_z,I_z',i and j. We can express C by the matrix element for which $I_z = I_z' = I$ and $X_{pi} = X_{pj} = Z_p$ as follow

$$\begin{aligned} \langle I, I, \eta \,| e \sum_p \left(3Z_p^2 - R_p^2\right) |\, I, I, \eta \rangle &= C \langle I, I, \eta \,| \left(3I_z^2 - \boldsymbol{I}^2\right) |\, I, I, \eta \rangle \\ &= CI(2I-1) \end{aligned} \tag{B.34}$$

In evaluating the right-hand side of the equation (B.34), we assume the quantum number η can commute with $\boldsymbol{I}^2$ and I_z. Using the equation (B.34), we define a symbol eQ as

$$eQ \equiv \langle I, I, \eta \,|\, e \sum_p \left(3Z_p^2 - R_p^2 \right) \,|\, I, I, \eta \rangle \tag{B.35}$$

Q is called the *quadrupole moment* of a nucleus. We can express the C in the equation (B.34) as

$$C = \frac{eQ}{I(2I-1)}. \tag{B.36}$$

Reconstructing the nuclear quadrupole operator by the nuclear angular momentum operator and taking the axes to a set of principal axes relative to which $V_{ij} = 0$ for $i \neq j$. Then the quadrupole Hamiltonian becomes

$$\mathcal{H}_{quad} = \frac{eQ}{6I(2I-1)} \left\{ V_{xx} \left(3I_x^2 - \boldsymbol{I}^2 \right) + V_{yy} \left(3I_y^2 - \boldsymbol{I}^2 \right) + V_{zz} \left(3I_z^2 - \boldsymbol{I}^2 \right) \right\}. \tag{B.37}$$

This interaction causes an appearance of a lot of peeks in a Mössbauer spectrum and sometimes causes asymmetry in a Mössbauer spectrum. Electrons surrounding a nucleus are divided into two parts, closed shell and open shell. The electric quadrupole interaction might occur from only open shell, because it is considered that a electron which belongs to a closed shell distributes spherically which does not give any contribution to field gradient. But aspherical distribution of open shell electron causes distortion of the electron distribution of closed shell. This effect is called Sternheimer antishielding. It makes difficult to estimate the quadrupole interaction.

B.2.2 Interaction with Magnetic Field

A nucleus has a magnetic moment ($\boldsymbol{m}_n$) which is defined as

$$\boldsymbol{m}_n = \gamma_n \hbar \boldsymbol{I}, \tag{B.38}$$

where γ_n is gyromagnetic ratio of nucleus and $\boldsymbol{I}$ is an angular momentum operator of a nucleus. This magnetic moment makes a vector potential ($\boldsymbol{A}$). Under the condition $\nabla \cdot \boldsymbol{A} = 0$, the vector potential is written as

$$\boldsymbol{A} = \frac{\boldsymbol{m}_n \times \boldsymbol{r}}{r^3} = \nabla \times \left(\frac{\boldsymbol{m}_n}{r} \right). \tag{B.39}$$

In this field, Schrödinger equation for one electron becomes

$$\begin{aligned} \mathcal{H} &= \frac{1}{2m} \left(\boldsymbol{p} + \frac{e}{c} \boldsymbol{A} \right)^2 + \gamma_e \hbar \boldsymbol{\sigma} \cdot \nabla \times \boldsymbol{A} + V(\boldsymbol{r}) \\ &\simeq \frac{\boldsymbol{p}^2}{2m} + V(\boldsymbol{r}) + \frac{e\hbar}{mc} \boldsymbol{m}_n \cdot \boldsymbol{l} + \gamma_e \boldsymbol{\sigma} \cdot \nabla \times \boldsymbol{A} \end{aligned} \tag{B.40}$$

where γ_e is gyromagnetic ratio of electron, $\boldsymbol{\sigma}$ is the electron spin operator and $\boldsymbol{l}$ is the angular momentum of a electron. In the last equation we neglect the term which is proportional to $\boldsymbol{A}^2$. The last term expresses the interaction between the magnetic field of nucleus and electron spin. From now on we concentrate on this interaction ($\mathcal{H}_{mag}$)

$$\mathcal{H}_{mag} = \frac{e\hbar}{mc}\boldsymbol{m}_n \cdot \boldsymbol{l} + \gamma_e \hbar \boldsymbol{\sigma} \cdot \nabla \times \boldsymbol{A} \tag{B.41}$$

Using the relations

$$\nabla \times \nabla \times \boldsymbol{A} = \nabla(\nabla \cdot \boldsymbol{A}) - \nabla^2 \boldsymbol{A}, \tag{B.42}$$

$$\nabla^2 \left(\frac{1}{r}\right) = -4\pi\delta(\boldsymbol{r}) \tag{B.43}$$

$\mathcal{H}_{mag}$ becomes

$$\begin{aligned}\mathcal{H}_{mag} &= \frac{8\pi}{3}\gamma_e\gamma_n\hbar^2\boldsymbol{\sigma}\cdot\boldsymbol{I}\delta(\boldsymbol{r}) - \gamma_e\gamma_n\hbar^2\boldsymbol{I}\cdot\left\{\frac{\boldsymbol{\sigma}}{r^3} - 3\frac{\boldsymbol{r}(\boldsymbol{\sigma}\cdot\boldsymbol{r})}{r^5}\right\} + \gamma_e\gamma_n\hbar^2\frac{\boldsymbol{I}\cdot\boldsymbol{l}}{r^3}. \\ &= -\gamma_n\hbar\boldsymbol{I}\cdot\boldsymbol{H}_{loc}. \end{aligned} \tag{B.44}$$

$\boldsymbol{H}_{loc}$ is called *hyperfine field*, and the definition is

$$\boldsymbol{H}_{loc} = -\frac{8\pi}{3}\gamma_e\hbar\delta(\boldsymbol{r})\boldsymbol{\sigma} + \gamma_e\hbar\frac{r^2\boldsymbol{\sigma} - 3(\boldsymbol{\sigma}\cdot\boldsymbol{r})\boldsymbol{r}}{r^5} - \gamma_e\hbar\frac{\boldsymbol{l}}{r^3} \tag{B.45}$$

$\boldsymbol{H}_{loc}$ is the effective field for nuclear angular momentum created by electron spin. The meaning of each terms are written below. The first term is Fermi contact term which denotes the magnetic field that electron creates at the nuclear position. The second term is classical dipole-dipole interaction. And the last term represents the interaction between the nucleus magnetic moment and electron current. In general the Fermi contact term is considered to contribute most to the hyperfine field therefore we neglect other two terms. Then $\mathcal{H}_{mag}$ is approximately

$$\mathcal{H}_{mag} \sim \frac{8\pi}{3}\gamma_e\gamma_n\hbar^2\boldsymbol{I}\cdot\boldsymbol{\sigma}\delta(\boldsymbol{r}). \tag{B.46}$$

We can see from the equation (B.46) that only s-orbital electron which has a finite probability at the nuclear site make a contribution to the Fermi contact term. Then the hyperfine field which is created by the Fermi contact becomes

$$H_{loc} = -\frac{8\pi}{3}\gamma_e\hbar\left(|\psi_{s\downarrow}(0)|^2 - |\psi_{s\uparrow}(0)|^2\right). \tag{B.47}$$

The degeneracy of nuclear states which has a same quantum number I but different in a quantum number I_z is decomposed. Therefore a lot of peeks could appear in a Mössbauer spectrum.

Table B.1: Irreducible tensor operator (T_{2m} (m=-2,-1,0,1,2)). x, y and z are operators of coordinate, and I_z, $I^+ \equiv I_x + iI_y$ and $I^- \equiv I_x - iI_y$ are operators of total angular momentum of a nucleus.

	$T_{2m}(\boldsymbol{r})$	$T_{2m}(\boldsymbol{I})$
T_{22}	$(x+iy)^2$	I^{+2}
T_{21}	$-2z(x+iy)$	$-(I_zI^+ + I^+I_z)$
T_{20}	$\sqrt{\frac{2}{3}}(3z^2 - r^2)$	$\sqrt{\frac{2}{3}}(3I_z^2 - I^2)$
T_{2-1}	$2z(x-iy)$	$I_zI^- + I^-I_z$
T_{2-2}	$(x-iy)^2$	I^{-2}

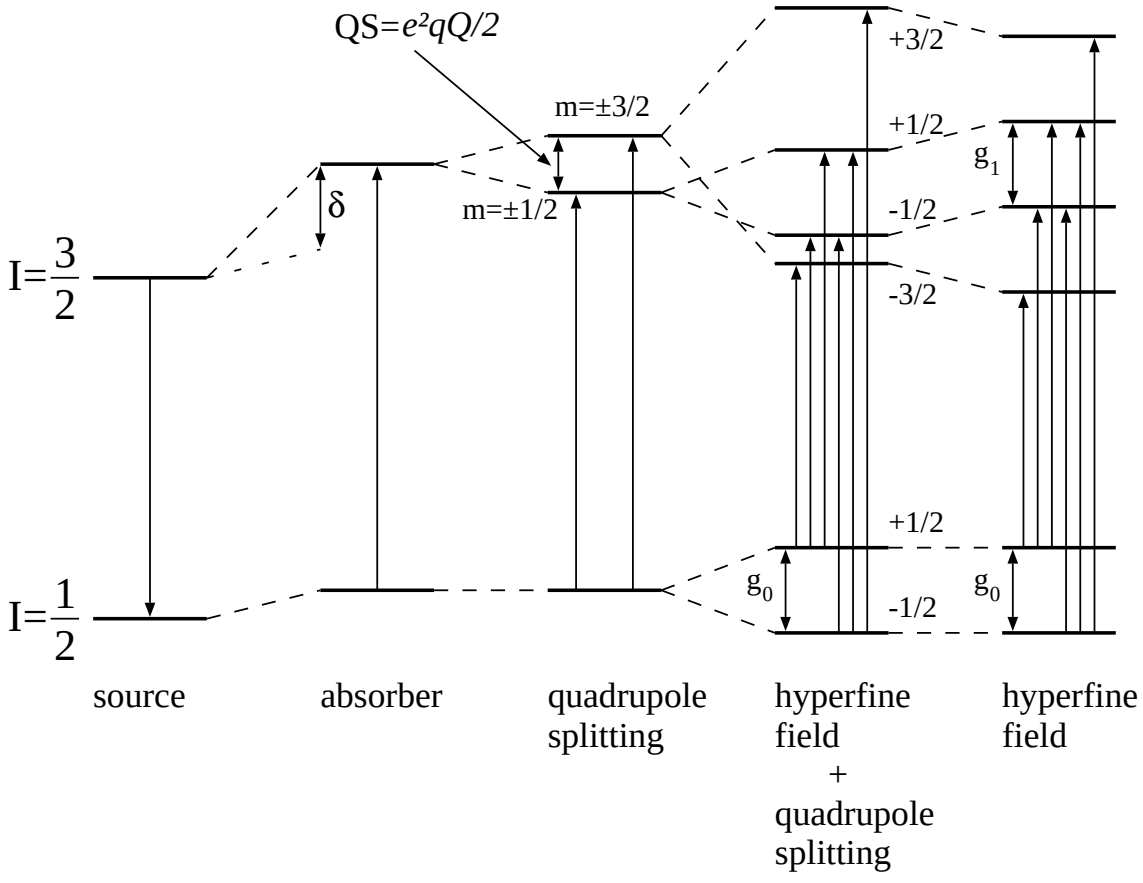

Figure B.1: Energy level shift of ^{57}Fe

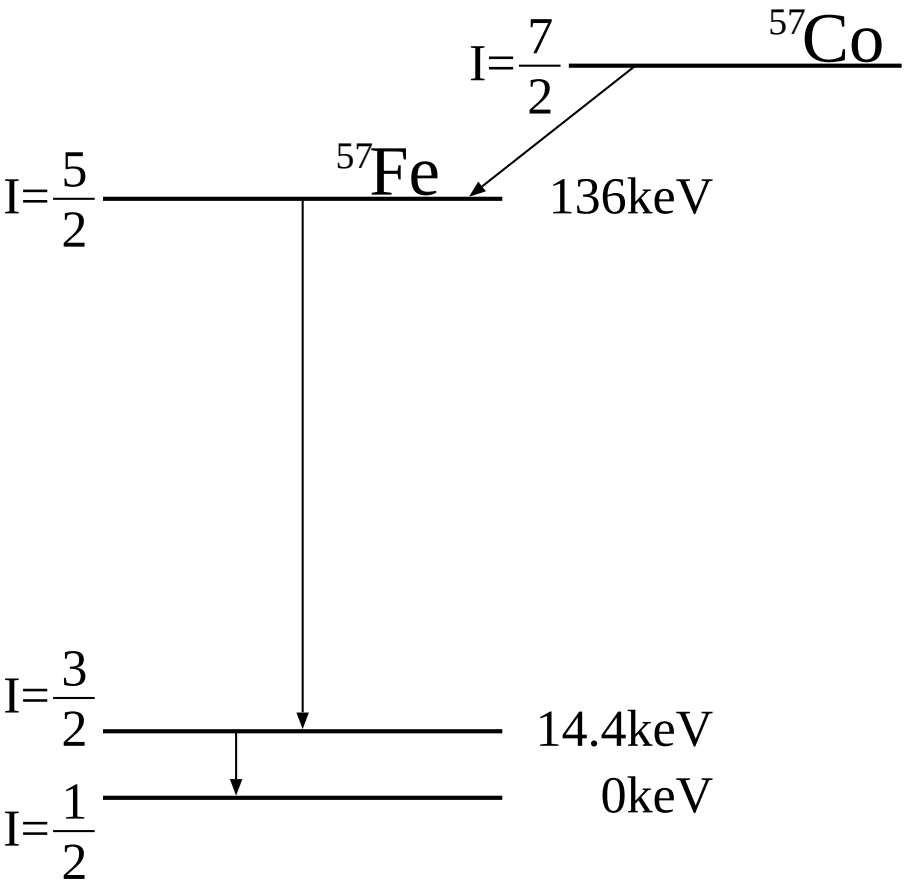

Figure B.2: Energy level scheme of ^{57}Fe

Bibliography

[1] M. Mekata, H. Yoshimura and H. Takaki, *J. Phys. Soc. Jpn.*, **33** (1972) 62.

[2] J. Häglung and G. Grimvall, *Phys. Rev.*, B **43** (1991) 14400.

[3] P. J. Dismukes, M. W. Yim and S. V. Ban, *J. Cryst. Growth*, **13/14** (1972) 365.

[4] H. F. George and H. K. John, *Phys. Rev.*, **93** (1954) 1004.

[5] L. M. Corliss, N. Elliott and J. M. Hastings, *Phys. Rev.*, **117** (1960) 929.

[6] A. Mavromaras, S. Matar, B. Siberchicot and G. Demazeau, *J. Magn. Magn. Mater.*, **134** (1994) 34.

[7] N. Heiman and N. S. Kazama, *J. Appl. Phys.*, **52** (1981) 3562.

[8] A. Oueldennaoua, E. Bauer-Grosse, M. Foos and C. Frantz, *Scr. Metall.*, **19** (1985) 1503.

[9] H. Nakagawa, S. Nasu, M. Takahashi and F. Kanamaru, *Hyperfine Int.*, **69** (1991) 455.

[10] K. Suzuki, H. Morita, T. Kaneko, H. Yoshida and H. Fujimori, *J. Alloys Comp.*, **201** (1993) 11.

[11] K. Suzuki, T. Kaneko, H. Yoshida, H. Morita and H. Fujimori, *J. Alloys Comp.*, **224** (1995) 232.

[12] T. L. Loucks, *Augmented Plane Wave Method*, (W. A. Benjamin, Inc., 1967).

[13] T. Takeda and J. Küblar, *J. Phys. F*: Metal Phys., **9** (1979) 661.

[14] M. Weinert, *J. Math. Phys.*, **22** (1981) 2433.

[15] O. Gunnarsson and B. I. Lundqvist, *Phys. Rev.*, B **13** (1976) 4274.

[16] F. D. Murnaghan, *Proc. Natl. Acad. Sci.*U.S.A., **30** (1944) 244.

[17] V. L. Moruzzi, J. F. Janak and A. R. Williams, *Calculated Electronic Properties of Metals*, (Pergamon Press Inc., New York, 1978).

[18] W. Lengauer, *J. Solid State Chem.*, **76** (1988) 412.

[19] A. N. Christiansen, *Acta. Chem. Scand.*, A **32** (1978) 87.

[20] B. R. Zhao, L. Chen and H. L. Luc, *Phys. Rev.*, B **29** (1984) 6198.

[21] V. P. Zhukov, V. A. Gubanov, O. Jepsen, N. E. Christensen, and O. K. Andersen : *J. Phys. Chem. Solids*, **49** (1988) 841.

[22] C. Amador, W. R. L. Lambrecht and B. Segall, *Phys. Rev.*, B **46** (1992) 1870.

[23] T. Asada, K. Terakura, *Phys. Rev.*, B **46** (1992) 13599.

[24] J. Kübler, *Phys. Lett.*, A **81** (1981) 81.